

Institute of Theoretical Physics
Faculty of Physics, Warsaw University

**Isolated Photon Production
in Deep Inelastic Compton Process
at HERA**

Andrzej Zembrzusi

*A Dissertation submitted
in partial fulfillment of the
requirements for the degree of
Doctor of Philosophy*

Supervisor: dr hab. Maria Krawczyk, prof. UW

August 2004

Acknowledgments

I would like to express my gratitude to my supervisor, Prof. Maria Krawczyk, for her support, many helpful discussions and the suggestion of the interesting topic. This dissertation could not have been accomplished without the guidance of Prof. Maria Krawczyk.

I am grateful to Prof. Peter Bussey and Dr. Sergei Chekanov from the ZEUS Collaboration, and Dr. Jörg Gayler and Dr. Rachid Lemrani from the H1 Collaboration for discussions and explanations concerning the experimental analyses.

I would like to thank Prof. Michel Fontannaz for providing me with the fortran subroutines computing the AFG and AFG02 parton densities in the photon and BFG fragmentation functions.

Many thanks to Dr. Paweł Jankowski for comments and discussions.

Finally, I am deeply grateful to my family, Zofia, Konrad and Marek Zembrzuski, and to Gosia Rytelewska for their support and help.

Contents

| | | |
|----------|---|-----------|
| 1 | Introduction | 1 |
| 2 | The Deep Inelastic Compton process in NLO QCD | 8 |
| 2.1 | Contributing processes | 8 |
| 2.1.1 | Born process and $\mathcal{O}(\alpha_S)$ corrections, resolved γ <u>or</u> fragmentation into γ | 8 |
| 2.1.2 | Counting of orders. Alternative set of diagrams | 12 |
| 2.1.3 | Full set of diagrams included in analysis. Resolved γ <u>and</u> fragmentation into γ , box diagram | 14 |
| 2.2 | Calculation details | 16 |
| 2.3 | Equivalent photon approximation | 18 |
| 3 | Inclusive photon production | 19 |
| 3.1 | Cross section formulae | 19 |
| 3.2 | Numerical results | 20 |
| 4 | Isolated photon production. Small cone approximation | 24 |
| 4.1 | Isolation restrictions | 24 |
| 4.2 | Small cone approximation | 25 |
| 4.3 | Analytical results | 25 |
| 4.4 | Numerical results and discussion | 28 |
| 4.4.1 | Effects of isolation | 28 |
| 4.4.2 | Effects of other cuts | 30 |
| 4.4.3 | Dependence on the choice of the renormalization scale | 32 |
| 4.4.4 | Comparison with the ZEUS data | 33 |
| 4.4.5 | Comparison with other QCD predictions (LG) | 38 |
| 5 | Isolated photon production. Exact implementation of isolation cuts | 41 |
| 5.1 | Cross section formulae | 42 |
| 5.2 | Division of phase space | 42 |
| 5.3 | Analytical results | 45 |
| 5.4 | Numerical results and discussion | 46 |
| 5.4.1 | Comparison between exact and approximated results | 47 |
| 5.4.2 | Comparison with the H1 data | 47 |

CONTENTS

| | | |
|----------|--|-----------|
| 5.4.3 | Comparison with other QCD predictions (FGH) | 50 |
| 6 | Isolated photon plus jet production | 51 |
| 6.1 | Jet algorithm | 51 |
| 6.2 | Numerical results and discussion | 52 |
| 6.2.1 | Asymmetric cuts | 52 |
| 6.2.2 | Theoretical uncertainties | 53 |
| 6.2.3 | Comparison with the H1 data | 60 |
| 6.2.4 | Comparison with other QCD predictions (FGH) | 62 |
| 7 | Probing the gluon content of the photon | 64 |
| 7.1 | Calculation of the cross section | 65 |
| 7.2 | Numerical results | 66 |
| 8 | Summary | 68 |
| | Tables | 70 |
| A | Kinematics and notation | 72 |
| A.1 | $2 \rightarrow 2$ processes | 72 |
| A.2 | $2 \rightarrow 3$ processes | 73 |
| B | Cross sections for $2 \rightarrow 2$ processes | 74 |
| C | Three-body phase space | 76 |
| D | Corrections of order $\mathcal{O}(\alpha_s)$ to the Born process | 79 |
| D.1 | General formulae for $2 \rightarrow 3$ processes | 79 |
| D.2 | Inclusive photon cross section | 81 |
| D.3 | Collinear configuration $(\vec{p}_1 \vec{p}_e$ or $\vec{p}_2 \vec{p}_e)$ | 81 |
| D.4 | Collinear configuration $(\vec{p}_1 \vec{p}_p$ or $\vec{p}_2 \vec{p}_p)$ | 83 |
| D.5 | Collinear configuration $(\vec{p}_1 \vec{p}_\gamma)$ | 86 |
| D.6 | Collinear configuration $(\vec{p}_2 \vec{p}_\gamma)$ | 88 |
| | Bibliography | 89 |

Chapter 1

Introduction

The Standard Model of particle physics is a successful theory describing the elementary particles and their interactions. It combines the $SU(2)_L \otimes U(1)_Y$ theory of electroweak interactions with the $SU(3)$ Quantum Chromodynamics (QCD) - the theory of strong interactions. The strong interacting particles, *hadrons* (e.g. protons), are build from more elementary point-like objects, *quarks* and *gluons*. The quarks are charged and they interact also electromagnetically with other charged particles, e.g. electrons, by exchange of the point-like *photons*. The electromagnetic interactions are described by the Quantum Electrodynamics (QED), being a part of the unified $SU(2)_L \otimes U(1)_Y$ theory.

This work is devoted to the theoretical study of the *photoproduction* of the photon with a large *transverse momentum*, called the Deep Inelastic Compton (DIC) process, in the electron-proton scatterings at the DESY HERA collider. We calculate the cross sections for this process with the beyond leading logarithmic accuracy within a framework of the *perturbative* QCD (see eg. [1]).

The *photoproduction* is a process in which a real or almost real photon collides with another particle producing some final state particles (for recent reviews see [2, 3, 4]). Currently, all high energy photon-proton collisions are realized in the electron-proton scatterings. They correspond predominantly to events with low virtuality of the exchanged photons, $Q^2 \approx 0$. These quasi-real photons colliding with the proton may lead for instance to a production of jets or particles with a large transverse momentum, p_T . If p_T is much larger than the QCD scale, $p_T \gg \Lambda_{QCD}$, then the perturbative QCD can be applied to describe such a process.

Processes in which the large transverse momentum of *jets*, *hadrons* or *photons* is observed in a final state in the e^+e^- , *hadron-hadron* and *electron-proton* colliders play an important role in testing QCD and in measuring the *parton densities* or the *parton fragmentation functions* as well as the *strong coupling constant* α_S . The process with the production of the photon is a special one, since the photon may couple directly to quarks involved in the *hard* QCD process, so it may provide a relatively clear information about the QCD dynamics. Such photons arising predominantly from the hard process are called *prompt* photons. Although the cross sections for the prompt photon production are smaller than for the production of jets, these processes are

considered as an important source of complementary informations.

The photoproduction of the prompt photon in the electron-proton scattering is shown in Fig. 1.1. In such a reaction an almost real photon emitted from the electron

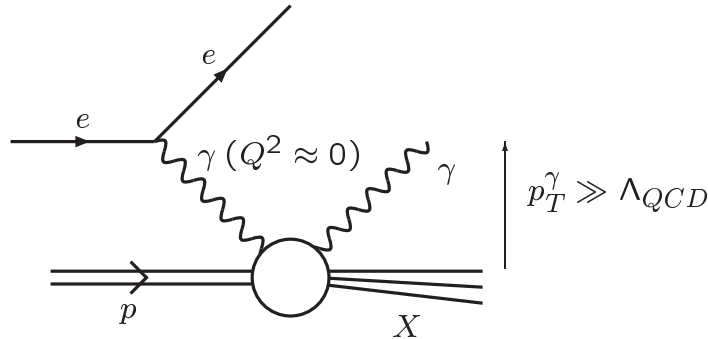


Figure 1.1: The $ep \rightarrow e\gamma X$ photoproduction.

interacts with the proton leading to the production of large- p_T photon and a hadronic system X : $ep \rightarrow e\gamma X$ ¹. Particles in the hadronic final state can form a jet or jets which balance the photon transverse momentum. If, beside the final photon, the jet is considered, we write: $ep \rightarrow e\gamma jet X$ (Fig. 1.2), where X stands for other hadronic final state. In the work we study both types of processes: $ep \rightarrow e\gamma X$ and $ep \rightarrow e\gamma jet X$.

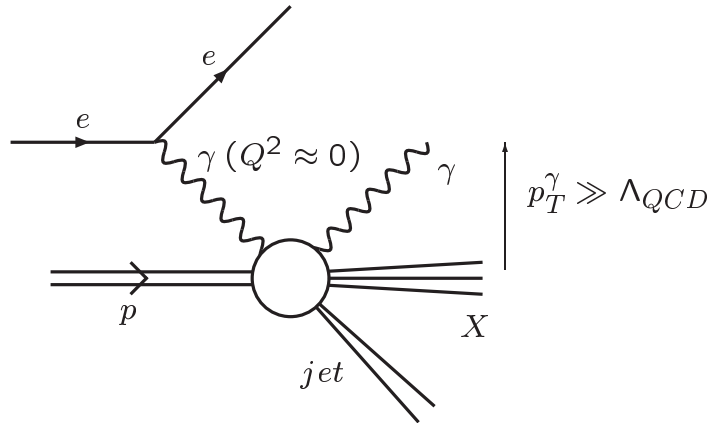


Figure 1.2: The $ep \rightarrow e\gamma jet X$ photoproduction.

In the lowest order of perturbative QCD the photon emitted by the electron is scattered from the quark being a component of the proton (the Born contribution), see Fig. 1.3. The final state of the hard interaction between the photon and the initial quark consists of the large- p_T photon and the quark from which the jet arises. In this lowest order process both the mediating and the final photon interact directly with the quark.

¹For a relatively small momentum transfer between the initial and the final electron, $Q^2 \approx 0$, the exchange of the photon dominates over the Z boson exchange and we do not include the Z boson in our analysis. We also neglect the emission of the final photon directly from the electron as it gives a very small contribution to the cross section for the photoproduction of large- p_T photons [5].

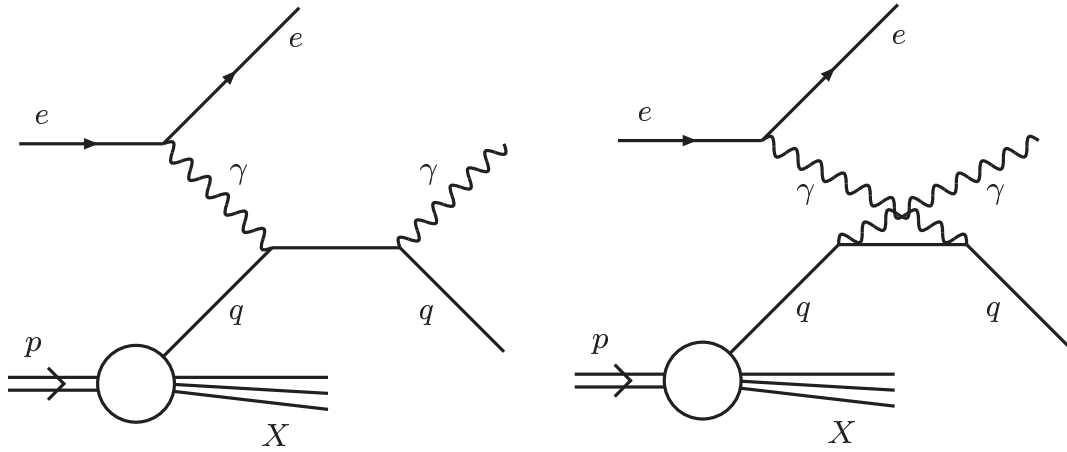


Figure 1.3: The Born contributions to the $ep \rightarrow e\gamma(\text{jet}) X$ photoproduction.

However, there are also processes of a quite different nature. At high energies the photon being a point-like *gauge boson*, may interact like a hadron. This hadron-like properties of the photon are due to fluctuations into a virtual pair quark-antiquark or into a vector meson, see Fig. 1.4. Due to these fluctuations the photon may

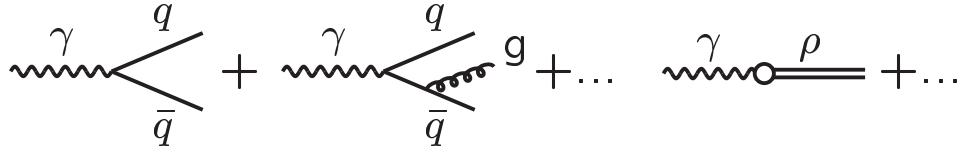


Figure 1.4: Various processes contributing to the hadron-like “structure of the photon”.

behave as an object consisting of quarks, antiquarks and gluons. The interactions in which such a photon, called the *resolved photon*, exhibits its complex hadronic-like “structure” are effectively described using the formalism of the *photon structure functions* [6, 7] in full analogy to the corresponding formalism for the proton [8, 9, 1]. The density of probability of “finding” the parton (quark or gluon) “inside” the photon is given in this formalism by the parton density/distribution in the photon, $f_{q(g)/\gamma}$. The process $\gamma \rightarrow q + \text{anything}$ described by the function $f_{q/\gamma}$ is illustrated in Fig. 1.5. The parton densities are related to the *structure functions*, as for the proton.



Figure 1.5: The resolved photon.

However, the photon structure functions, e.g. F_2^γ , in contrast to the corresponding proton structure functions, are calculable in the *Parton Model*, based on the $\gamma^*\gamma \rightarrow q\bar{q}$

process. The F_2^γ is proportional to the *electromagnetic coupling constant*, α , and it depends logarithmically on the energy scale of the process, μ , already in the *Parton Model*²:

$$F_2^\gamma \sim \alpha \ln \frac{\mu^2}{\Lambda_{QCD}^2} + \dots \quad (1.1)$$

We stress that this logarithmic scaling violation in F_2^γ in the Parton Model arises from the purely electromagnetic coupling $\gamma \rightarrow q\bar{q}$. For more detailed discussion on the concept of the “photon structure” see e.g. [3, 4, 10].

So, taking into account the hadronic structure of the photon, the photon mediating in the electron-proton scattering shown in Figs. 1.1 and 1.2 may interact with the constituents of the proton directly (as in Fig. 1.3) or indirectly as the resolved photon. Similarly, the final photon can be produced directly in the hard interaction with the quark (as in Fig. 1.3) or it may originate from *fragmentation processes*. The cross section of the latter processes involve relatively poorly known *parton-to-photon fragmentation functions* (see e.g. [11] and references therein) which describe the density of probability of the parton “decay” into the photon, see Fig. 1.6. Fortunately, one can

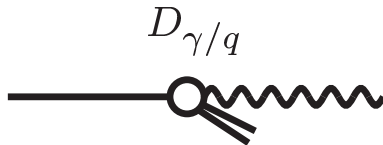


Figure 1.6: *The quark-to-photon fragmentation.*

suppress this contribution introducing the *isolation* of the final photon. The *isolation* constraints, which separate the photon from energetic hadrons, are introduced in both experimental and theoretical analyses. We follow this approach in this work.

The standard experiments to extract the parton densities in the proton or photon are the Deep Inelastic Scatterings in the ep or $e\gamma$ collisions, where the structure functions F_2^p and F_2^γ are measured. From these structure functions the corresponding parton densities can be derived. The photoproduction processes, as the prompt photon production considered herein, can provide an additional information about the parton densities in both the proton and the photon, see e.g. [2, 3].

The production of the photons with large transverse momenta in the γp scatterings, and its importance for probing the proton structure, was studied theoretically for the first time in 1969 [8]. The concept of the resolved photon was included in the analyses of this process ten years latter [12]. Then, a few groups of authors studied the inclusive (i.e. non-isolated) large- p_T photon production in the γp or ep scattering, and its importance for testing QCD and constraining the parton densities in both the proton and photon [13]-[26]. The next-to-leading order (NLO) QCD predictions for the photoproduction of isolated photons in the ep process at the HERA collider

²In the case of the $\gamma^*\gamma \rightarrow q\bar{q}$ process, the energy scale μ squared is equal to the virtuality, Q^2 , of the virtual photon (γ^*) which probes the structure of the real photon (γ).

have been presented in the papers [27, 28, 29, 30]. Finally, the photoproduction of the isolated photon and a jet at HERA has been calculated in NLO QCD in [31]-[36]. There is also a NLO calculation for the isolated photon and the isolated photon plus a jet production in the deep inelastic events ($Q^2 \gg 1 \text{ GeV}^2$) [37, 38, 11, 39], which is in many theoretical aspects close to the calculations for the corresponding photoproduction events.

The photoproduction of isolated photons without and with additional jets has been measured at the HERA collider by the ZEUS [40]-[45] and H1 [46]-[49] Collaborations. All the NLO QCD predictions as well as the Monte Carlo simulations for the isolated photon with no jet requirement tend to lie below the ZEUS data for the photon rapidities $\eta^\gamma < 0.1$ [41, 42, 43, 45], and below the final H1 data [49] in the whole range of the photon rapidities³. On the other hand the H1 data [49] for the isolated photon plus jet production are somewhat better described by the QCD predictions.

In the paper [44] the ZEUS Collaboration has implemented in Monte Carlo simulations for the prompt photon plus jet production the intrinsic transverse momentum of partons in the proton. From a fit to the data it was found that the effective intrinsic transverse momentum is very large with respect to the mass of the proton, namely $\langle k_T \rangle = 1.69 \pm 0.18_{-0.20}^{+0.18} \text{ GeV}$. In our work the intrinsic transverse momentum is not included, since one can argue that the measured $\langle k_T \rangle$ in the proton describes effectively higher order emissions or multiple interactions between particles involved in the process. Moreover, it was shown in [32] that the NLO QCD calculation is able to describe the ZEUS data [44] with no need for the intrinsic transverse momentum.

As it was mentioned above, there are some moderate discrepancies between the QCD predictions and the data for the photoproduction of the isolated photons in ep scattering, especially when no jet in the final state is considered. Note, that some differences between theory and data are also observed for other processes involving photons in the hadron-hadron, ep and e^+e^- collisions, see e.g. [50, 51, 52, 53]. It may indicate, that our understanding of such processes is not satisfactory yet, and further theoretical and experimental searches are needed. This is one of reasons for our study.

This thesis contains a detailed theoretical analysis of the cross section for the photoproduction of the prompt photon and the prompt photon plus a jet including effects due to the structure of the photon and the fragmentation into photon. In most of theoretical studies the parton densities in the photon, f_γ , and the parton-to-photon fragmentation functions, D_γ , are treated as quantities of order $\mathcal{O}(\alpha/\alpha_S)$. In our calculations they are considered as quantities of order $\mathcal{O}(\alpha)$. This leads to a different set of diagrams included in our calculation [28, 30, 33] and in calculations of other authors [27, 29, 31, 32, 34, 35, 36] for the photoproduction of the isolated photons at HERA.

We implement the isolation restrictions in the cross section using two methods. First, we use the *small cone approximation* method, in which the isolation is implemented in an approximated way. This method was previously used by other authors.

³The rapidity of e.g. the photon is defined as $\eta^\gamma \equiv -\ln \tan(\theta/2)$, where θ stands for the angle between the final photon momentum and the momentum of the initial proton. The positive rapidity is pointed in the proton direction.

However, not all expressions needed to calculate the higher order corrections in the small cone approximation exist in the literature, so we derive and present the missing formulae. Next, we use the method, in which the phase space of produced particles is divided into a few parts. This allows to implement the isolation, as well as other kinematic cuts, in an exact way. We perform a comparison between both methods and show that the small cone approximation is quite accurate and leads to reliable predictions for the prompt photon production at HERA.

The division (slicing) of the phase space is a standard approach to calculate various cross sections, e.g. cross sections for the isolated photon production. However, our method differs in details from methods applied in other calculations and allows to obtain relatively simple analytical formulae for the cross sections including higher order corrections.

The formulae for the higher order corrections are different in each part of the divided phase space. Our method of the division allows to apply in some parts of the phase space the known cross sections for the non-isolated photon production. In other parts of the phase space we derive all needed analytical expressions for the higher order corrections to the isolated photon production in the ep collision. Some obtained expressions are consistent with formulae presented previously by other authors (for processes other than this considered herein). We find it useful to present in this work in a compact analytical form all the expressions, which are necessary to obtain the cross section for the isolated photon production in the ep scattering including higher order corrections.

This thesis is based on the papers listed below and it contains in addition some new results never published before:

- M. Krawczyk and A. Zembrzuski, “Probing the structure of virtual photon in the deep inelastic Compton process at HERA,” *Phys. Rev. D* **57** (1998) 10 [arXiv:hep-ph/9708274],
- M. Krawczyk, A. Zembrzuski and M. Staszal, “Survey of recent data on photon structure functions and resolved photon processes,” DESY 98-013, arXiv:hep-ph/9806291,
- M. Krawczyk and A. Zembrzuski, in: A. Astbury, D. Axen, J. Robinson (Eds.), *Proceedings of the 29th Int. Conference on High Energy Physics, ICHEP’98, Vancouver, Canada, July 1998*, World Scientific, 1999, p.895, “NLO prediction for the photoproduction of the isolated photon at HERA,” arXiv:hep-ph/9810253,
- M. Krawczyk and A. Zembrzuski, “The forward photon production and the gluonic content of the real and virtual photon at the HERA collider,” *Nucl. Phys. Proc. Suppl.* **82** (2000) 167 [arXiv:hep-ph/9912368],
- M. Krawczyk, A. Zembrzuski and M. Staszal, “Survey of present data on photon structure functions and resolved photon processes,” *Phys. Rept.* **345** (2001) 265 [arXiv:hep-ph/0011083].

-
- M. Krawczyk and A. Zembrzusi, “Photoproduction of the isolated photon at DESY HERA in next-to-leading order QCD,” *Phys. Rev. D* **64** (2001) 114017 [arXiv:hep-ph/0105166],
 - A. Zembrzusi and M. Krawczyk, “Photoproduction of isolated photon and jet at the DESY HERA,” arXiv:hep-ph/0309308,

The paper is organized as follows. First, in Chapter 2 we discuss our choice of diagrams and present some calculation details. The formula for the cross section and our results for the inclusive (non-isolated) photon production are briefly discussed in Chapter 3. In Chapter 4 the isolation cuts are defined and the calculation for the isolated photon in the small cone approximation is presented; we study the influence of the isolation cut on the production rate of the photon and the role of other cuts applied in experiments. Then, in Chapter 5 the division (slicing) of the three body phase space is discussed and we present our analytical results. Here, the numerical predictions for the isolated photon production with the exact implementation of the isolation cuts are also presented and compared with the previous approximated ones. The results for the $ep \rightarrow e\gamma \text{ jet } X$ process are presented in Chapter 6. We discuss theoretical uncertainties and compare our predictions with predictions of other NLO QCD calculations, as well as with existing data for the photoproduction of the isolated photon or the isolated photon plus a jet at HERA (Chapters 4, 5, 6). In Chapter 7 we briefly discuss the sensitivity of the leading order (LO) cross section to the gluon distribution in the photon taking into account a non-zero virtuality of the exchanged photon, $Q^2 \neq 0$. The summary is given in Chapter 8. Finally, the Appendices contain the formulae for the cross sections for all the processes included in our analysis. Some of these formulae are taken from the literature and the other are briefly derived.

Chapter 2

The Deep Inelastic Compton process in NLO QCD

Our calculation bases on the standard leading twist perturbative QCD description of hard hadronic processes. This means that we consider such diagrams where one active parton from each initial particle is involved in the hard process. However, in some Monte Carlo simulations performed by experimental groups recently (2004) a large effect of multiple interactions was found for the prompt photon production at HERA. This effect is included in experimental analyses by introducing some models. We present predictions based on our calculations and “corrected” by an experimental group for the multiple interactions as well as hadronization processes in Chapters 5 and 6.

There are several calculations for the photoproduction of prompt (isolated) photons at the HERA collider, namely: the calculation of Gordon and Vogelsang (GV) [27], Gordon (LG) [31], Krawczyk and Zembruski (K&Z) [28, 30, 33] and Fontannaz, Guillet and Heinrich (FGH) [29, 32]. All these calculations differ from one another by set of diagrams included in next-to-leading order (NLO). Below we discuss our choice of diagrams (Sec. 2.1), as well as some calculation details (Secs. 2.2, 2.3).

2.1 Contributing processes

2.1.1 Born process and $\mathcal{O}(\alpha_S)$ corrections, resolved γ or fragmentation into γ

We wish to study the hard electron-proton scattering leading to a production of a photon or a photon plus a jet and anything else, $ep \rightarrow e\gamma (jet) X$ (Figs. 1.1-1.3). In this reaction the mediating photon arising from the electron interacts with a partonic constituent (quark or gluon) inside the proton [8]. In the lowest order (Born) process, $\gamma q \rightarrow \gamma q$, the photon is scattered from a quark yielding the final photon and the quark, see Fig. 2.1. This subprocess is of order $\mathcal{O}(\alpha^2)$ and has a pure electromagnetic nature. To obtain the NLO QCD predictions, the corrections of order $\mathcal{O}(\alpha_S)$ to the Born

process have to be taken into account. These corrections lead to partonic processes of order $\mathcal{O}(\alpha^2\alpha_S)$. They include the virtual gluon exchange (Fig. 2.2), the real gluon emission (Fig. 2.3) and the process $\gamma g \rightarrow \gamma q\bar{q}$ (Fig. 2.4) [15, 17, 18, 25].

The corrections due to the virtual gluon exchange and the real gluon emission contain *infrared* singularities which cancel when both contributions are added up properly

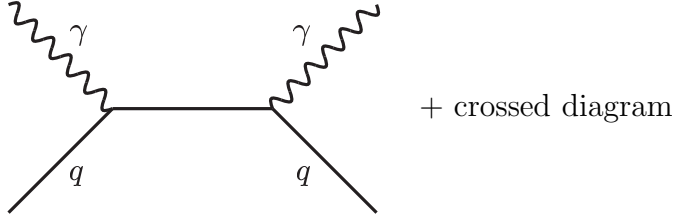


Figure 2.1: The Born process (the Compton scattering on the quark).

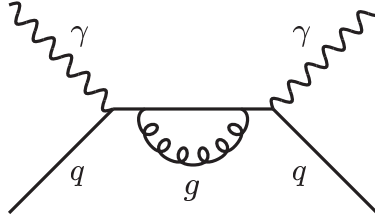


Figure 2.2: An example of the virtual gluon corrections to the Born process.

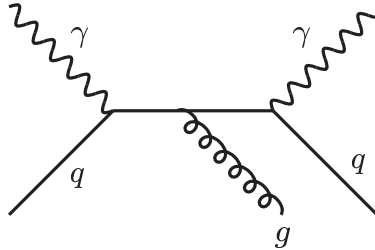


Figure 2.3: An example of the real gluon corrections to the Born process, $\gamma q \rightarrow \gamma qg$.

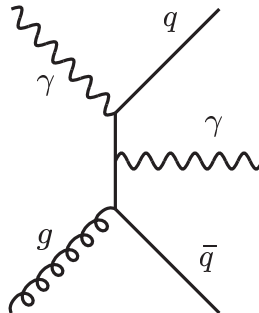


Figure 2.4: An example diagram for the process $\gamma g \rightarrow \gamma q\bar{q}$.

in the scattering amplitude squared (see Secs. 3.1, 4.2, 5.2). The contribution due to the processes $\gamma q \rightarrow \gamma qg$ and $\gamma g \rightarrow \gamma q\bar{q}$ contains another type of singularities, so called *mass* or *collinear* singularities, which do not cancel. In order to remove them from the cross section the *factorization* procedure is applied: the singularities are subtracted and shifted into corresponding parton densities in the proton or photon or into parton-to-photon fragmentation functions [18, 25]. At this stage the *factorization* scale appears. The *bare* (scale invariant) parton densities in the proton are replaced by renormalized *scale dependent* densities. Moreover, the *scale dependent* parton densities in the photon and the *scale dependent* fragmentation functions appear in the calculation. They are necessary ingredients in the NLO calculation to absorb the mass singularities.

The factorization procedure is illustrated in Figs. 2.5 and 2.6: the singularities due to the collinear configurations in the vertexes $\gamma \rightarrow q\bar{q}$ and $q \rightarrow \gamma q$ are shifted and

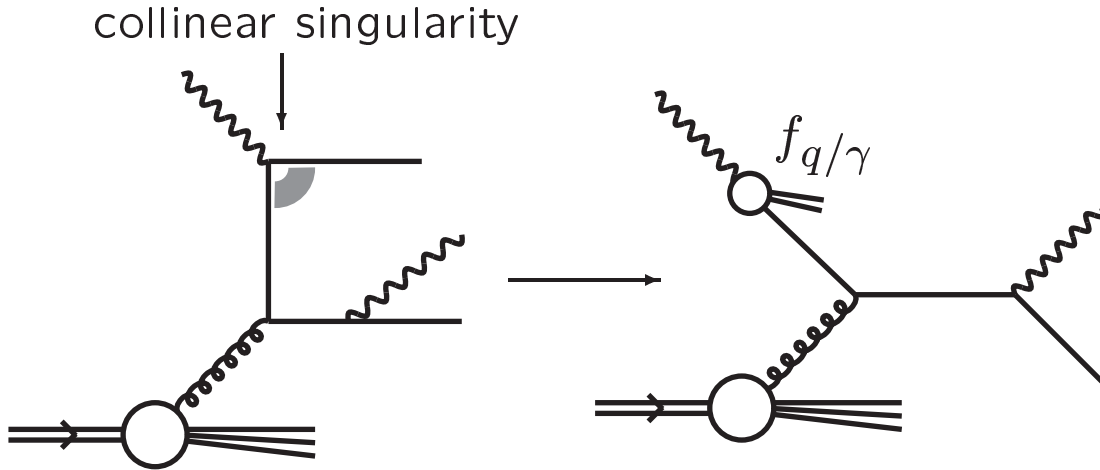


Figure 2.5: A sample of diagrams illustrating the factorization of the collinear singularities from the process $\gamma g \rightarrow \gamma q\bar{q}$ into the parton density in the photon, $f_{q/\gamma}$.

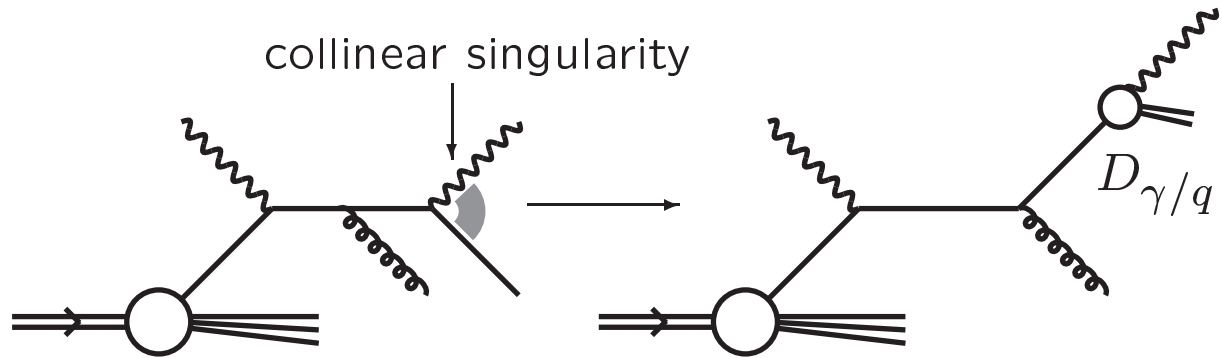


Figure 2.6: A sample of diagrams illustrating the factorization of the collinear singularities from the process $\gamma q \rightarrow \gamma qg$ into the fragmentation function, $D_{\gamma/q}$.

absorbed by the corresponding quark density in the photon ($f_{q/\gamma}$) or by the quark-to-photon fragmentation function ($D_{\gamma/q}$), respectively (for precise definitions and details see [18, 25]).

It is worth mentioning that there was a discussion whether for the photoproduction of isolated photons in e^+e^- collisions the conventional factorization breaks down, and whether the cross section is an infrared safe quantity [54, 55, 56]. In principle these questions could as well occur for the photoproduction of isolated photons in ep collisions. However we do not deal with this problem because it arises from $2 \rightarrow 3$ processes involving the parton-to-photon fragmentation, which are absent in our calculation. We checked this explicitly and found that all the singularities in our calculations for the isolated photon production are canceled or factorized, as in the case of non-isolated photon production, and the cross sections are well defined [28, 30, 33] (see also [27, 29, 31, 32], [34]-[39]).

The processes involving the parton densities in the *resolved* initial photon are shown in Fig. 2.7. In these processes a parton (quark or gluon) from the photon interacts with a parton arising from the proton yielding the *direct* final photon and a parton. Fig. 2.8 shows the processes with the fragmentation of a parton into the final photon. Here the *direct* initial photon interacts with a parton from the proton leading to a production of two partons; one of these partons produces the final photon in the *fragmentation* process. The name *direct* photons stand for the photons participating directly in the hard partonic process.

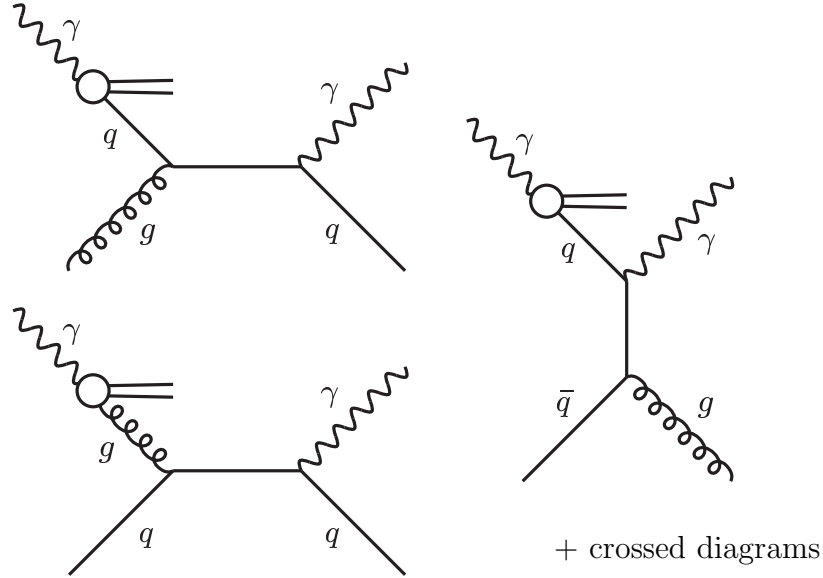


Figure 2.7: The processes with the resolved initial photon.

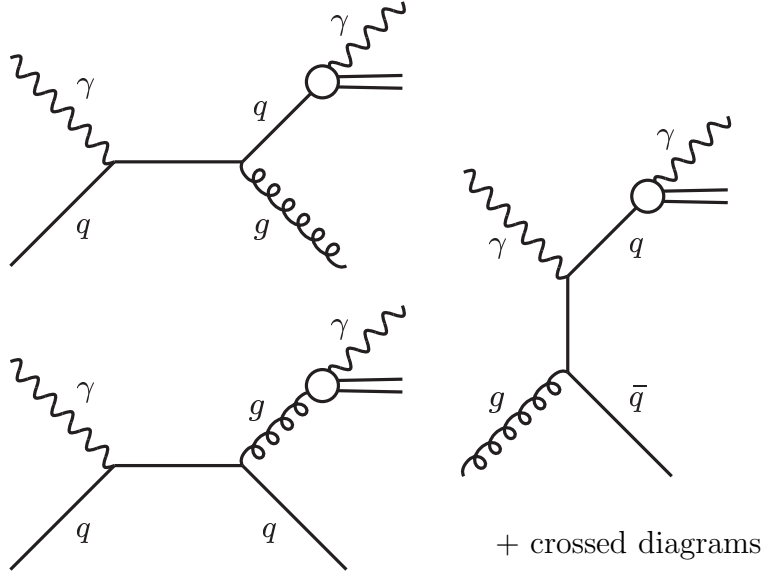


Figure 2.8: The processes with the parton-to-photon fragmentation.

2.1.2 Counting of orders. Alternative set of diagrams

The hard partonic processes in Figs. 2.7 and 2.8 are of order $\mathcal{O}(\alpha\alpha_S)$. They are convoluted with the corresponding parton densities or fragmentation functions which are proportional to the electromagnetic coupling constant α . These distributions contain the logarithmic dependence on the factorization/renormalization scale μ : $f_\gamma \sim \alpha \ln \mu^2/\Lambda_{QCD}^2$ and $D_\gamma \sim \alpha \ln \mu^2/\Lambda_{QCD}^2$. The logarithm behaves like the inverse of the strong coupling, $\ln \mu^2/\Lambda_{QCD}^2 \sim 1/\alpha_S$ and many authors (e.g. [27, 29, 31, 32, 34, 35, 36]) treat f_γ and D_γ as being of order $\mathcal{O}(\alpha/\alpha_S)$. This conclusion arises from the *evolution equation* and the *renormalization group equation*, as it shown in [57]. If so, then the processes shown in Figs. 2.7, 2.8 are of order $\mathcal{O}(\alpha\alpha_S \cdot \alpha/\alpha_S) = \mathcal{O}(\alpha^2)$, i.e. identical with the order of the Born process (Fig. 2.1). Note however, that the logarithmic behavior of the parton densities in the photon or the parton-to-photon fragmentation functions arises from the pure electromagnetic coupling $\gamma \rightarrow q\bar{q}$ and $q \rightarrow \gamma q$, respectively [6], as already discussed in Introduction. From this point of view the considered distributions should be rather treated as the quantities of order $\mathcal{O}(\alpha)$ since the logarithm $\ln \mu^2/\Lambda_{QCD}^2$ coming from the electromagnetic interaction is not related to the strong coupling constant, see also [20, 28, 30] and for more detailed discussion in [58]. Such a counting, f_γ and $D_\gamma \sim \mathcal{O}(\alpha)$, leads to an assignment of the $\mathcal{O}(\alpha^2\alpha_S)$ order to the processes shown in Figs. 2.7, 2.8.

The different counting of orders in the strong coupling leads to the different sets of processes included in our NLO calculation for the prompt photon production at HERA [28, 30, 33] in comparison with other NLO calculations. They include in addition (beside the $\mathcal{O}(\alpha_S)$ corrections to the Born cross section) the $\mathcal{O}(\alpha_S)$ corrections to the processes with the resolved initial photon or parton-to-photon fragmentation [27,

29, 31, 32], and the $\mathcal{O}(\alpha_S)$ corrections to the processes with both the resolved initial photon and parton-to-photon fragmentation [27, 29, 32]¹. These corrections are not included in our NLO calculation since in our approach they should be taken into account together with the next-to-next-to-leading (NNLO) order corrections to the Born process.

It should be emphasized that the $\mathcal{O}(\alpha_S)$ corrections to the Born process contain (after the factorization procedure) an explicit logarithmic dependence on the scale μ , $\ln s/\mu^2$. This dependence is compensated by $\ln \mu^2/\Lambda_{QCD}^2$ from f_γ and D_γ if the $\mathcal{O}(\alpha_S)$ corrections to the Born process are included in the cross section consistently with the corresponding contributions involving parton densities in the photon or parton-to-photon fragmentation functions. Similarly, the $\mathcal{O}(\alpha_S)$ corrections to the processes with the resolved initial photon or the fragmentation into the final photon should be, from our point of view, taken into account together with the $\mathcal{O}(\alpha_S^2)$ corrections to the Born process in order to compensate the dependence on the μ^2 in the hadronic cross section.

One can argue that, since the other authors [27, 29, 31, 32] include more diagrams, their calculation is more accurate. It is true that including more diagrams usually improves the quality of QCD predictions but it is not obvious that it is always the case (see also the discussion in Secs. 4.4.3 and 4.4.5).

It is worth mentioning that there are also other authors who treat the processes involving photons in a similar way as we do. The authors of [64] (see also [65, 66]) present the NLO calculation for the prompt photon production in the e^+e^- collision with the quark-to-photon fragmentation. They include the fragmentation function at the same order as the $\mathcal{O}(\alpha_S)$ corrections, since the fragmentation is in a close relation with the corresponding collinear configuration in $\mathcal{O}(\alpha_S)$ corrections (compare Fig. 2.6). It allows to cancel an explicit dependence on the scale μ^2 . A similar NLO calculation for the prompt photon production in the deep inelastic ep events (with $Q^2 > 10 \text{ GeV}^2$) at the HERA collider is presented in [39, 38, 11]. In this calculation the diagrams shown in Figs. 2.1-2.4 and 2.8 are included without the $\mathcal{O}(\alpha_S)$ corrections to the processes involving the fragmentation (the contributions due to the resolved initial photon are negligible for large Q^2). The cancellation (to a large extent) of the μ^2 dependence is therein also stressed.

Another kind of arguments is presented in [67], where the NLO calculation for the prompt photon production in the e^+e^- collision is investigated. The authors of [67] claim that the parton-to-photon fragmentation, despite being of order $\mathcal{O}(\alpha/\alpha_S)$ for the non-isolated photon production, should be counted as the quantity of order $\mathcal{O}(\alpha)$ for the isolated final photon, since the isolation itself is a correction of order $\mathcal{O}(\alpha_S)$.

Counting f_γ and D_γ as being of order $\mathcal{O}(\alpha/\alpha_S)$ allows for a self-consistent expansion of physical quantities (structure functions, cross sections) in powers of $1/\ln \mu^2/\Lambda_{QCD}^2$ (with $\alpha_S \sim 1/\ln \mu^2/\Lambda_{QCD}^2 + \dots$) [57]. On the other hand, our approach, where $f_\gamma, D_\gamma \sim \mathcal{O}(\alpha)$, allows for a consistent counting of powers of α_S (since the logarithm $\ln \mu^2/\Lambda_{QCD}^2$ in f_γ and D_γ it is not $1/\alpha_S$, see also [20, 58]).

¹All these QCD corrections have been calculated (most of them twice) in [59]-[63]

The photon is a very special particle: being the point-like object it sometimes exhibits hadronic-like “structure”. This double nature of the photon leads to more complicated description within the QCD than for purely hadronic processes, and further study is needed to clarify what is the proper organization of the QCD perturbative series for processes involving photons. This should include among others also the calculation of the $\mathcal{O}(\alpha_s^2)$ corrections to the Born process.

2.1.3 Full set of diagrams included in analysis. Resolved γ and fragmentation into γ , box diagram

Besides the diagrams discussed in Sec. 2.1.1, we include in our numerical analysis also other diagrams, namely the diagrams with the resolved γ and the fragmentation into γ and the box diagram. In Figs. 2.9, 2.10 the processes with the resolved initial photon and the fragmentation into the final photon are shown. If we take $f_\gamma, D_\gamma \sim \mathcal{O}(\alpha)$, all these processes are of order $\mathcal{O}(\alpha^2\alpha_s^2)$ and strictly speaking go beyond the NLO accuracy of our calculations. Nevertheless we include them, since they were taken into account in most of existing NLO calculations for the (non-isolated or isolated) prompt photon production at HERA and are found to be important [15, 18], [20]-[24], [26]-[34].

Finally, we take into account the photon-by-gluon scattering, so called box process, $\gamma g \rightarrow \gamma g$, shown in Fig. 2.11 [68]. The box process is also of order $\mathcal{O}(\alpha^2\alpha_s^2)$, i.e. beyond the accuracy of our calculation. However it is a very special process as it is the lowest order contribution to the photon-by-gluon scattering, it contains no singularities, and no parton densities in the photon or fragmentation functions are involved. We think that including the box process does not introduce any additional ambiguities in the summation of partonic cross sections. The box contribution to the reaction $ep \rightarrow e\gamma X$ or $\gamma p \rightarrow \gamma X$ was considered in previous calculations and it is known to be large [14, 18], [19]-[24], [26]. It is included in the calculations for the isolated photon production at HERA by authors K&Z [28, 30, 33] and FGH [29, 32] but it is omitted by GV [27] and LG [31].

To summarize, in our NLO calculation we take into account the following contributions:

- the Born contribution (Fig. 2.1),
- the $\mathcal{O}(\alpha_s)$ corrections to the Born diagram, including the $\gamma g \rightarrow \gamma q\bar{q}$ process (Figs. 2.2-2.4),
- the processes with the resolved initial photon (Fig. 2.7) or with the fragmentation into the final photon (Fig. 2.8),
- the processes with the resolved initial photon and the fragmentation into the final photon (Figs. 2.9, 2.10),
- the box process (Fig. 2.11).

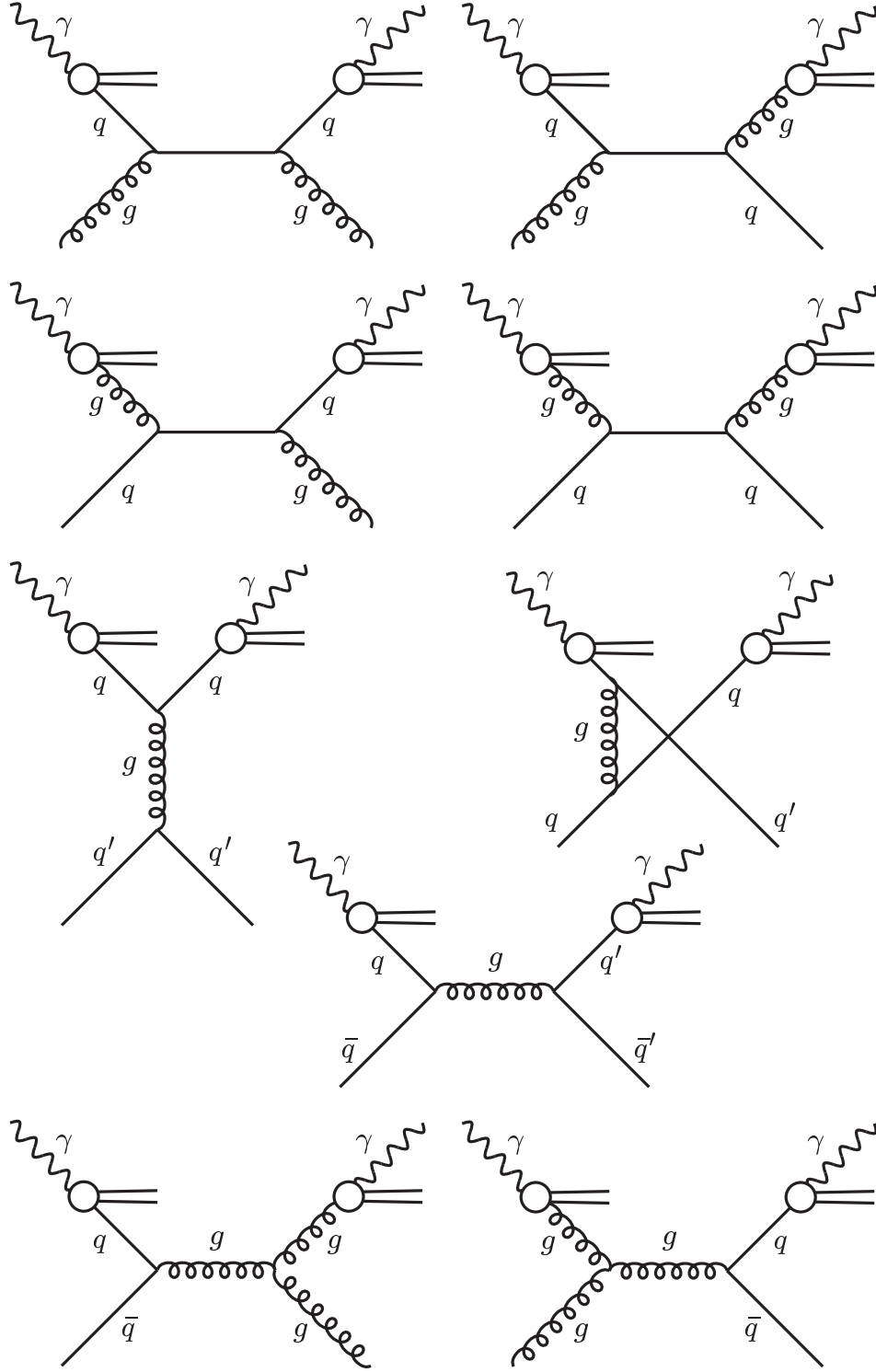


Figure 2.9: The processes involving the resolved initial photon and the parton-to-photon fragmentation.

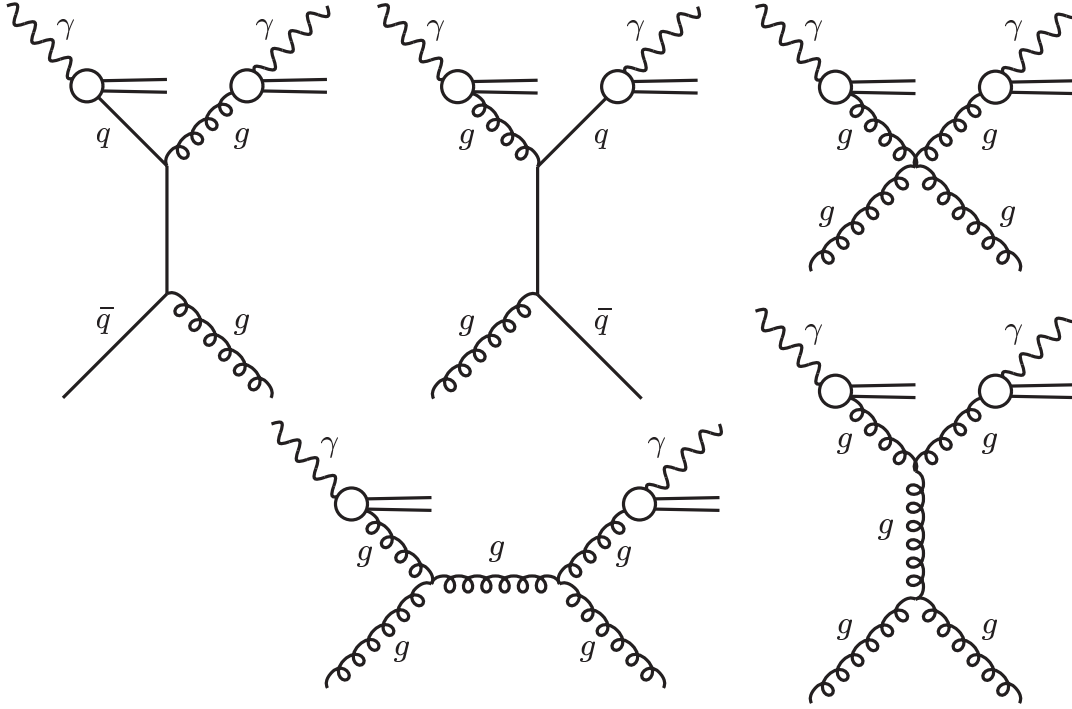


Figure 2.10: Continuation of Fig. 2.9.

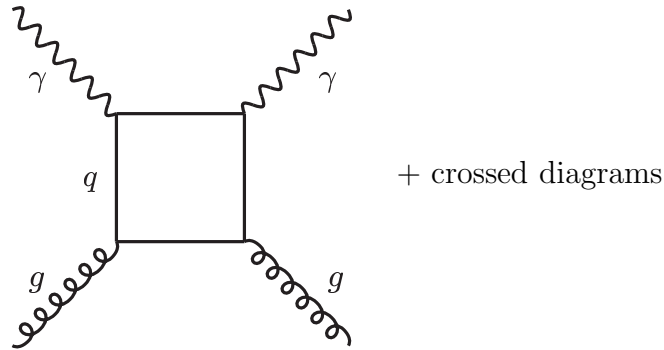


Figure 2.11: The box diagram.

2.2 Calculation details

We perform NLO QCD calculations in the modified Minimal Subtraction ($\overline{\text{MS}}$) renormalization scheme [69]. The factorization/renormalization scales in parton densities and fragmentation functions are assumed being equal to the renormalization scale in the strong coupling constant and are denoted as μ . As a reference we take μ equal to the transverse momentum² (transverse energy) of the final photon, $\mu = p_T^\gamma = E_T^\gamma$.

²By the transverse momentum, p_T , we mean the component of the momentum perpendicular to momenta of the initial particles.

For a comparison $\mu = E_T^\gamma/2$ and $\mu = 2E_T^\gamma$ will be also considered.

The quark masses are neglected in the calculation and the number of active flavors is assumed to be $N_f=4$ or, for a comparison, $N_f=3$ or 5. The cross section is proportional to the electric charge of the quark in the fourth power, so the contribution of the bottom quark ($e_b=-1/3$) is expected to be much smaller than the contributions of the up and charm quarks ($e_u=e_c=2/3$), and the predictions for $N_f=4$ and 5 should not differ considerably. On the other hand, the differences between the results obtained using $N_f=4$ and 3 can be large.

The two-loop coupling constant α_s is applied in the form

$$\alpha_s(\mu^2) = \frac{12\pi}{(33 - 2N_f) \ln(\mu^2/\Lambda_{QCD}^2)} \left[1 - \frac{6(153 - 19N_f)}{(33 - 2N_f)^2} \frac{\ln[\ln(\mu^2/\Lambda_{QCD}^2)]}{\ln(\mu^2/\Lambda_{QCD}^2)} \right]. \quad (2.1)$$

To obtain the QCD parameter Λ_{QCD} appearing in the strong coupling constant (2.1), we use the world average of α_s at the scale M_Z (the mass of the Z^0 gauge boson) [70]:

$$\overline{\alpha_s}(M_Z^2) = 0.1183 \pm 0.0027. \quad (2.2)$$

In order to minimize theoretical and experimental uncertainties the above $\overline{\alpha_s}(M_Z^2)$ value was determined in [70] from precise data based on NNLO analyses only; the data given at scales different than M_Z were extrapolated to the M_Z scale using the four-loop coupling. Although we use the two-loop expression (2.1), we apply (2.2) as the best estimation of the true value of $\alpha_s(M_Z)$. We take the number of active flavours $N_f=3, 4$ or 5 at scales $\mu < m_c$, $m_c < \mu < m_b$ and $\mu < m_b$, respectively, with the following charm, bottom and Z masses: $m_c = 1.5$ GeV, $m_b = 4.7$ GeV, $M_Z = 91.2$ GeV [70]. Assuming that $\alpha_s(\mu^2)$ is a continuous function at $\mu = m_c$ and $\mu = m_b$ the obtained Λ_{QCD} parameters are: $\Lambda_{QCD}=0.386, 0.332$ and 0.230 GeV for $N_f=3, 4$ and 5, respectively. The above Λ_{QCD} values are used in numerical calculations discussed in the next chapters (Chapters 3, 5, 6) ³.

In the calculations we apply the Glück-Reya-Vogt (GRV) parton densities in the proton [71] and photon [72], and the GRV fragmentation functions [73]. For a comparison we also use other parametrizations, namely Martin-Roberts-Stirling-Thorne (MRST98) [74], (MRST99) [75], (MRST2002) [76], CTEQ4M [77], CTEQ6M [78], Aurenche-Chiappetta-Fontannaz-Guillet-Pilon (ACFGP) [24], Aurenche-Guillet-Fontannaz (AFG) [79] and (AFG02) [80], Gordon-Storow (GS) [81], Cornet-Jankowski-Krawczyk-Lorca (CJLK) [82], Duke-Owens (DO) [15], Bourhis-Fontannaz-Guillet (BFG) [83] and Glück-Reya-Stratmann (GRS) [84].

Following experimental analysis [40]-[49], we consider the photoproduction of the photon at HERA with transverse momentum (transverse energy) higher than 5 GeV. In such processes the emission of the final large- p_T photon directly from the electron (Bethe-Heitler process) is negligible [5] and we omit it ⁴ (this process is neglected in all

³Note that in Chapters 4 and 7 different numbers are used for consistency with the published results.

⁴For transverse energy higher than 5 GeV the momentum transfer, $-t$ (see Eq. (A.6)), is higher than 25 GeV². Note that for $Q_{max}^2 = 1$ GeV² and lower values of the momentum transfer, $4 \leq -t \leq 10$ GeV², the contribution of the Bethe-Heitler process may be no-negligible in some kinematic regions, see Fig. 6 in Ref. [85].

existing calculations for the photoproduction of isolated photons at HERA [27]-[34]).

The results presented in next sections are obtained in NLO QCD with use of the GRV set of parametrizations with $\mu = E_T^\gamma$, $N_f = 4$ and $\Lambda_{QCD}=0.332$ GeV unless stated otherwise.

2.3 Equivalent photon approximation

Our aim is to consider the production of photons with large transverse momentum in the electron-proton scattering in processes in which the electron is scattered at a small angle. In such events the mediating photon is almost on-shell, $Q^2 \approx 0$ (photoproduction events), and the cross section can be calculated using the equivalent photon (Weizsäcker-Williams) approximation [86, 87] (see also e.g. [88, 89, 4]). In this approximation the differential cross section for the ep collision is related to the corresponding differential cross section for the γp collision; in case of the considered herein reaction, $ep \rightarrow e\gamma X$ (or $ep \rightarrow e\gamma \text{ jet } X$), we get (see Fig. 2.12):

$$d\sigma^{ep \rightarrow e\gamma(jet)X} = \int G_{\gamma/e}(y) d\sigma^{\gamma p \rightarrow \gamma(jet)X} dy, \quad (2.3)$$

where y is the fraction of the initial electron momentum carried by the exchanged photon, and $G_{\gamma/e}$ stands for the flux of the real photons emitted from the electron. We use the photon spectrum in the form [89]:

$$G_{\gamma/e}(y) = \frac{\alpha}{2\pi} \left\{ \frac{1 + (1-y)^2}{y} \ln \left[\frac{Q_{max}^2(1-y)}{m_e^2 y^2} \right] - \frac{2}{y} \left(1 - y - \frac{m_e^2 y^2}{Q_{max}^2} \right) \right\}, \quad (2.4)$$

with m_e being the electron mass. In the numerical calculations the maximal photon virtuality $Q_{max}^2 = 1 \text{ GeV}^2$ is assumed, what is a typical value for the recent photoproduction measurements at the HERA collider [40]-[49]. The above formula describes the spectrum of equivalent real (transversally polarized) photons. We do not take into account longitudinally polarized photons and the interference between longitudinally and transversally polarized photons, since they give a very small contribution in the kinematic regions which we study [5, 90].

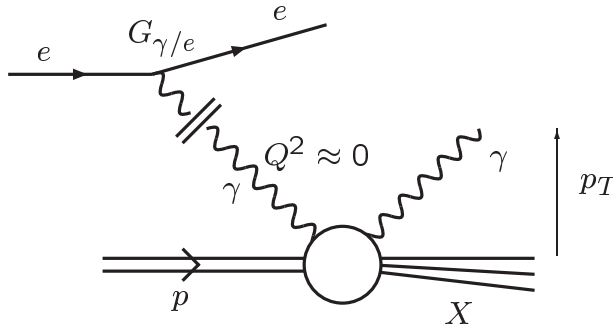


Figure 2.12: The factorization of the $ep \rightarrow e\gamma X$ reaction.

Chapter 3

Inclusive photon production

The inclusive production of the photon with a large transverse momentum in the γp or ep collision at HERA and other colliders was the subject of detailed studies in the literature [8], [12]-[26], and herein only the main aspects of the calculation of the cross section including NLO QCD corrections are briefly discussed. The main cross section formula and explicit expressions for various contributions are given in Sec. 3.1 and in the Appendices.

3.1 Cross section formulae

The differential cross section for the $\gamma p \rightarrow \gamma X$ (or $\gamma p \rightarrow \gamma \text{ jet } X$) process has the following form:

$$d\sigma^{\gamma p \rightarrow \gamma(jet)X} = \sum_{q,\bar{q}} \int dx f_{q/p}(x, \mu^2) d\sigma^{\gamma q \rightarrow \gamma q} + \int dx f_{g/p}(x, \mu^2) d\sigma^{\gamma g \rightarrow \gamma g} \quad (3.1)$$

$$+ \sum_{a=q,\bar{q},g} \int dx_\gamma \sum_{b=q,\bar{q},g} \int dx f_{a/\gamma}(x_\gamma, \mu^2) f_{b/p}(x, \mu^2) d\sigma^{ab \rightarrow \gamma d} \quad (3.2)$$

$$+ \sum_{b=q,\bar{q},g} \int dx \sum_{c=q,\bar{q},g} \int \frac{dz}{z^2} f_{b/p}(x, \mu^2) D_{\gamma/c}(z, \mu^2) d\sigma^{\gamma b \rightarrow cd} \quad (3.3)$$

$$+ \sum_{a=q,\bar{q},g} \int dx_\gamma \sum_{b=q,\bar{q},g} \int dx \sum_{c=q,\bar{q},g} \int \frac{dz}{z^2} f_{a/\gamma}(x_\gamma, \mu^2) f_{b/p}(x, \mu^2) \cdot D_{\gamma/c}(z, \mu^2) d\sigma^{ab \rightarrow cd} \quad (3.4)$$

$$+ \sum_{q,\bar{q}} \int dx \left\{ f_{q/p}(x, \mu^2) \left[d\sigma_{\alpha_S}^{\gamma q \rightarrow \gamma q} + d\sigma_{\alpha_S}^{\gamma q \rightarrow \gamma qg} \right] + f_{g/p}(x, \mu^2) d\sigma_{\alpha_S}^{\gamma g \rightarrow \gamma q\bar{q}} \right\}, \quad (3.5)$$

where $\gamma q \rightarrow \gamma q$, $\gamma g \rightarrow \gamma g$ etc. are various partonic processes described in the previous chapter. The functions $f_{a/\gamma}$, $f_{b/p}$, and $D_{\gamma/c}$ stand for the parton distributions in the photon and proton, and the parton-to-photon fragmentation function, respectively. The corresponding longitudinal-momentum fractions carried by partons in the proton and photon are denoted as x and x_γ . Similarly, for the parton-to-photon fragmentation

the variable z is introduced. The μ scale is the factorization/renormalization scale related to the physical hard scale of the considered process.

The contribution of processes with the direct both initial and final photon are given on the right-hand side in (3.1) (see Figs. 2.1, 2.11). The expressions (3.2-3.4) stand for contributions of processes with the resolved photons or/and the fragmentation into the photon (Figs. 2.7-2.10). The formulae for the partonic cross sections, $d\sigma^{\gamma q \rightarrow \gamma q}$ etc., appearing in (3.1-3.4) are listed in Appendix B. The $\mathcal{O}(\alpha_S)$ corrections to the Born process are included in (3.5), where $d\sigma_{\alpha_S}^{\gamma q \rightarrow \gamma q}$, $d\sigma_{\alpha_S}^{\gamma q \rightarrow \gamma qg}$ and $d\sigma_{\alpha_S}^{\gamma g \rightarrow \gamma q\bar{q}}$ are the partonic cross sections for the processes shown in Figs. 2.2-2.4.

The $\mathcal{O}(\alpha_S)$ corrections to the Born process were first numerically calculated for the inclusive photon production in [15], and the compact analytical formulae can be found in [18, 25]. These corrections contain the infrared and/or collinear singularities. The collinear singularities are present in the squared amplitudes of the $2 \rightarrow 3$ processes (Figs. 2.3, 2.4), and are factored out and absorbed by the corresponding parton densities in the proton or photon (Fig. 2.5), and by the parton-to-photon fragmentation functions (Fig. 2.6). The infrared singularities are due to the soft gluon emission or the soft gluon exchange and cancel when the real gluon corrections (Fig. 2.3) are added to the virtual gluon corrections (Fig. 2.2) in agreement with the Bloch-Nordsieck theorem [91] (see [18, 25] for the calculation details). The corresponding singular-free partonic cross sections $d\sigma_{\alpha_S}^{\gamma q \rightarrow \gamma q} + d\sigma_{\alpha_S}^{\gamma q \rightarrow \gamma qg}$ and $d\sigma_{\alpha_S}^{\gamma g \rightarrow \gamma q\bar{q}}$ for the inclusive photon production are given in Eqs. (D.21) and (D.22) in Appendix D.2.

To obtain the predictions for the inclusive photon production one needs to perform the integrations of the cross section (3.1-3.5) within the whole range of the fractional momenta: $0 < x < 1$, $0 < x_\gamma < 1$, $0 < z < 1$. The Θ -functions in (D.21) and (D.22), and the δ -function in (B.1) ensure that in fact the x , x_γ and z close to zero do not contribute to the cross section.

3.2 Numerical results

The results for the inclusive (non-isolated) photon production at the HERA collider are obtained with the parameters and parton distributions given in Sec. 2.2. The initial electron and proton energies corresponding to energies at HERA are taken $E_e = 27.6$ GeV and $E_p = 920$ GeV, respectively [49].

In Fig. 3.1 the NLO cross section $d\sigma/dE_T^\gamma$ for the inclusive photon production in the ep scattering is presented (dashed line). The contribution of the processes with the resolved initial photon or/and the parton-to-photon fragmentation (solid line) and the contribution of the processes with the direct both photons (dotted line) are shown as well. The cross section decreases by three orders of magnitude when E_T^γ increases from 4 GeV to 20 GeV, and obviously the most important contribution to the total cross section is coming from the lowest E_T^γ region. The processes with the direct initial and final photons, i.e. Born plus $\mathcal{O}(\alpha_S)$ corrections and the box contribution (Figs. 2.1-2.4, 2.11), dominate in the cross section for large $E_T^\gamma \geq 9$ GeV. For lower E_T^γ the processes with the resolved initial photon or/and the fragmentation into final photon

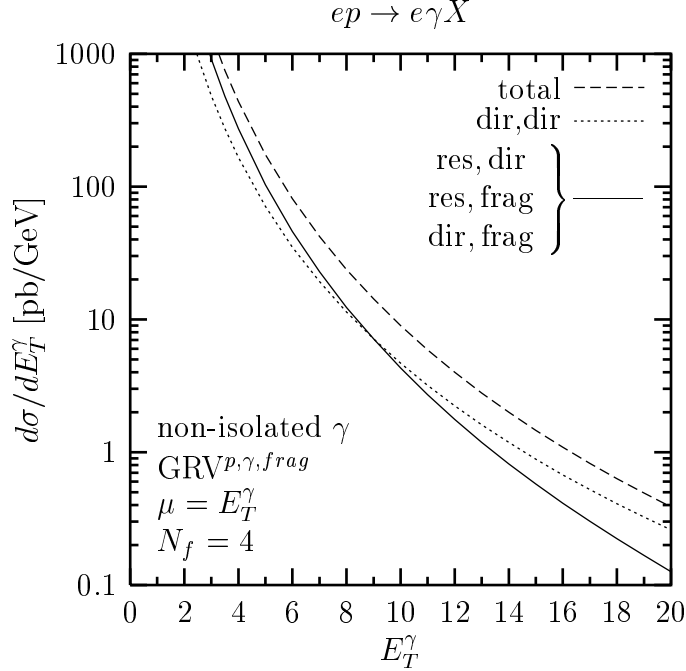


Figure 3.1: The cross section $d\sigma/dE_T^\gamma$ for the inclusive γ production at the HERA collider (dashed line). The contributions of processes with the direct initial and final γ (dotted line) and processes with the resolved initial γ or/and the fragmentation into final γ (solid line) are shown separately.

(Figs. 2.7-2.10) constitute more than a half of the cross section.

The importance of individual contributions to the inclusive photon cross section, integrated over $5 \text{ GeV} < E_T^\gamma < 10 \text{ GeV}$, is illustrated in Tab. 1 (the first row) and in Figs. 3.2 and 3.3, where the distributions of the final photon rapidity, η^γ , are shown. In this E_T^γ range the integrated (“total”) NLO cross section is equal to 241 pb. Processes other than the lowest order (Born) one give all together the contribution almost two times larger than the cross section for the Born process alone. The $\mathcal{O}(\alpha_s)$ corrections to the Born process are relatively small, negative at $\eta_\gamma < 0$ and positive at $\eta_\gamma > 0$ (Fig. 3.2), and constitute only 2% of the total cross section (Tab. 1). The box contribution constitutes 6% of the cross section integrated over all η_γ (Tab. 1) and it is even larger, 7-12%, for the differential cross section in the range $-1 < \eta_\gamma < 1$ (Fig. 3.2), where the data [42, 49] exists (see Chapters 4, 5, 6). Although the box diagram, $\gamma g \rightarrow \gamma g$, is of order $\mathcal{O}(\alpha^2\alpha_s^2)$, it gives relatively large contribution mainly due to a large gluonic content of the proton at small x .

The contribution of processes of order $\mathcal{O}(\alpha^2\alpha_s^2)$ with the resolved initial photon and the quark-to-photon fragmentation is large, being of order 20% (Tab. 1). It is worth noticing that this contribution is build from many, relatively small, individual terms (Figs. 2.9, 2.10). The parton-to-photon fragmentation with the direct or resolved initial photon (Figs. 2.7-2.10) gives in sum a contribution of 31% (Tab. 1) or 32-39% for the central rapidity range $-1 < \eta_\gamma < 1$ (Fig. 3.3), and this contribution is similar to the Born one (36%). Note that this part of the cross section involving

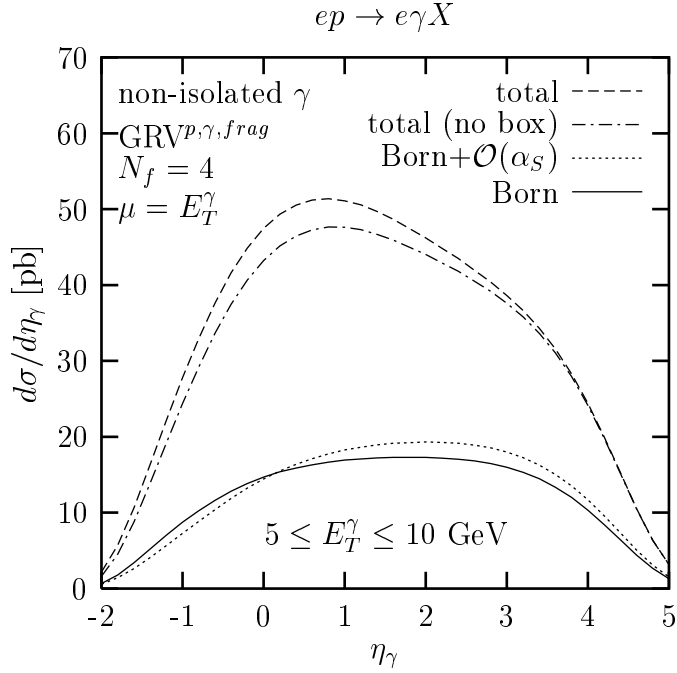


Figure 3.2: The cross section $d\sigma/d\eta_\gamma$ for the inclusive γ production at the HERA collider with (dashed line) and without (dashed-dotted line) the box contribution. The contributions of the Born process (solid line) and the Born process with the $\mathcal{O}(\alpha_S)$ corrections (dotted line) are shown.

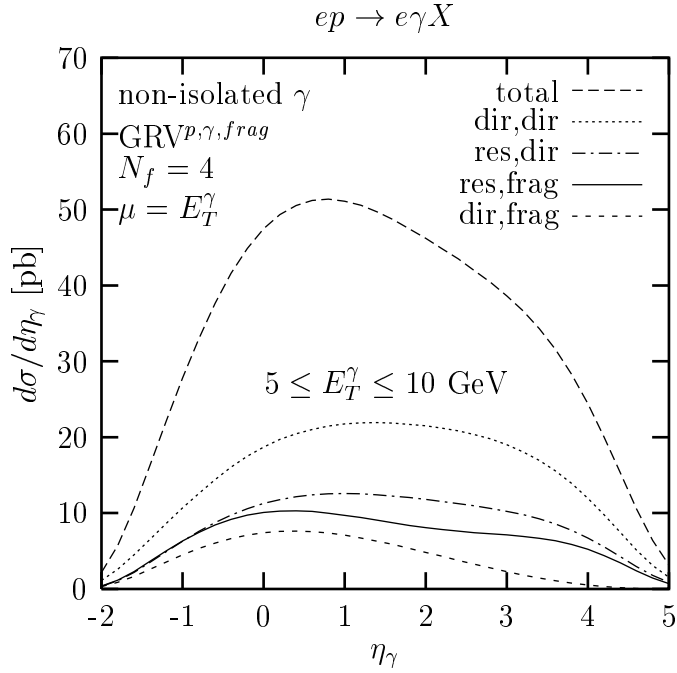


Figure 3.3: The cross section $d\sigma/d\eta_\gamma$ for the inclusive γ production at the HERA collider (dashed line) and the contributions of various types of processes with: the direct initial γ and the fragmentation into the final γ (short-dashed line), the resolved initial γ and the fragmentation into the final γ (solid line), the resolved initial and the direct final γ (dashed-dotted line), and direct both γ 's (dotted line).

poorly known fragmentation functions, D_γ , is much suppressed by implementing of experimental cuts, see Chapter 4.

In the whole range of η_γ the processes with the resolved initial and direct final photons constitute about 25% of the cross section ¹ (Tab. 1, Fig. 3.3). It makes the cross section sensitive to the photon structure function [15], [18]-[24], [26]-[36], [92, 93] and in particular to the gluonic content of the photon, what will be shortly discussed in Chapter 7.

¹This contribution is even enhanced if experimental constrains are taken into account (Chapter 4).

Chapter 4

Isolated photon production. Small cone approximation

In order to compare QCD predictions with data, one should consider such physical quantities, which are actually measured or are as close to the measured ones as possible. Since in experimental analyses in order to reduce backgrounds the observed photon is often required to be *isolated* from hadrons [40]-[49], similar isolation of the photon produced in the ep scattering was included in the QCD calculations. It was done for the first time by Gordon and Vogelsang [27, 31] and Gordon [31]. The second independent calculation was performed by Krawczyk and Zembrzuski [28, 30]. Then the calculation of Fontannaz, Guillet, Heinrich, [29, 32] and a new analysis of Zembrzuski and Krawczyk [33] were presented. In this chapter we discuss the QCD predictions for the isolated photon production presented in the paper of Krawczyk and Zembrzuski [30] ¹.

4.1 Isolation restrictions

The final photon is “isolated” if the sum of hadronic transverse energy within a cone of radius R around the photon is smaller than the photon transverse energy multiplied by a small parameter ϵ [40]-[49]:

$$\sum_{hadrons} E_T^{hadron} < \epsilon E_T^\gamma. \quad (4.1)$$

The cone is defined in the rapidity and azimuthal angle phase space, namely

$$\sqrt{(\eta^{hadron} - \eta^\gamma)^2 + (\phi^{hadron} - \phi^\gamma)^2} < R. \quad (4.2)$$

The isolation constraint allows to reduce the background from neutral mesons (π^0 , η), which decay into two photons and from photons radiated by final state hadrons. It suppresses considerably the contribution of processes involving the parton fragmentation into the photon. For comparison with data the same isolation restriction (4.1) is taken into account in theoretical calculations [27]-[36].

¹This is an extended and updated version of [28].

Note, that a different type of isolation which removes from the cross section the whole fragmentation component is advocated by Frixione [94]. We do not apply this type of isolation, since so far it is not applied in experimental analyses of the prompt photon production at the HERA collider.

4.2 Small cone approximation

The simplest way to calculate the differential cross section for an isolated photon production, $d\sigma_{isol}$, is to calculate the difference of the differential cross section for a non-isolated (inclusive) photon production, $d\sigma_{non-isol}$, and a subtraction term, $d\sigma_{sub}$ [95, 96, 97, 27]:

$$d\sigma_{isol} = d\sigma_{non-isol} - d\sigma_{sub}. \quad (4.3)$$

The calculation of $d\sigma_{non-isol}$ was discussed in the previous chapter. The subtraction term corresponds to the cuts which are opposite to the isolation cuts, i.e. within a cone of radius R around the final photon the total transverse energy of hadrons should be higher than the photon transverse energy multiplied by ϵ ,

$$\sum_{hadrons} E_T^{hadron} > \epsilon E_T^\gamma. \quad (4.4)$$

In this chapter we apply the subtraction term $d\sigma_{sub}$ calculated in an approximate way. This approximation bases on the assumption that an angle δ between the final photon and a parton inside the cone of radius R is small [96, 27]. It allows to simplify the calculations considerably and leads to the compact analytical expressions for all relevant matrix elements involved in $d\sigma_{sub}$. Note that in this approximation the maximal value of the angle δ is proportional to the radius R :

$$\delta \leq R/\cosh(\eta^\gamma) = RE_T^\gamma/E^\gamma, \quad (4.5)$$

where η^γ , E^γ and E_T^γ stand for the photon rapidity, energy and transverse energy, respectively. We stress that the above small angle (cone) approximation is used only in calculation of the $\mathcal{O}(\alpha_S)$ corrections in the subtraction cross section $d\sigma_{sub}$, while other contributions to $d\sigma_{sub}$ as well as $d\sigma_{non-isol}$ are obtained in an exact way.

4.3 Analytical results

The calculations include partonic processes with two ($2 \rightarrow 2$) or three ($2 \rightarrow 3$) particles in the final state:

$$ab \rightarrow cd \quad (4.6)$$

or

$$ab \rightarrow \gamma d_1 d_2, \quad (4.7)$$

CHAPTER 4. ISOLATED PHOTON PRODUCTION. SMALL CONE APPROXIMATION

where a is the photon or a parton originating from the photon, b is a parton from the proton, c stand for the final photon or a parton which decays into the photon in the fragmentation process, and $d_{(i)}$ denotes quarks and/or gluons. For the isolated final photon the summation in Eqs. (4.1, 4.4) runs over the c -parton remnant and over the d_i -partons, if they are inside the cone (4.2).

In the partonic $2 \rightarrow 2$ processes with a direct final photon ($c = \gamma$),

$$ab \rightarrow \gamma d, \quad (4.8)$$

the photon is isolated by definition, so they give no contribution to the subtraction term. If the final photon comes from the fragmentation process ($c \neq \gamma$),

$$ab \rightarrow cd, \quad (4.9)$$

it takes the z -fraction of the c -parton transverse energy, $E_T^\gamma = zE_T^c$. The hadronic remnant of the c -parton takes the fraction of transverse energy equal to $(1 - z)E_T^c$, and the photon is isolated if

$$E_T^\gamma = zE_T^c > \epsilon(1 - z)E_T^c \quad (4.10)$$

or

$$z > 1/(1 + \epsilon). \quad (4.11)$$

The subtraction term for $2 \rightarrow 2$ processes can be obtained from cross sections (3.3, 3.4) involving fragmentation functions integrated over z , with z -values fulfilling inequality opposite to (4.11), i.e. $z < 1/(1 + \epsilon)$. So we have

$$\begin{aligned} d\sigma_{frag,sub}^{\gamma p \rightarrow \gamma X} = & \sum_{b=q,\bar{q},g} \int_0^1 dx \sum_{c=q,\bar{q},g} \int_0^{1/(1+\epsilon)} \frac{dz}{z^2} f_{b/p}(x, \mu^2) D_{\gamma/c}(z, \mu^2) d\sigma^{\gamma b \rightarrow cd} \\ & + \sum_{a=q,\bar{q},g} \int_0^1 dx_\gamma \sum_{b=q,\bar{q},g} \int_0^1 dx \sum_{c=q,\bar{q},g} \int_0^{1/(1+\epsilon)} \frac{dz}{z^2} f_{a/\gamma}(x_\gamma, \mu^2) f_{b/p}(x, \mu^2) \\ & \cdot D_{\gamma/c}(z, \mu^2) d\sigma^{ab \rightarrow cd}. \end{aligned} \quad (4.12)$$

The total subtraction cross section consists of $d\sigma_{frag,sub}^{\gamma p \rightarrow \gamma X}$ and $\mathcal{O}(\alpha_S)$ corrections:

$$d\sigma_{sub}^{\gamma p \rightarrow \gamma X} = d\sigma_{frag,sub}^{\gamma p \rightarrow \gamma X} + d\sigma_{\alpha_S,sub}^{\gamma p \rightarrow \gamma X}. \quad (4.13)$$

The virtual gluon corrections do not contribute to the subtraction, since they come from $2 \rightarrow 2$ processes (Fig. 2.2), where the direct final photon is isolated by definition. The cross section $d\sigma_{\alpha_S,sub}^{\gamma p \rightarrow \gamma X}$ includes only contributions of $2 \rightarrow 3$ processes (4.7). In these processes the photon and two partons are produced. One parton, say d_1 , enters the cone of radius R around the photon (4.2), and its transverse energy should be higher than the photon's transverse energy multiplied by ϵ (4.4). There are three types of such processes, namely:

$$\bullet \gamma q \rightarrow \gamma q + g \text{ (with a quark inside the cone),} \quad (4.14)$$

$$\bullet \gamma q \rightarrow \gamma g + q \text{ (with a gluon inside the cone),} \quad (4.15)$$

$$\bullet \gamma g \rightarrow \gamma q + \bar{q} \text{ (with a quark or antiquark inside the cone).} \quad (4.16)$$

The subtraction cross section for $\mathcal{O}(\alpha_S)$ corrections has a general form:

$$d\sigma_{\alpha_S, sub}^{\gamma p \rightarrow \gamma X} = \sum_{i=1}^{2N_f} \int_0^1 \Theta \left(\frac{v(1-w)}{1-v+vw} - \epsilon \right) \left[f_{q_i/p}(x, \mu^2) d\sigma_{sub}^{\gamma q_i \rightarrow \gamma q_i + g} + \right. \\ \left. f_{q_i/p}(x, \mu^2) d\sigma_{sub}^{\gamma q_i \rightarrow \gamma g + q_i} + f_{g/p}(x, \mu^2) d\sigma_{sub}^{\gamma g \rightarrow \gamma q_i + \bar{q}_i} \right] dx, \quad (4.17)$$

where the variables v and w are defined in Appendix A.2. These variables are related to the final photon momentum and to the initial momenta, and depend on the fractional momenta y and x . To fulfill the condition (4.4) the integration is performed over x according to Θ function with

$$v(1-w)/(1-v+vw) > \epsilon, \quad (4.18)$$

since in the small cone approximation the transverse energy of the parton d_1 is related to the photon transverse energy in the following way:

$$E_T^{d_1} = E_T^\gamma v(1-w)/(1-v+vw). \quad (4.19)$$

The analytical results for the $\mathcal{O}(\alpha_S)$ corrections contributing to the subtraction term (4.17) are presented below. All collinear singularities are shifted into the fragmentation functions $D_{\gamma/c}$ (Fig. 2.6) according to the standard factorization procedure, as discussed in Introduction (for details for the non-isolated photon production see also [18, 25]). The infrared singularities do not appear in this calculations. This is due to the fact that there are no virtual gluon corrections, the gluons emitted inside the cone can not be too soft being constrained by Eqs. (4.18, 4.19), while the gluon emitted outside the isolation cone can not be soft, because its transverse momentum has to balance transverse momenta of the photon and the parton moving parallel to the photon. The cross sections for partonic processes (4.14-4.16), denoted in (4.17) by $d\sigma_{sub}^{\gamma b \rightarrow \gamma d_1 + d_2}$, are given by following expressions:

$$E^\gamma \frac{d\sigma_{sub}^{\gamma q_i \rightarrow \gamma q_i + g}}{d^3 p^\gamma} = \Theta(1-w) \frac{\alpha_{em}^2 \alpha_s e_{q_i}^4}{\pi \hat{s}^2} C_F \frac{(1-v+vw)^2 + (1-v)^2}{(1-v+vw)^2(1-v)} \cdot P, \quad (4.20)$$

$$E^\gamma \frac{d\sigma_{sub}^{\gamma q_i \rightarrow \gamma g + q_i}}{d^3 p^\gamma} = \Theta(1-w) \frac{\alpha_{em}^2 \alpha_s e_{q_i}^4}{\pi \hat{s}^2} C_F \frac{(R \cdot E_T^\gamma)^2}{\hat{s}} \cdot \frac{(1-v)[(1-v+vw)^2 + (vw)^2]}{(1-v+vw)^5 v(1-w)(vw)^2} [1 + (1-v+vw)^4 + v^4(1-w)^4], \quad (4.21)$$

$$E^\gamma \frac{d\sigma_{sub}^{\gamma g \rightarrow \gamma q_i + \bar{q}_i}}{d^3 p^\gamma} = \Theta(1-w) \frac{\alpha_{em}^2 \alpha_s e_{q_i}^4}{\pi \hat{s}^2} \frac{1}{2} \frac{(vw)^2 + (1-v)^2}{(1-v+vw)vw(1-v)} \cdot P, \quad (4.22)$$

where $C_F = 4/3$ and

$$P = \frac{1 + v^2(1 - w)^2}{1 - v + vw} \ln \left(\frac{(R^2 \cdot E_T^\gamma)^2 v^2 (1 - w)^2}{\mu^2} \right) + 1. \quad (4.23)$$

The function P (4.23) which appears in Eqs. (4.20) and (4.22) was previously presented e.g. in [96], where it was used in calculations for the prompt photon production in the hadron-hadron collisions. Other terms on the right-hand side in Eqs. (4.20) and (4.22) correspond to the partonic cross sections for the $2 \rightarrow 2$ processes, $\gamma q \rightarrow qg$ or $\gamma g \rightarrow q\bar{q}$, respectively. The expression (4.21) has been derived by us and presented for the first time in the paper of Krawczyk and Zembrzusi [30]. The derivation of formulae (4.20-4.22) is briefly discussed in Appendices D.5 and D.6.

These results are obtained with the assumption that the angle between the photon and the parton inside the cone is small and only the leading terms are kept. In $d^3\sigma_{sub}^{\gamma q_i \rightarrow \gamma q_i + g}$ (4.20) and $d^3\sigma_{sub}^{\gamma g \rightarrow \gamma q_i + \bar{q}_i}$ (4.22) the leading contribution is $\mathcal{O}(\ln R) + const$ and all terms of order $\mathcal{O}(R^2)$ or higher are neglected (terms of order $\mathcal{O}(R)$ do not appear). In $d^3\sigma_{sub}^{\gamma q_i \rightarrow \gamma g + q_i}$ (4.21) there are no logarithmic $\mathcal{O}(\ln R)$ or constant terms. For small ϵ , a soft gluon can be emitted into the isolation cone in the process $\gamma q_i \rightarrow \gamma g + q_i$, leading to a large $\mathcal{O}(R^2)$ term in (4.21), and therefore this contribution can not be neglected.

The small cone approximation was previously used to obtain the predictions for the prompt photon production at the hadron-hadron [96] as well as at the electron-proton [27] reactions. Then the exact (i.e. without the assumption that the cone is small) calculations were performed for both the hadron-hadron [98] and the electron-proton [31] collisions. The author of [98] compared the approximated and exact results and concluded that the applied approximation was reliable for the hadronic processes. Moreover, he mentioned in [31] that it is also an accurate technique for including isolation effects in the cross section for the prompt photon production in the electron-proton scattering. We have performed a detailed comparison between the predictions obtained for this process with the approximated and with the exact implementation of the isolation restrictions, see Sec. 5.4.1.

4.4 Numerical results and discussion

We perform the numerical calculations for the isolated photon production at the ep scattering using the HERA collider energies: $E_e=27.5$ GeV and $E_p=820$ GeV [42], and applying the parton densities specified in Sec. 2.2. In this section we use the parameter $\Lambda_{QCD}=0.365, 0.320$ and 0.220 GeV, fitted by us to the experimental value of $\alpha_s(M_Z) = 0.1177$ [99], for $N_f=3, 4$ and 5 , respectively.

4.4.1 Effects of isolation

The results for the isolated photon production are presented in Figs. 4.1 and 4.2 in comparison with the results for the non-isolated photon production in the ep collision.

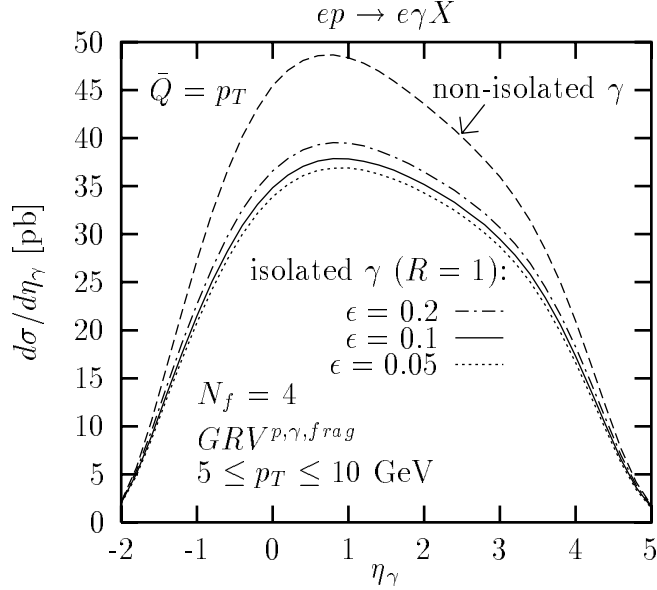


Figure 4.1: The differential cross section $d\sigma/d\eta_\gamma$ for the prompt γ photoproduction at HERA as a function of the photon rapidity η_γ for non-isolated photon (dashed line) and isolated photon with $R = 1$ and $\epsilon = 0.05$ (dotted line), 0.1 (solid line) and 0.2 (dashed-dotted line). The photon transverse energy, $E_T^\gamma \equiv p_T$, is taken in the range $5 \leq E_T^\gamma \leq 10$ GeV. The factorization/renormalization scale $\mu \equiv \bar{Q} = E_T^\gamma$ is used.

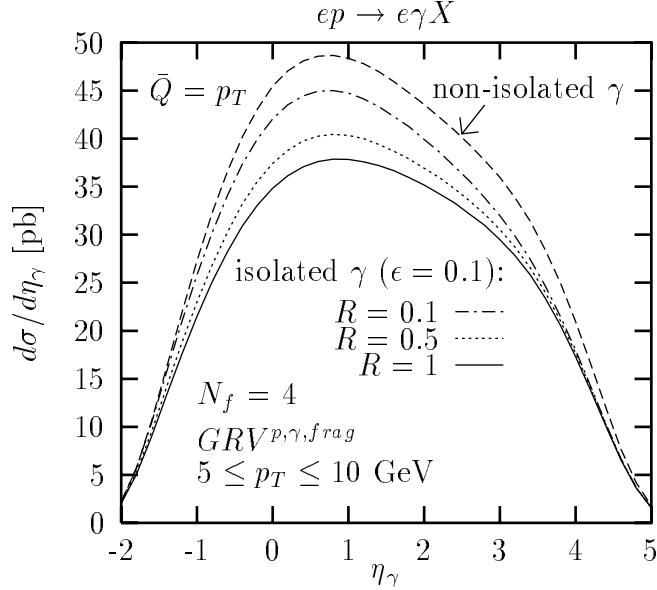


Figure 4.2: As in Fig. 4.1 for non-isolated photon (dashed line) and isolated photon with $\epsilon = 0.1$ and $R = 0.1$ (dashed-dotted line), 0.5 (dotted line) and 1 (solid line).

The presented differential cross sections $d\sigma/d\eta_\gamma$ are obtained for $5 \leq E_T^\gamma \leq 10$ GeV using various isolation cone parameters, ϵ and R . The isolation cut suppresses the cross section by above 10% in the whole range of the photon rapidities shown in Figs. 4.1, 4.2. For $\epsilon=0.1$ and $R = 1$ the suppression is 17-23% at rapidities $-1.5 < \eta_\gamma \leq 4$. This

large effect is not very sensitive to the value of ϵ : changing the value by a factor of 2 from $\epsilon = 0.1$ to $\epsilon = 0.2$ or to $\epsilon = 0.05$ varies the results for isolated photon by about 4% (Fig. 4.1). The dependence on R is stronger but also not very large: when the R value is changed by a factor of 2 (from 1 to 0.5) the results increase by about 7% (Fig. 4.2).

The suppression due to the isolation imposed on the photon is seen in Tab. 2, for the individual contributions and for the sum of all contribution. The results for both the non-isolated and isolated photons are shown in the first and the second row, respectively. As expected, the cross section for processes with fragmentation into final photon is strongly suppressed: due to the isolation it is lowered by a factor of 5. At the same time the $\mathcal{O}(\alpha_S)$ corrections to the Born diagram increase from 4.8 pb for the non-isolated γ to 13.1pb for the isolated γ , i.e. the contribution of this corrections to the subtraction cross section, $d\sigma_{sub}$, is negative. The requirement of isolation does not modify contributions of other processes since they are of $2 \rightarrow 2$ type and involve only the direct final photons. The subtraction cross section, being a sum of negative $\mathcal{O}(\alpha_S)$ corrections and fragmentation contributions, is of course positive. Finally, the total cross section for isolated final photon is lower, by 20%, than for the non-isolated one.

In further calculations discussed in this work the values $R = 1$ and $\epsilon = 0.1$ are assumed, as in analyses of the H1 and ZEUS Collaborations [40]-[49].

4.4.2 Effects of other cuts

In order to compare the results obtained by us with the data we take into account the isolation restrictions, as well as other kinematic cuts imposed in experimental analyses of the prompt photon events at the HERA collider. In this section we study effects of cuts applied in the analysis of the ZEUS Collaboration [42], where the initial γ fractional momentum and the final γ transverse energy and rapidity are required to be in the range: $0.2 \leq y \leq 0.9$, $5 \leq E_T^\gamma \leq 10$ GeV and $-0.7 \leq \eta^\gamma \leq 0.9$, respectively. The influence of the limited y range is shown in Fig. 4.3. The cross section (solid line) is strongly reduced, by 30-85%, in the positive rapidity region. At negative rapidities the change due to the y -cut is weaker: 5-10% at $-1.2 < \eta^\gamma \leq -0.4$ and 10-30% at other negative rapidities. Separately we show the results obtained without including the box subprocess (dashed line). The box diagram contributes mainly in the rapidity region between -1 and 3. After imposing the y -cut it is important in the narrower region, from -1 to 1. The influence of the y -cut can be read also from the third row in Tab. 2: the Born contribution is reduced 3.5 times in comparison with the results obtained without the y -cut (the second row), while other contributions are suppressed less, roughly by a factor of 2.

The results obtained for the isolated photon with the y -cut and in addition with the cut on the final photon rapidity, $-0.7 \leq \eta^\gamma \leq 0.9$, are presented in the last row of Tab. 2. The restriction on η^γ decreases the contributions of all subprocesses approximately by a factor of 2, except for the contribution of processes with resolved initial γ and fragmentation into final γ which is reduced almost 3 times.

The influence of various cuts on the x_γ -distribution is illustrated in Fig. 4.4. This

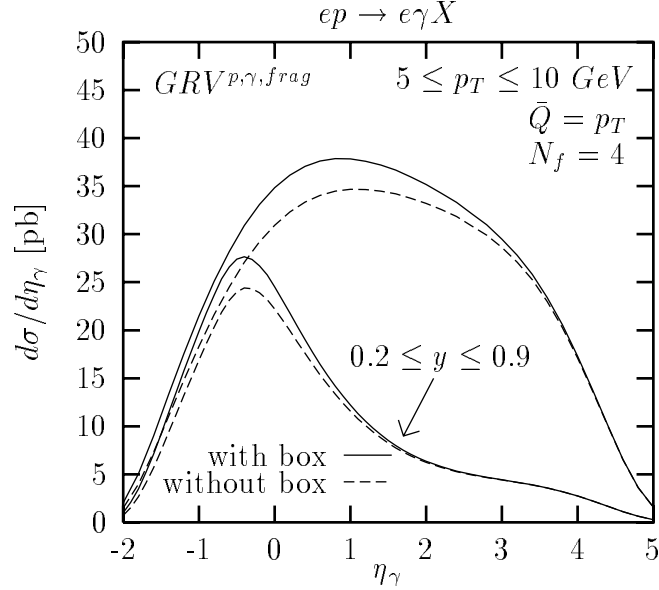


Figure 4.3: The differential cross section $d\sigma/d\eta_\gamma$ for the photoproduction of the isolated γ ($\epsilon = 0.1$, $R = 1$) at HERA as a function of the photon rapidity η_γ with (solid lines) and without (dashed lines) the box contribution. The results are obtained with imposed y -cut ($0.2 \leq y \leq 0.9$) and without this cut. The photon transverse energy, $E_T^\gamma \equiv p_T$, is assumed in the range $5 \leq E_T^\gamma \leq 10$ GeV.

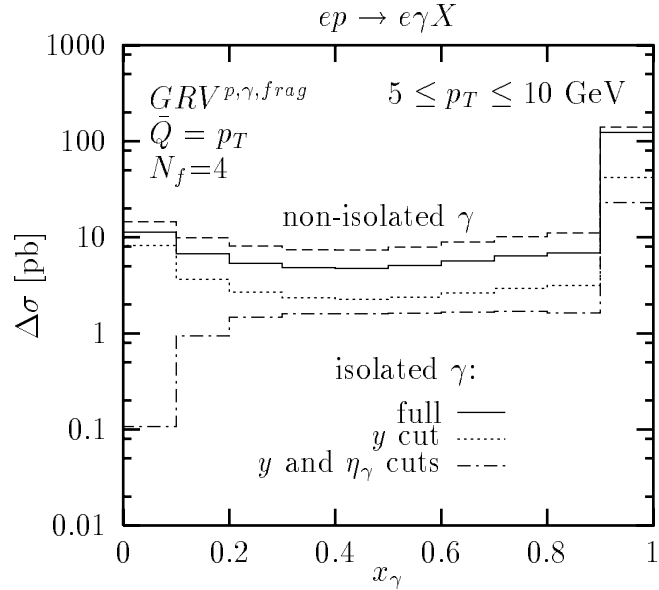


Figure 4.4: The cross section in x_γ bins of the length 0.1 for the photon transverse energy in the range $5 \leq E_T^\gamma \leq 10$ GeV ($E_T^\gamma \equiv p_T$). The results for the non-isolated γ integrated over the whole range of y and η_γ are shown with the dashed line. The solid line represents results integrated over the whole range of y and η_γ for the isolated γ with $\epsilon = 0.1$ and $R = 1$. Results with additional cuts in the isolated γ cross section are shown with: dotted line ($0.2 \leq y \leq 0.9$) and dashed-dotted line ($0.2 \leq y \leq 0.9$, $-0.7 \leq \eta_\gamma \leq 0.9$).

distribution is scheme-dependent, nevertheless it is important to study the resolved photon contributions in the chosen renormalization scheme. Such an analysis was performed for the first time in our paper [30]. Note that $x_\gamma < 1$ and $x_\gamma = 1$ correspond to processes with the resolved or direct initial photon, respectively. So, the cross section in the last bin in Fig. 4.4, $0.9 < x_\gamma \leq 1$, contain the contributions of both types of processes, while the cross sections in other bins, $x_\gamma \leq 0.9$, consists of the resolved photon contribution alone. In particular we see in Fig. 4.4 that the isolation and the energy cut reduce considerably the cross section at large and medium x_γ , while the cross section at x_γ below 0.1 is reduced less. On the other hand, the small x_γ contributions are strongly, by two orders of magnitude, diminished by the photon rapidity cut. This shows that measurements in the central η^γ region ($-0.7 \leq \eta^\gamma \leq 0.9$) are not too sensitive to the parton densities in the photon at small x_γ region.

4.4.3 Dependence on the choice of the renormalization scale

In order to estimate the contribution due to missing higher order terms, the influence of the choice of the renormalization/factorization scale μ is studied for the η^γ distribution. In Fig. 4.5 the results obtained with and without the y -cut are shown. When changing μ from E_T^γ to $2 \cdot E_T^\gamma$ ($E_T^\gamma/2$) the cross section increases (decreases) at rapidities below ~ 1 and decreases (increases) at higher rapidity values. Only at high rapidities, $\eta^\gamma > 3$, the dependence on a choice of the scale is strong, above 10%, however here the cross section is relatively small. In the wide kinematic range, $-2 < \eta^\gamma < 2$, the relative differences between the results obtained (with and without the y -cut) for $\mu = E_T^\gamma$ and for $\mu = 2 \cdot E_T^\gamma$ or $E_T^\gamma/2$ are small and do not exceed 6%. Around the maximum of

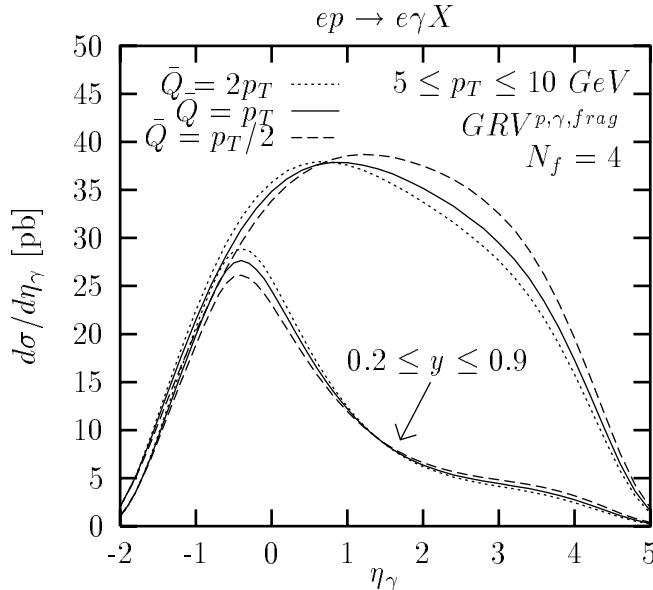


Figure 4.5: The cross section $d\sigma/d\eta^\gamma$ for $5 \leq E_T^\gamma \equiv p_T \leq 10$ GeV and $\mu \equiv \bar{Q} = E_T^\gamma/2$ (dashed line), E_T^γ (solid line) and $2 \cdot E_T^\gamma$ (dotted line). The results obtained without and with the y -cut, $0.2 \leq y \leq 0.9$, are shown.

the cross section at rapidities $-1 \leq \eta^\gamma \leq 0$ these differences are 4-6%. This small sensitivity of the results to the change of the scale is important since it may indicate that the contribution from neglected NNLO and higher order terms is not significant. This is important for a comparison (see below, and in Sec. 5.5.3 and 6.2.4) with other NLO calculations using other set of diagrams and, in particular, including the $\mathcal{O}(\alpha_S)$ corrections to the processes with the resolved photon which are not included in our calculation.

Note that individual contributions are strongly dependent on the choice of μ , e.g. results for the processes with the resolved photon vary by ± 10 -20% at rapidities $\eta^\gamma \leq 1$ while the $\mathcal{O}(\alpha_S)$ corrections to the Born diagram vary by a factor of a few and in some kinematic ranges they even change sign (not shown). The results are much more stable when the sum of the resolved photon processes and the $\mathcal{O}(\alpha_S)$ corrections to the Born process is included (compare the discussion in Sec. 2.1.2).

4.4.4 Comparison with the ZEUS data

The results of the first measurements of the isolated prompt photon cross section (with no jet requirements) in photoproduction events at the HERA collider have been published in [42]. Below we compare of our predictions with these data.

E_T^γ, N_f

Fig. 4.6a shows the distribution of the photon transverse energy, E_T^γ , for various number of active massless quarks, N_f . The predictions for $N_f = 4$ and 5 are in agreement with most of the experimental points but tend to lie slightly below the data. The difference between predictions for $N_f = 4$ and $N_f = 5$ is very small due to the fourth power of electric charge characterizing processes with two photons. The contribution of the charm quark is an order of magnitude larger than the contribution of beauty and the predictions for $N_f = 3$ are significantly below the predictions for $N_f = 4$ and below the data, confirming the need to include the charm contribution in the calculations.

η^γ, N_f

A similar comparison between the predictions and the data, now for the distribution of the photon rapidity, η^γ , is shown in Fig. 4.6b. A good description of the data is obtained for $N_f=4, 5$ in the rapidity region $0.1 \leq \eta^\gamma \leq 0.9$. For $-0.7 \leq \eta^\gamma \leq 0.1$ our predictions lie mostly below the experimental points. Note that this disagreement between predicted and measured cross sections is also observed for calculations of Gordon [31] and of Fontannaz, Guillet and Heinrich [29] as well as for Monte Carlo simulations [42, 45]. In order to find the source of such a disagreement various checks have been performed, discussed below.

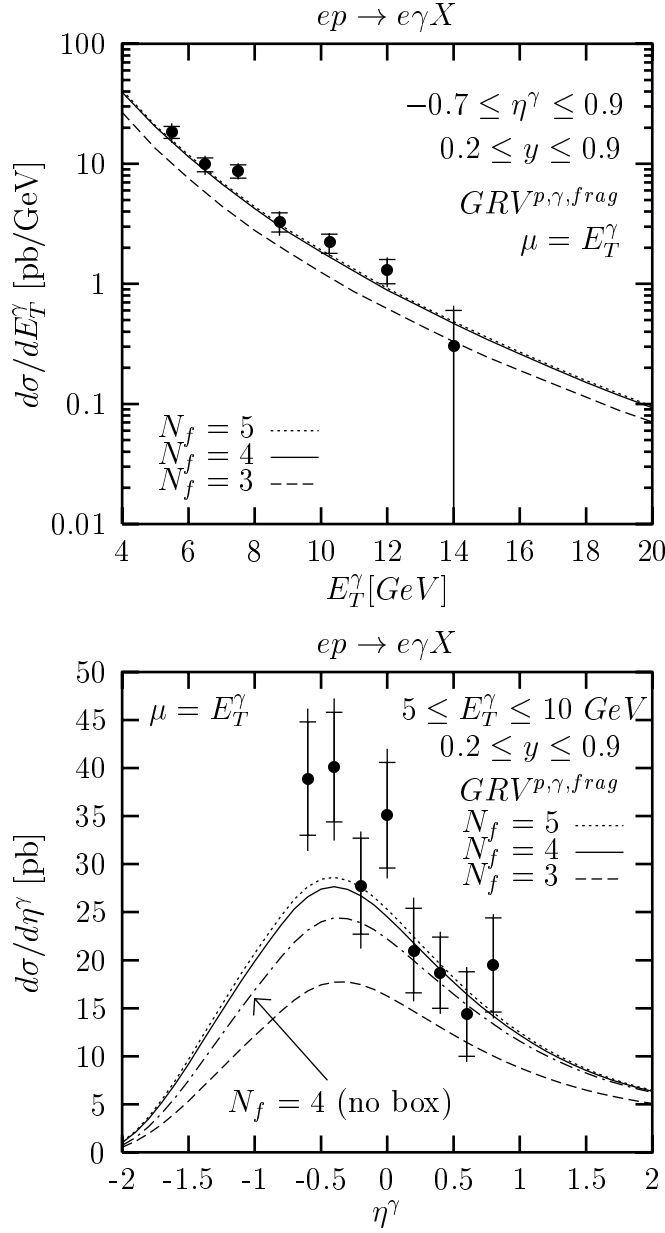


Figure 4.6: The cross section $d\sigma/dE_T^\gamma$ (a) and $d\sigma/d\eta^\gamma$ (b) with various numbers of active massless flavors: $N_f = 3$ (dashed lines), 4 (solid lines) and 5 (dotted lines), compared to the ZEUS data [42]. The result without the box contribution is also shown for $N_f = 4$ (dot-dashed line)

η^γ , integrated σ , $\mathcal{O}(\alpha^2\alpha_S^2)$

First, we study the size of $\mathcal{O}(\alpha^2\alpha_S^2)$ contributions included by us. In Fig. 4.6b we present separately an effect due to the box subprocess (for $N_f = 4$). One can see that the box term enhances considerably the cross section in the measured rapidity region. Its contribution to the integrated cross section is equal to 10%, see Tab. 2 (fourth line). The processes with resolved photon and fragmentation also give a no-negligible

contribution, although roughly two times smaller than the box one (Tab. 2, fourth line). We conclude, that taking into account of these $\mathcal{O}(\alpha^2\alpha_s^2)$ contributions improves the description of the data.

$\eta^\gamma, f_\gamma, \mu$

Next, we study the dependence on the parton densities. The predictions obtained using three different NLO parton densities in the photon (ACFGP $^\gamma$ [24], GRV $^\gamma$ [72] and GS $^\gamma$ [81]) are presented for $N_f = 4$ in Fig. 4.7a ($\mu = E_T^\gamma$) and in Fig. 4.7b ($\mu = 2E_T^\gamma$) together with the ZEUS data [42]. The results based on ACFGP $^\gamma$ and GRV $^\gamma$ parametrizations differ by less than 4% at rapidities $\eta^\gamma < 1$ (at higher η^γ the differences are bigger), and both give a good description of the data in the rapidity range $0.1 \leq \eta^\gamma \leq 0.9$ (for $\mu = E_T^\gamma$ and $\mu = 2E_T^\gamma$). For $-0.7 \leq \eta^\gamma \leq 0.1$ none of the predictions is in agreement with the measured cross section.

For $\mu=E_T^\gamma$ (Fig. 4.7a) the GS $^\gamma$ distribution leads to results considerably below ones obtained using ACFGP $^\gamma$ and GRV $^\gamma$ densities, especially in the rapidity region from roughly -1 to 1, where the differences are up to 14%. This difference between the GS $^\gamma$ and other considered herein parton parametrizations is mainly due to their different treatment of the charm quark in the photon, namely in the GS $^\gamma$ approach the charm quark is absent for μ^2 below 50 GeV 2 . Since we take $5 \leq \mu = E_T^\gamma \leq 10$ GeV, and the most important contribution to the cross section arises from the lower E_T^γ region (see Fig. 4.6a), the μ^2 value usually lies below the GS $^\gamma$ charm quark threshold. As a consequence, the predictions based on GS $^\gamma$ have strongly suppressed contribution of subprocesses involving charm from the photon - contrary to GRV $^\gamma$ and ACFGP $^\gamma$ predictions where the charm threshold is assumed at lower μ^2 .

All the considered parton parametrizations give similar description of the data when the scale is changed to $\mu = 2E_T^\gamma$, see Fig. 4.7b. Here the calculation corresponds to μ^2 which is always above 50 GeV 2 and the charm density in the GS $^\gamma$ parametrization is non-zero, as in other parametrizations.

$\eta^\gamma, f_p, D_\gamma$

We have also studied the dependence of our results on a choice of the parton densities in the proton and parton fragmentation into the photon (not shown). The MRST1998 p (set ft08a) [74] and CTEQ4M p [77] NLO densities in the proton give predictions lower than GRV p [71] NLO densities by 4-7% and 4-6% at negative rapidities. At positive rapidities the cross sections calculated using MRST1998 p , CTEQ4M p and GRV p vary among one another by less than 4%. Results for the isolated photon production are not too sensitive to the parton-to-photon fragmentation function. For rapidity ranging from -1 to 4 the cross section obtained with DO frag (LO) [15] fragmentation function is 2 – 4% lower than the cross section based on GRV frag (NLO) [73] parametrization. Only at minimal ($\eta^\gamma < -1$) and maximal ($4 < \eta^\gamma$) rapidity values this difference is larger, being at a level of 4 – 8%. All these parton densities in the proton and fragmentation functions lead to similar descriptions of the data.

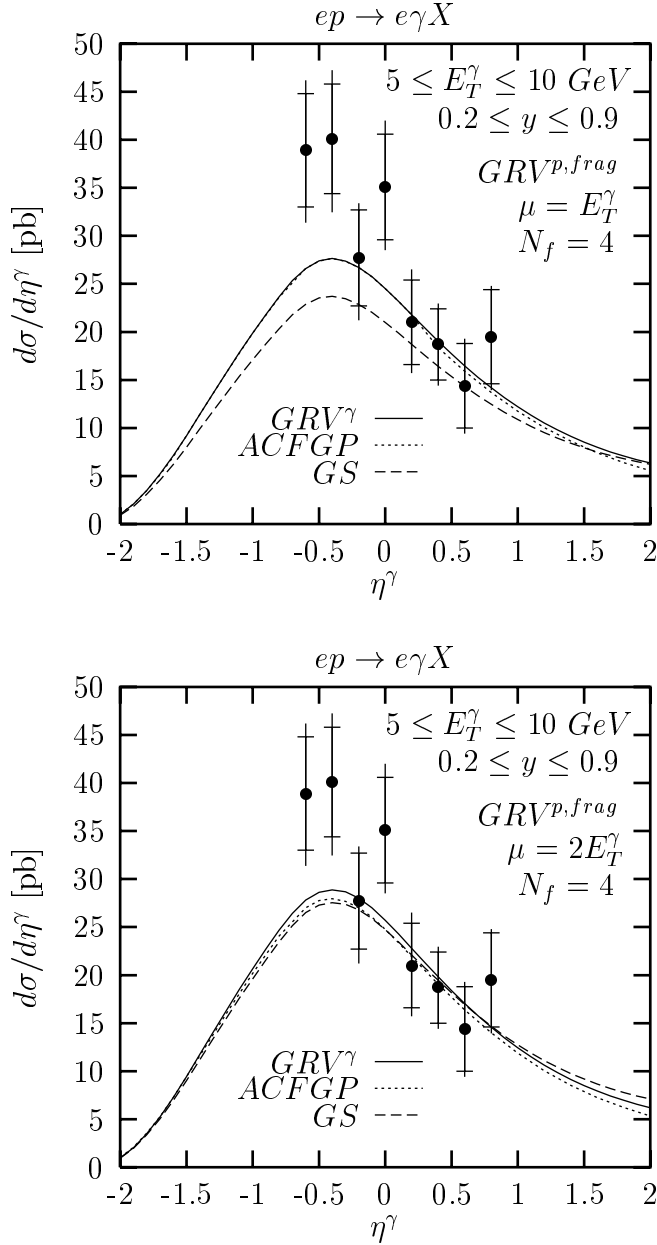


Figure 4.7: The cross section $d\sigma/d\eta^\gamma$ in the range $5 < E_T^\gamma < 10$ GeV for the renormalization/factorization scale $\mu = E_T^\gamma$ (a) and $\mu = 2 \cdot E_T^\gamma$ (b). The GRV^γ [72] (solid line), $ACFGP^\gamma$ [24] (dotted line) and GS^γ [81] (dashed line) parton densities in the photon were used together with GRV^p densities in the proton [71] and GRV^{frag} fragmentation [73].

η^γ, y

In Fig. 4.8 our predictions are compared to the ZEUS data divided into three ranges of the initial photon fractional momentum y . This allows to establish that the above discussed discrepancy between the data and the predictions for $\eta^\gamma < 0.1$ is coming mainly from the low, $0.2 < y < 0.32$, and medium, $0.32 < y < 0.5$, y region. In the

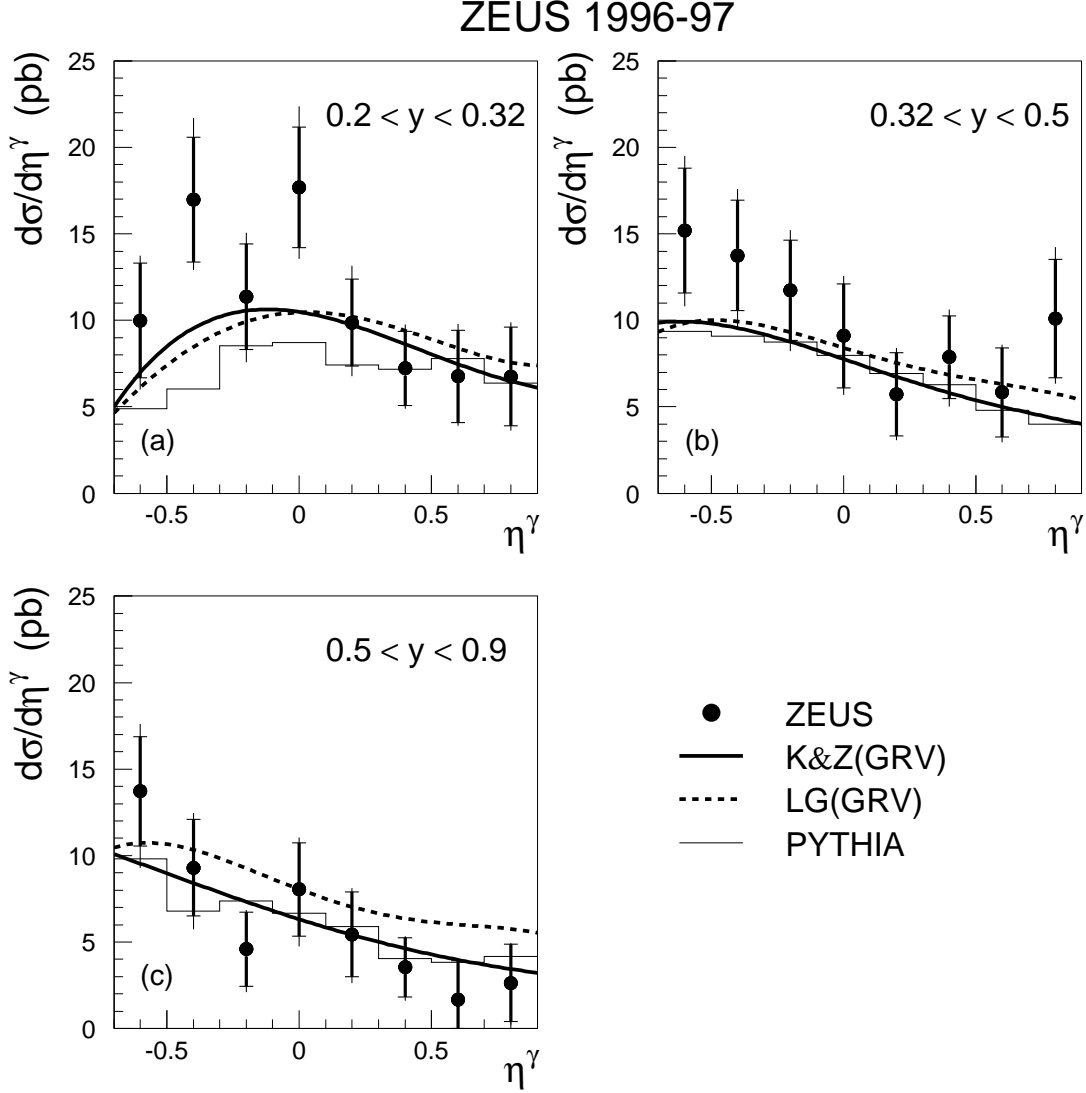


Figure 4.8: The cross section $d\sigma/d\eta^\gamma$ for three ranges of y : $0.2 < y < 0.32$ (a), $0.32 < y < 0.5$ (b) and $0.5 < y < 0.9$ (c). The predictions of K&Z [30] and LG [31] are compared with the ZEUS Collaboration data [42]. The figure is taken from [42].

high y region, $0.5 < y < 0.9$, a good agreement is obtained.

summary of comparison with data

To summarize, there are discrepancies between the predictions and the ZEUS data [42] at $\eta^\gamma < 0.1$ and $y < 0.5$. The variation of theoretical parameters and parton densities do not improve the description of the data. Note that there are also discrepancies between predictions and the new H1 data for the prompt photon production at HERA [49] (Chapter 5). So far the source of these discrepancies is not established.

Finally, it is worth mention that in Ref. [43] there was performed an analysis, in which our computer program for the prompt photon production at HERA [30] was

modified: the parton densities in the photon for $x_\gamma > 0.8$ were multiplied by a factor of 2 or 3. For doubled f_γ at $x_\gamma > 0.8$ the description of the data was much improved, and for tripled f_γ at $x_\gamma > 0.8$ a good agreement with the ZEUS data was found in the whole range of η^γ . This agreement is probably accidental, but it can also indicate a need of improvement of the parton densities in the photon at x_γ close to 1 [43].

4.4.5 Comparison with other QCD predictions (LG)

The calculation of L. Gordon (LG) [31] for the photoproduction of isolated photons at HERA contains the $\mathcal{O}(\alpha_S)$ corrections to the processes with the resolved initial photon, which are not included in our calculation (Chapter 2). On the other hand, we include the box diagram (Fig. 2.11) neglected in [31]. The $\mathcal{O}(\alpha_S^2)$ diagrams with resolved initial γ and fragmentation into final γ , as well as other diagrams shown in Figs. 2.1-2.4 and 2.7-2.10, are taken into account in both calculation.

The LG calculation applies the MRST^p(NLO) [74] parton distributions in the proton which give predictions 4% lower on average than GRV^p(NLO) [71] parametrization used by us (Sec. 4.4.4). Both calculations use GRV $^\gamma$ [72] and GS $^\gamma$ [81] parton densities in the photon. Since the GS $^\gamma$ densities lead to worse description of the data than the GRV $^\gamma$ ones (see Sec. 4.4.4), below we discuss the predictions obtained using the GRV $^\gamma$ parametrization.

The comparison between the predictions of Krawczyk and Zembrzuski (K&Z) [30], predictions of Gordon (LG) [31] and the data was performed by the ZEUS Collaboration [42]. Results of this analysis are shown in Figs. 4.8, 4.9 and 4.10².

The LG predictions for $d\sigma/dE_T^\gamma$ cross section are higher than ours in the whole presented range of transverse momentum, $5 \leq E_T^\gamma \leq 15$ GeV (Fig. 4.9). Both calculations agree with the data within large experimental errors, although the K&Z predictions tend to lie slightly below the data.

For $d\sigma/d\eta^\gamma$ the biggest differences are at $\eta^\gamma=0.9$ where the LG results are about 35% higher than K&Z (Fig. 4.10b). The differences decrease towards negative rapidity values and are negligible at $-0.7 \leq \eta^\gamma < -0.5$. The average difference in the range $-0.7 \leq \eta^\gamma < 0.9$ is about 10%. Both predictions are in disagreement with data at $\eta^\gamma < 0.1$. At $\eta^\gamma > 0.1$ K&Z agrees with the measured cross section but LG tends to lie slightly to high.

For y range limited to low values only, $0.2 < y < 0.32$, the LG cross section is higher than ours by up to 20% at positive η^γ , while at negative η^γ it is lower by up to 10%. (Fig. 4.8a). In this y range, as well as for medium range with $0.32 < y < 0.5$ (Fig. 4.8b), the K&Z and LG calculations lead to similar discrepancies with data at $\eta^\gamma \lesssim 0.1$. For large y values, $0.5 < y < 0.9$, where our predictions agree with data, the LG results are higher than ours by up to 70% at $0.7 < \eta^\gamma < 0.9$ and does not describe the data well (Fig. 4.8c).

²In the comparison between LG [31] and K&Z [30] we consider the predictions presented in the ZEUS paper [42], because the numerical results presented in the original paper [31] are given for different kinematic ranges.

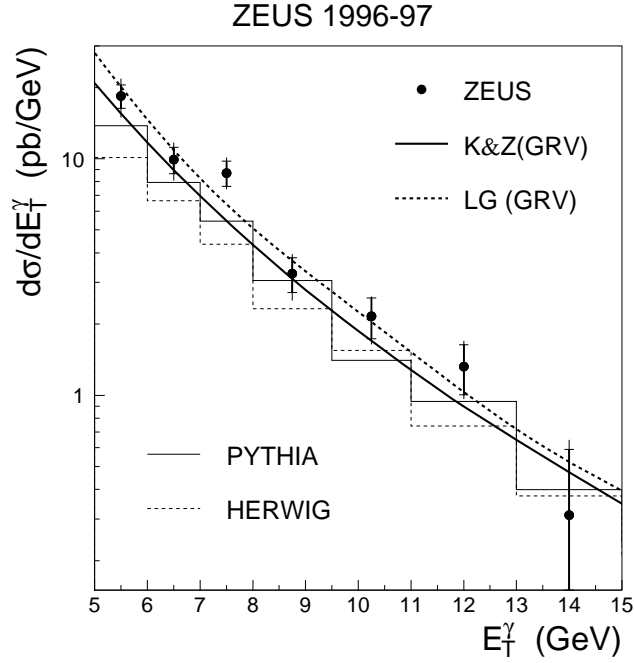


Figure 4.9: The cross section $d\sigma/dE_T^\gamma$ for the photoproduction of isolated photons in the kinematic range $0.2 < y < 0.9$ and $-0.7 \leq \eta^\gamma \leq 0.9$. The predictions of K&Z [30] and LG [31] using GRV $^\gamma$ [72] parton distributions in the photon, are compared with the ZEUS Collaboration data [42]. The Monte Carlo simulations are also shown. The figure is taken from [42].

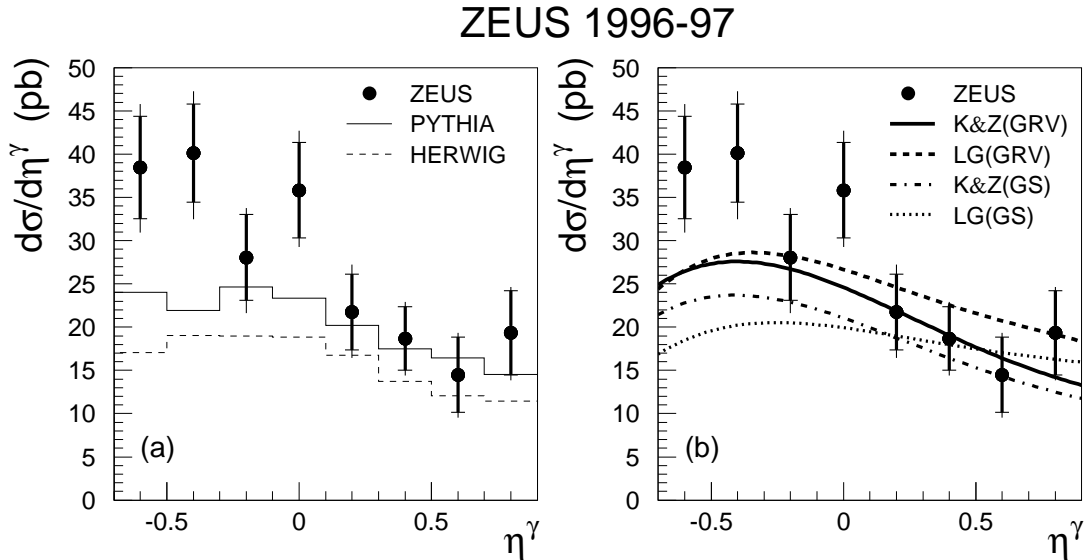


Figure 4.10: As in Fig. 4.9 for the $d\sigma/d\eta^\gamma$ cross section in the range $5 < E_T^\gamma < 10$ GeV. In addition, the predictions of K&Z [30] and LG [31] using GS $^\gamma$ [81] parton densities in the photon are shown. The figure is taken from [42].

To summarize, the differences between both calculations including different sets of diagrams are of order 10%. However there are some kinematic ranges where the differences are larger up to 70% for $0.5 < y < 0.9$ and $0.7 < \eta^\gamma < 0.9$. The experimental errors are too large to conclude which calculation describes better the ZEUS Collaboration data presented in [42]. Nevertheless, for large y region, $0.5 < y < 0.9$, our predictions give a better description of the data.

There is also another NLO calculation for the photoproduction of isolated photons at HERA presented by Fontannaz, Guillet and Heinrich (FGH) [29]. We compare our predictions with predictions of FGH in Secs. 5.4.3 and 6.2.4, where we use the same parton distributions as FGH do. Let us only note here, that in the range considered by the ZEUS group [42], $0.2 < y < 0.9$ and $-0.7 < \eta^\gamma < 0.9$, the FGH predictions obtained using MRST1999^p [75], AFG ^{γ} [79] and BFG ^{$frag$} [83] parametrizations are about 10% higher on average than our predictions obtained using GRV ^{$p,\gamma,frag$} [71, 72, 73] parametrizations. However, for the large y region, $0.5 < y < 0.9$, and for η^γ in the narrowed range $0.7 < \eta^\gamma < 0.9$ the FGH predictions are about 50% higher.

The dependence of our predictions on the renormalization/factorization scale μ is about $\pm 5\%$ in the kinematic range considered by the ZEUS Collaboration [42] and it is true also for $0.5 < y < 0.9$. So, we could expect that the size of higher order contributions is not large in this particular region of y as well. However we found that the difference between K&Z and LG (FGH) is up to 70% (50%) for $0.5 < y < 0.9$ and $0.7 < \eta^\gamma < 0.9$. To understand the origin of this large difference we should know the dependence of the LG and FGH predictions on the scale μ in this particular range, which however was not presented in [31] and [29]³. If this dependence was large, it could be a confirmation of our supposition that the $\mathcal{O}(\alpha_S)$ corrections to the processes with resolved photons should be included together with the $\mathcal{O}(\alpha_S^2)$ corrections to the Born process in next-to-next-to-leading order (NNLO) accuracy and, that they should not be included in NLO to avoid possible uncertainties due to the choice of μ .

³The dependence on the choice of the scale μ was studied in [31, 29] for the total cross sections, i.e. cross sections integrated within considered kinematic ranges. The total cross section of FGH for the prompt photon production varies by about $\pm 4\%$. The total cross section of LG for the prompt photon plus jet production varies by $\pm 3\%$.

Chapter 5

Isolated photon production. Exact implementation of isolation cuts

In the small cone approximation, discussed in the previous section, one obtains simple analytical formulae which are easy to implement in numerical calculations for the isolated photon production. The accuracy of this approximation is good [96, 27, 98, 31], however the method has one drawback: it does not allow to obtain any predictions for the rapidity or transverse energy of the jet (or jets) produced together with the photon. This is because the formulae (4.20-4.23) and (D.21,D.22) used in the small cone approximation are integrated over all allowed momenta of final particles other than the photon.

In order to compare predictions with the existing data not only for the photon observed in the final state but also for the $ep \rightarrow e\gamma \text{ jet } X$ process, there is a need of more general technique allowing to consider both the photon and the jet momenta in any kinematic range for which the data are taken. An introduction of such a technique, based on the division (*slicing*) of the three-body phase space [100]-[107], [29, 31, 32] is presented below and was discussed in the paper of Zembrzuski and Krawczyk [33]. Note, that our method of the division of the phase space [33] slightly differs from methods applied in other papers.

The use of the *phase space slicing* allows to calculate the cross section in an exact way, i.e. with no assumption that the isolation cone is small. We take some cross section and matrix elements formulae from the literature and derive all the missing expressions, see Secs. 5.1-5.3 and Appendices B-D. The comparison between exact predictions for the $ep \rightarrow e\gamma X$ cross section and the predictions based on the small cone approximation, as well as the comparison with the new H1 data [49] for the $ep \rightarrow e\gamma X$ reaction, are presented in Sec. 5.4.

The slicing of the phase space is applied to obtain predictions for the $ep \rightarrow e\gamma \text{ jet } X$ cross section, and comparing them with corresponding H1 data [49], in Chapter 6.

5.1 Cross section formulae

The general formula for the isolated photon (or isolated photon + jet) cross section is obtained from Eqs. (3.1-3.5) integrated over the whole range of x and x_γ and over z within the region given by Eq. (4.11), namely:

$$d\sigma^{\gamma p \rightarrow \gamma(jet)X} = \sum_{q,\bar{q}} \int_0^1 dx f_{q/p}(x, \mu^2) d\sigma^{\gamma q \rightarrow \gamma q} + \int_0^1 dx f_{g/p}(x, \mu^2) d\sigma^{\gamma g \rightarrow \gamma g} \quad (5.1)$$

$$+ \sum_{a=q,\bar{q},g} \int_0^1 dx_\gamma \sum_{b=q,\bar{q},g} \int_0^1 dx f_{a/\gamma}(x_\gamma, \mu^2) f_{b/p}(x, \mu^2) d\sigma^{ab \rightarrow \gamma d} \quad (5.2)$$

$$+ \sum_{b=q,\bar{q},g} \int_0^1 dx \sum_{c=q,\bar{q},g} \int_{1/1+\epsilon}^1 \frac{dz}{z^2} f_{b/p}(x, \mu^2) D_{\gamma/c}(z, \mu^2) d\sigma^{\gamma b \rightarrow cd} \quad (5.3)$$

$$+ \sum_{a=q,\bar{q},g} \int_0^1 dx_\gamma \sum_{b=q,\bar{q},g} \int_0^1 dx \sum_{c=q,\bar{q},g} \int_{1/1+\epsilon}^1 \frac{dz}{z^2} f_{a/\gamma}(x_\gamma, \mu^2) f_{b/p}(x, \mu^2) \\ \cdot D_{\gamma/c}(z, \mu^2) d\sigma^{ab \rightarrow cd} \quad (5.4)$$

$$+ \sum_{q,\bar{q}} \int_0^1 dx \left\{ f_{q/p}(x, \mu^2) \left[d\sigma_{\alpha_S}^{\gamma q \rightarrow \gamma q} + d\sigma_{\alpha_S}^{\gamma q \rightarrow \gamma q g} \right] + f_{g/p}(x, \mu^2) d\sigma_{\alpha_S}^{\gamma g \rightarrow \gamma q \bar{q}} \right\}, \quad (5.5)$$

where the partonic cross sections in (5.1-5.4) are given by Eqs. (B.1-B.22). Note, that these partonic cross sections are not integrated over the photon momentum, so they allow to obtain various types of differential cross sections (e.g. $d\sigma/d\eta^\gamma$ or $d\sigma/dE_T^\gamma$) in any range of the final photon or final parton momenta. This is due to the fact that in $2 \rightarrow 2$ processes the parton momentum is determined, in the centre-of-mass system, by the final photon momentum. The isolation is taken into account simply through the lower limit of the integration over z .

An inclusion of the isolation in calculations of the $\mathcal{O}(\alpha_S)$ corrections (5.5) is more complicated, since one needs to restrict the final momenta of two partons, and to take care of a cancellation and factorization of singularities.

5.2 Division of phase space

The $\mathcal{O}(\alpha_S)$ corrections (5.5) include $2 \rightarrow 3$ processes (4.7) and the virtual gluon corrections. The squared matrix elements of these processes contain infrared and collinear singularities [18, 25], see Appendix D. In order to obtain numerical predictions for the isolated photon production with arbitrary kinematic cuts, one needs to isolate these singularities, and cancel or factorize them in such a way, that an integration over any range of final momenta is still possible [29, 31]. The standard method to achieve this goal is to divide the phase space (Appendix C) into a few parts [100]-[107], [29, 31, 32], and herein this technique is adopted.

Let us assume that θ_{ji} is an angle between the momentum of the final parton d_i (see Eq. (4.7)) and the momentum of an initial particle j , where $j = e, p$ ¹. Let us also define the distance, $R_{\gamma i}$, between the d_i parton and the final photon:

$$R_{\gamma i} = \sqrt{(\eta_{d_i} - \eta_\gamma)^2 + (\phi_{d_i} - \phi_\gamma)^2}. \quad (5.6)$$

We define the parts of the phase space in the following way:

- Part 1. In the first part the variable w (see Appendix A.1) is in the range $w_{cut} \leq w \leq 1$, where w_{cut} is an arbitrary parameter close to 1: $0 < 1 - w_{cut} \ll 1$. This region of the phase space contains all types of NLO corrections: the virtual gluon exchange, the real gluon emission, and the process $\gamma g \rightarrow \gamma q \bar{q}$. The virtual gluon exchange is a $2 \rightarrow 2$ process, while the other ones are of $2 \rightarrow 3$. However, for w close to 1, $w_{cut} < w \leq 1$, the two final partons in the $2 \rightarrow 3$ processes are almost collinear or/and one of the final partons is soft. For w_{cut} sufficiently close to 1 the kinematics of the $2 \rightarrow 3$ processes is almost the same as in the $2 \rightarrow 2$ case:

$$\gamma b \rightarrow \gamma d \quad , \quad d \equiv d_1 + d_2, \quad (5.7)$$

where the “particle” d has four-momentum equal to the sum of four-momenta of the d_i -partons, and its mass is almost zero. The additional restriction $1 - w_{cut} < \epsilon$ is sufficient to ensure that if parton d_1 or d_2 is inside the isolation cone then its energy is smaller than ϵE_γ , so the final photon is isolated.

The other parts of the phase space, Parts 2-5 described below, are defined for $w < w_{cut}$, and contain only $2 \rightarrow 3$ diagrams.

- Part 2. In this region $w < w_{cut}$ and $\theta_{cut} > \min(\theta_{e1}, \theta_{e2})$, where θ_{cut} is a small arbitrary parameter, $\theta_{cut} \ll 1$. Here, one of the final partons has the momentum almost collinear to the momentum of the initial electron and it, for sufficiently small θ_{cut} , does not enter the isolation cone around the photon. The second parton has a large transverse momentum balancing the photon transverse momentum, so the final photon is isolated.
- Part 3. Here $w < w_{cut}$ and $\theta_{cut} > \min(\theta_{p1}, \theta_{p2})$. One of the final partons has momentum almost collinear to the momentum of the proton, and, like in Part 2, the final photon is isolated.
- Part 4. Here $w < w_{cut}$ and $R_{cut} > \min(R_{\gamma 1}, R_{\gamma 2})$, where R_{cut} is a small parameter, $R_{cut} \ll 1$. In this case one of the final partons, say d_1 , is almost collinear to the photon, and the photon is isolated if the transverse momenta obey the inequality (4.1): $E_{Td_1} < \epsilon E_{T\gamma}$.

¹The initial particles a and b in Eq. (4.7) move parallel to the initial electron and proton, respectively.

CHAPTER 5. ISOLATED PHOTON PRODUCTION. EXACT IMPLEMENTATION OF ISOLATION CUTS

- Part 5. The last part is defined as the region in which there are no collinear configurations: $w < w_{cut}$, $\theta_{cut} < \min(\theta_{e1}, \theta_{e2})$, $\theta_{cut} < \min(\theta_{p1}, \theta_{p2})$, and $R_{cut} < \min(R_{\gamma1}, R_{\gamma2})$.

The $\mathcal{O}(\alpha_S)$ corrections (5.5) contain contributions from all parts of the phase space:

$$\left[d\sigma_{\alpha_S}^{\gamma q \rightarrow \gamma q} + d\sigma_{\alpha_S}^{\gamma q \rightarrow \gamma qg} \right] = \left[d\sigma_{\alpha_S(1)}^{\gamma q \rightarrow \gamma q} + d\sigma_{\alpha_S(1)}^{\gamma q \rightarrow \gamma qg} \right] + \sum_{i=2,3,4,5} d\sigma_{\alpha_S(i)}^{\gamma q \rightarrow \gamma qg} \quad (5.8)$$

$$d\sigma_{\alpha_S}^{\gamma g \rightarrow \gamma q\bar{q}} = \sum_{i=1,2,3,4,5} d\sigma_{\alpha_S(i)}^{\gamma g \rightarrow \gamma q\bar{q}} \quad (5.9)$$

In numerical calculations for Part 1 the formulae (D.21) and (D.22) (the same as for the inclusive photon case) can be used with the requirement $w > w_{cut}$. In these formulae all the soft gluon singularities present in the virtual gluon and real gluon corrections are canceled, and all the collinear singularities are factorized into the parton densities.

Parts 2-5 contain no contribution from the virtual gluon exchange, and no soft gluon singularities. Analytical expressions for cross sections corresponding to Parts 2, 3, and 4 are derived in Appendix D, and will be presented in next section.

The cross section in Part 5 has no singularities at all, and one can perform an exact numerical integration over final four-momenta in any kinematic range, including isolation restrictions and other cuts. For this purpose the general formulae (C.13) and (D.1-D.20) with $\varepsilon = 0$ are used.

The presented method of the division of the phase space differs from the methods applied in other calculations for the photoproduction of isolated photons at HERA [31, 29, 32], since we use the cut-off parameter w_{cut} not used before. Our method allows to obtain relatively the simplest analytical singular-free formulae in all parts of the phase space, as all the singularities due to the soft gluons (or gluons collinear to the final quark) are collected in one part of the phase space, i.e. in Part 1, and this part is chosen this way that the formulae for the non-isolated photon production can be used. The unintegrated over momenta formulae used in Part 5 are also the same as for the non-isolated photon case, and in Parts 2-4 the relatively simple expressions for collinear configurations are applied.

The drawback of our method is that the numerical calculations are not stable if the integration over final momenta in Part 5 is performed in the laboratory ep frame or in the rest frame of the initial photon and parton. However, we found that the calculations were sufficiently stable if the rest frame of the final partons was chosen instead.

The predictions should not depend on a choice of unphysical cut-off parameters, $1 - w_{cut}$, θ_{cut} and R_{cut} , if they are small enough. On the other hand, they can not be too small, since for very low values of these parameters large numerical errors occur. The results presented in Secs. 5.4 and 6.2 are obtained with $1 - w_{cut} = \theta_{cut} = R_{cut} = 0.01$ where the angle θ_{cut} is defined in the centre of mass of the initial photon and the initial parton (despite the fact that the numerical calculation is performed in other frame). We have checked that the change of the predictions due to the variation of these parameters is negligible, below 1%, if they are taken in the range $10^{-4} \leq 1 - w_{cut} \leq 0.03$, $10^{-4} \leq \theta_{cut} \leq 0.05$ and $10^{-4} \leq R_{cut} \leq 0.05$.

5.3 Analytical results

Below we present analytical results for cross sections for $2 \rightarrow 3$ processes including various collinear configurations described in Sec. 5.2. These results are obtained (for the details see Appendices C, D) using the standard factorization procedure, which for the inclusive (non-isolated) photon production in the ep scattering was discussed in Ref. [18, 25]. All the collinear singularities appearing in the calculations are factorized into parton densities in the photon (Part 2), proton (Part 3), and into fragmentation functions (Part 4).

Some of the presented below “splitting functions” P have been already presented in Ref. [96], where they were used to calculate in the small cone approximation the cross section for the isolated photon production in the hadron-hadron collision (see also e.g. [101, 103, 104]). Nevertheless, we find it useful to present herein compact analytical formulae for all the relevant cross sections for the isolated photon production in the ep scattering. The partonic cross sections for the $2 \rightarrow 3$ processes in the parts of the phase space labeled in Sec. 5.2 as Part 2, 3 and 4 have the form:

$$d\sigma_{\alpha_S(2)}^{\gamma g \rightarrow \gamma q \bar{q}} = \Theta(s + t + u) \int_0^1 d\sigma^{qg \rightarrow \gamma q}(\xi s, \xi t, u) P_{\gamma \rightarrow q \bar{q}}(\xi, y E_e(1 - \xi) \theta_{cut}) d\xi, \quad (5.10)$$

$$d\sigma_{\alpha_S(2)}^{\gamma q \rightarrow \gamma q g} = \Theta(s + t + u) \int_0^1 d\sigma^{q \bar{q} \rightarrow \gamma g}(\xi s, \xi t, u) P_{\gamma \rightarrow q \bar{q}}(\xi, y E_e(1 - \xi) \theta_{cut}) d\xi, \quad (5.11)$$

$$d\sigma_{\alpha_S(3)}^{\gamma q \rightarrow \gamma q g} = \Theta(s + t + u) \int_0^1 d\sigma^{\gamma q \rightarrow \gamma q}(\xi s, t, \xi u) P_{q \rightarrow q g}(\xi, x E_p(1 - \xi) \theta_{cut}) d\xi, \quad (5.12)$$

$$d\sigma_{\alpha_S(3)}^{\gamma g \rightarrow \gamma q \bar{q}} = \Theta(s + t + u) \int_0^1 d\sigma^{\gamma q \rightarrow \gamma q}(\xi s, t, \xi u) P_{g \rightarrow q \bar{q}}(\xi, x E_p(1 - \xi) \theta_{cut}) d\xi, \quad (5.13)$$

$$d\sigma_{\alpha_S(4)}^{\gamma q \rightarrow \gamma q g} = \Theta\left(\frac{s + t + u}{t + u} + \epsilon\right). \quad (5.14)$$

$$\cdot \Theta(s + t + u) \int_0^1 d\sigma^{\gamma q \rightarrow q g}\left(s, \frac{t}{\xi}, \frac{u}{\xi}\right) P_{q \rightarrow \gamma q}\left(\xi, E_T^\gamma(1 - \xi) R_{cut}\right) \frac{d\xi}{\xi^2}, \quad (5.15)$$

$$d\sigma_{\alpha_S(4)}^{\gamma g \rightarrow \gamma q \bar{q}} = \Theta\left(\frac{s + t + u}{t + u} + \epsilon\right). \quad (5.16)$$

$$\cdot \Theta(s + t + u) \int_0^1 d\sigma^{\gamma g \rightarrow q \bar{q}}\left(s, \frac{t}{\xi}, \frac{u}{\xi}\right) P_{q \rightarrow \gamma q}\left(\xi, E_T^\gamma(1 - \xi) R_{cut}\right) \frac{d\xi}{\xi^2}, \quad (5.17)$$

where $\Theta(\frac{s+t+u}{t+u} + \epsilon)$ includes the isolation restrictions (4.1), the partonic cross sections for the $2 \rightarrow 2$ processes are given in Appendix B and the functions P are given by

$$P_{q \rightarrow \gamma q}(\xi, E_\perp) = \frac{\alpha}{2\pi} e_q^2 \left\{ \frac{1 + (1 - \xi)^2}{\xi} \ln \frac{E_\perp^2}{\mu^2} + \xi \right\}, \quad (5.18)$$

$$P_{\gamma \rightarrow q \bar{q}}(\xi, E_\perp) = 3 \frac{\alpha}{2\pi} e_q^2 \left\{ [\xi^2 + (1 - \xi)^2] \ln \frac{E_\perp^2}{\mu^2} + 1 \right\}, \quad (5.19)$$

$$P_{q \rightarrow qg}(\xi, E_\perp) = \frac{4}{3} \frac{\alpha_S}{\alpha e_q^2} P_{q \rightarrow \gamma q}(1 - \xi, E_\perp), \quad (5.20)$$

$$P_{g \rightarrow q \bar{q}}(\xi, E_\perp) = \frac{1}{6} \frac{\alpha_S}{\alpha e_q^2} P_{\gamma \rightarrow q \bar{q}}(\xi, E_\perp). \quad (5.21)$$

The variable ξ in the functions $P_{a \rightarrow bc}(\xi, E_\perp)$ stands for the fraction of the energy of the particle a taken by the particle b : $E_b = \xi E_a$. The variable E_\perp is the maximal possible (for given θ_{cut} or R_{cut}) momentum of the particle c perpendicular to the momentum of the particle a : $E_\perp = \max |\vec{p}_c \times \vec{p}_a| / |\vec{p}_a|$. The results (5.10-5.21) are obtained with the assumption that θ_{cut} and R_{cut} are small, see Appendices C and D for details.

Note, that the integration over ξ in Eqs. (5.10-5.17) is trivial as the $2 \rightarrow 2$ partonic cross sections, $d\sigma^{ab \rightarrow cd}(s, t, u)$, contain the $\delta(s + t + u)$ function, see Eq. (B.1). The expressions (5.15) and (5.17) are equivalent to the expressions (4.20) and (4.22) for the subtraction terms used in the small cone approximation (Sec. 4.2).

The cut-off parameter R_{cut} is chosen in a Lorentz-invariant form (Sec. 5.2), but the parameter θ_{cut} depends on the choice of the frame of reference. It can be defined in any frame of reference provided that the energies yE_e and xE_p in Eqs. (5.10-5.13) are given in the same frame. In numerical calculations we use the expressions (5.10-5.13) with θ_{cut} defined in the centre of mass system of the initial photon and the initial parton, where $yE_e = xE_p$.

5.4 Numerical results and discussion

The predictions for the photoproduction of the prompt photons at the HERA collider are obtained with parameters and parton densities specified in Sec. 2.2. For a comparison with the H1 Collaboration data, kinematic ranges used in [49] are applied: the fraction of the electron energy transferred to the photon is restricted to the range $0.2 < y < 0.7$, the final photon rapidity and transverse energy are taken in the limits $-1 < \eta^\gamma < 0.9$ and $5 < E_T^\gamma < 10$ GeV, and the initial energies are $E_e = 27.6$ GeV and $E_p = 920$ GeV. The final photon is isolated with parameters $\epsilon = 0.1$ and $R = 1$.

5.4.1 Comparison between exact and approximated results

In Figs. 5.1 and 5.2 the differential cross sections $d\sigma/dE_T^\gamma$ and $d\sigma/d\eta^\gamma$ are presented. The exact predictions ² (solid lines) are compared with the predictions obtained in the small cone approximation (dashed lines) and with the new H1 data [49] (see also [48]). The differences between both predictions are about 3%, so the small cone approximation works well, despite the fact that the isolation cone of radius $R = 1$ is not a small one.

The comparison between the two predictions are also presented in Tab. 3 for individual contributions and total cross sections. The Born, box and resolved photon contributions are the same in both calculations, since the approximation was applied to $\mathcal{O}(\alpha_S)$ corrections only (Sec. 4.2). Nevertheless the difference between exact and approximated $\mathcal{O}(\alpha_S)$ corrections is very large. We have found that for the isolated photon production the $\mathcal{O}(\alpha_S)$ corrections to the Born process obtained using the small cone approximation are 67% higher than the corresponding contribution obtained using the division of the phase space ³. We conclude that the small cone approximation gives a very rough estimation of the order of magnitude of the $\mathcal{O}(\alpha_S)$ corrections, however the total cross section is estimated quite well, since the $\mathcal{O}(\alpha_S)$ corrections give relatively small (5%) contribution to the total cross section (Tab. 3).

5.4.2 Comparison with the H1 data

The comparison with the new H1 Collaboration data [49] is presented in Figs. 5.1 and 5.2 and we see that the predictions tend to lie below the data for η^γ distribution, although in most bins an agreement is obtained within the large experimental errors (Fig. 5.2). For E_T^γ distribution (Fig. 5.1) the data in two bins are 2 - 3 standard deviations above the predictions, while in other bins the data and predictions agree well.

Our predictions shown in Figs. 5.1, 5.2 are obtained for the final photon and partons production (Eqs. 4.6, 4.7). According to the analysis done by the H1 Collaboration [49], for a realistic comparison with their data, the hadronization corrections and multiple interactions (h.c.+m.i.) should be taken into account in the predictions. Our exact predictions, after h.c.+m.i. corrections implemented by the H1 Collaboration [49], are shown in Fig. 5.3 (dotted lines) together with the H1 data [49] and with predictions of Fontannaz, Guillet and Heinrich (FGH) [29, 32]. Both, our and FGH, predictions are obtained with with MRST99^p [75], AFG ^{γ} [79], BFG^{*frag*} [83] parton densities. To show the effect of h.c.+m.i., the FGH predictions are presented with (solid lines) and without (dashed lines) these corrections ⁴.

The FGH and our predictions are below the data typically by 30% and 40%, respectively [49]. The discrepancy is seen in almost whole range of η^γ with exception

²By exact predictions we mean the predictions obtained using the technique described in Sec. 5.2 with no assumption that the isolation cone is small.

³For non-isolated photon there is no difference between both types of calculations.

⁴The correction factors are typically 0.75-0.90 depending on a bin. In both K&Z and FGH predictions the same factors are applied.

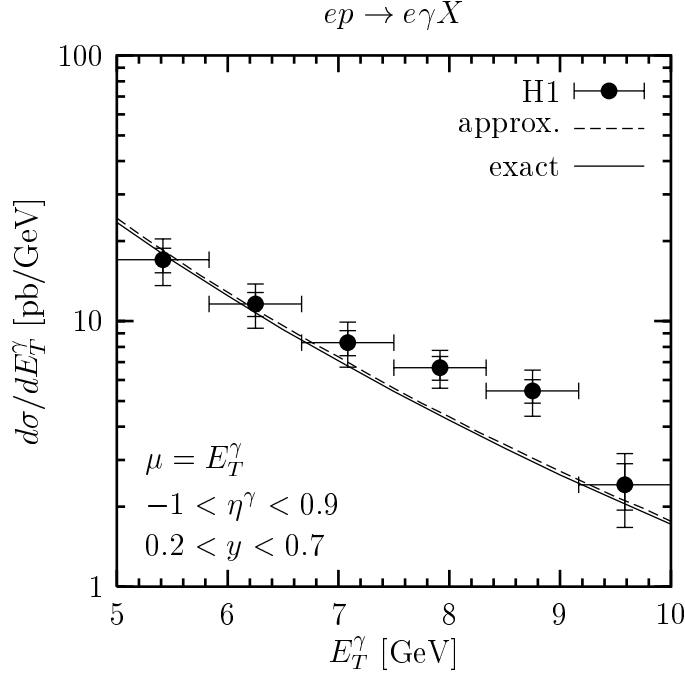


Figure 5.1: The comparison between exact predictions (solid line), predictions obtained in the small cone approximation (dashed line) and the H1 [49] data for $d\sigma/dE_T^\gamma$ cross section. The $GRV^{p,\gamma,frag}$ [71, 72, 73] parton densities are used

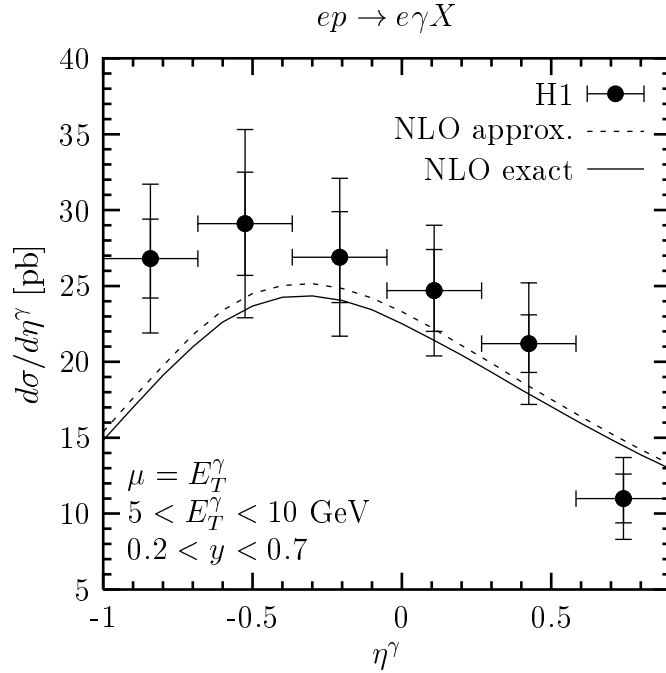


Figure 5.2: As in Fig. 5.1 for $d\sigma/d\eta_\gamma$ cross section.

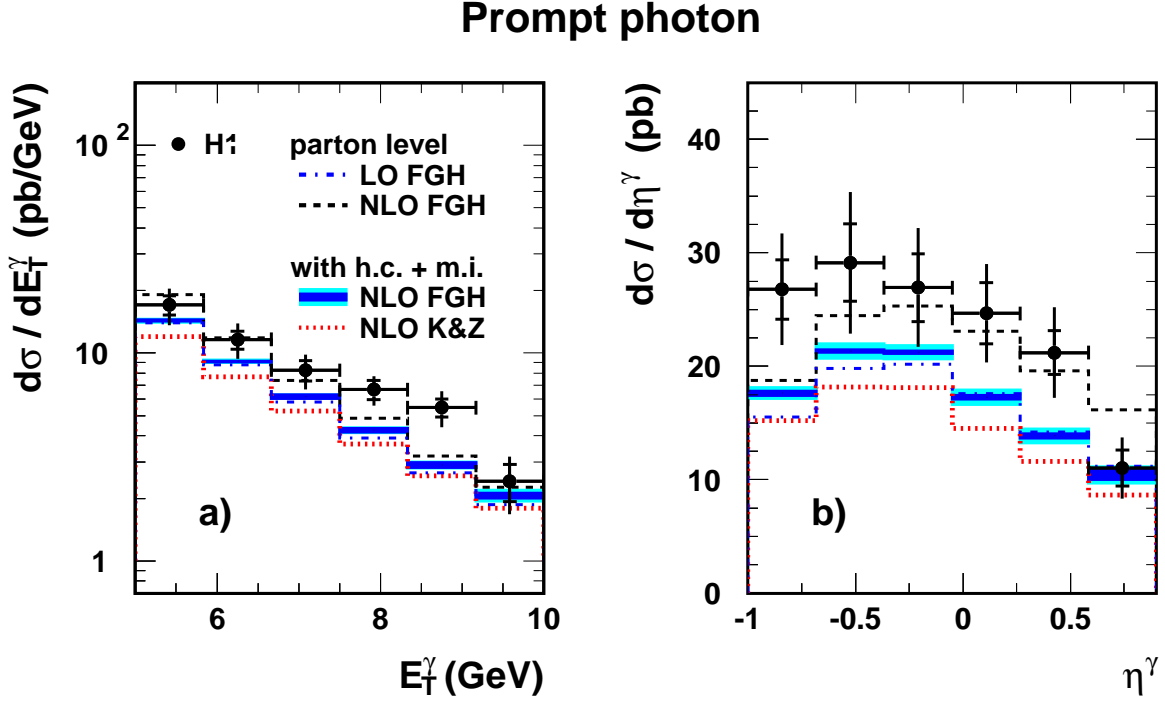


Figure 5.3: The cross sections $d\sigma/dE_T^\gamma$ (a) and $d\sigma/d\eta^\gamma$ (b) for the $ep \rightarrow e\gamma X$ process with $-1 < \eta^\gamma < 0.9$, $5 < E_T^\gamma < 10$ GeV and $0.2 < y < 0.7$. The H1 data [49] are compared with K&Z [33] (dotted lines) and FGH [29, 32] (solid lines) predictions obtained using MRST99^p [75], AFG ^{γ} [79], BFG ^{$frag$} [83] parton densities. Both predictions are corrected for hadronization and multiple interactions (h.c.+m.i.) effects. The shaded areas show changes of FGH predictions due to the μ scale variation between $0.5 \cdot E_T^\gamma$ and $2 \cdot E_T^\gamma$ (inner bands) and added linearly uncertainties on h.c.+m.i. corrections (outer bands). The LO (dashed-dotted) and NLO (dashed) FGH results without h.c.+m.i. are also shown. The figure is taken from the H1 paper [49]

of the last bin, where the QCD calculations and data are in agreement. Note, that the prompt photon cross sections measured previously by the ZEUS Collaboration [42] were well described by predictions at $\eta^\gamma > 0.1$ (Sec. 4.4.4). On the other hand, both the ZEUS [42] and the H1 [49] data are consistent, as it was shown in [49, 48]. It seems, that the above different conclusions of comparisons between the predictions and the ZEUS data, and between the predictions and the H1 data are due to large effects of h.c.+m.i. corrections applied in the H1 analysis [49].

Note, that the dependence on the choice of parton parametrizations is relatively large: results obtained using GRV ^{$p,\gamma,frag$} [71, 72, 73] (not shown) are 10% higher on average than these obtained with MRST99^p [75], AFG ^{γ} [79], BFG ^{$frag$} [83] densities, and slightly decrease the size of discrepancies between the predictions and the data.

5.4.3 Comparison with other QCD predictions (FGH)

The calculation of Fontannaz, Guillet and Heinrich (FGH) [29, 32] for the photoproduction of isolated photons at the HERA collider includes the $\mathcal{O}(\alpha_S)$ corrections to the processes with the resolved initial photon or/and with the fragmentation into the final photon, which are not included in our calculation (Chapter 2). Both our and FGH calculations take into account the $\mathcal{O}(\alpha^2\alpha_S^2)$ box diagram (Fig. 2.11) and all other diagrams shown in Figs. 2.1-2.4 and 2.7-2.11.

The predictions of FGH presented in their papers [29, 32] were obtained in the kinematic ranges considered by the ZEUS Collaboration [42, 44] (see Sec. 4.4.5) and one can not use them for the direct comparison with our predictions corresponding to the H1 measurements [49]. So, to compare the predictions, we use the FGH and K&Z (Zembrzuski and Krawczyk) [33] results based on the theoretical predictions and corrected for h.c.+m.i., as presented in the paper of the H1 Collaboration [49]⁵. Both predictions are obtained using the same parton parametrizations, namely MRST99^p [75], AFG ^{γ} [79], BFG^{*frag*} [83].

The FGH predictions are 15-20% larger than ours for the η^γ and E_T^γ distributions shown in Fig. 5.3. and this difference is of a similar order as the difference between our predictions and the predictions of Gordon (LG) [31] which was discussed in Sec. 4.4.5. It means, that the higher order terms included in the LG and FGH calculations and not included in the K&Z approach, give a sizable contribution to the cross section in the kinematic range considered for the prompt photon photoproduction. This is not fully supported by our study of the dependence on the renormalization/factorization scale, which seemed to suggest smaller effect due to missing higher order terms (Sec. 4.4.3).

⁵The applied correction factors are the same for both K&Z and FGH predictions, see footnote ⁴. So the relative differences between both “corrected” predictions are the same as the differences between pure QCD (with no h.c.+m.i.) K&Z and FGH predictions

Chapter 6

Isolated photon plus jet production

The partons produced in hard processes (Figs. 2.1-2.4, 2.7-2.11) are not observed experimentally, since they recombine into colorless jets. In previous parts of the work, the predictions for the prompt photon production were discussed and the presented cross sections were integrated over partons/jets momenta. Now, the isolated photon plus jet production is studied for limited ranges of both photon and jet rapidities and transverse energies. Such a process with two objects observed in the final state can be a source of more detailed information concerning the dynamics of the interaction.

6.1 Jet algorithm

As it was discussed in Chapter 2 and in Sec. 4.2, in the calculation we deal with $2 \rightarrow 2$ and $2 \rightarrow 3$ hard processes. In $2 \rightarrow 2$ processes (4.6) the jet originates from the parton d and the momentum of the jet can be identified with the momentum of this parton.

Two partons, d_1 and d_2 , produced in $2 \rightarrow 3$ processes (4.7) may lead to two separate jets or they may form one jet. The number of observed jets and their momenta depend on the jet definition. In this work the inclusive k_T -jet finding algorithm [108, 109] is applied in accordance with the jet definition used in the H1 Collaboration measurements [49].

Since in the presented calculation there are no more than two partons forming the jet or jets, the algorithm becomes very simple. If the distance between the partons, R_{12} , defined as

$$R_{12} = \sqrt{(\eta^{d_1} - \eta^{d_2})^2 + (\phi^{d_1} - \phi^{d_2})^2}, \quad (6.1)$$

is larger than an arbitrary parameter R_J , then two separate jets arise with transverse energies, rapidities, and azimuthal angles of the d_i -partons:

$$E_T^{jet_i} = E_T^{d_i}, \quad \eta^{jet_i} = \eta^{d_i}, \quad \phi^{jet_i} = \phi^{d_i}, \quad i = 1, 2. \quad (6.2)$$

For $R_{12} < R_J$ both partons are treated as components of one jet with

$$E_T^{jet} = E_T^{d_1} + E_T^{d_2}, \quad (6.3)$$

$$\eta^{jet} = (E_T^{d1} \eta^{d1} + E_T^{d2} \eta^{d2}) / E_T^{jet}, \quad (6.4)$$

$$\phi^{jet} = (E_T^{d1} \phi^{d1} + E_T^{d2} \phi^{d2}) / E_T^{jet}. \quad (6.5)$$

The algorithm can be easily applied in numerical calculations using the phase space slicing (Sec. 5.2). In the first part of the phase space, where $w \sim 1$, the kinematics is the same as in $2 \rightarrow 2$ processes. In part 2 (3, 4) one parton moves parallel to the initial electron (initial proton, final photon) and it, for sufficiently small θ_{cut} (θ_{cut} , R_{cut}), does not enter the cone defining the jet, so the jet consists (on the partonic level) of the second parton alone. In part 5 one or two jets may arise depending on the value of R_{12} (6.1).

Following experimental analyses [49], $R_J = 1$ is used in our numerical calculations.

6.2 Numerical results and discussion

We perform numerical calculations in kinematic regions as used in experimental analysis. There are two publications of the ZEUS Collaboration presenting results of measurements of the isolated photon plus jet photoproduction at the HERA collider [40, 44]. In the first paper [40] the cross section integrated over some kinematic range is given. The aim of the second one [44] was to study transverse momentum of partons in the proton, and no results for cross sections were presented (distributions of events, not corrected for the detector effects, were shown). There is also a conference paper of the ZEUS Collaboration where data for a differential cross section for the isolated photon plus a jet photoproduction are given, however these data are still preliminary [41].

In the new paper of the H1 Collaboration [49] (see also [48]), the photoproduction data for the isolated final photon ($\epsilon = 0.1$ and $R = 1$) with the initial energies $E_e = 27.6$ GeV and $E_p = 920$ GeV are presented for various differential cross sections of both $ep \rightarrow e\gamma X$ (considered in Chapter 5) and $ep \rightarrow e\gamma jet X$ processes. Herein, the predictions for the kinematic limits as in [49] are compared with these recent final data. The cross sections are integrated over $0.2 < y < 0.7$, and $-1 < \eta^\gamma < 0.9$ and/or $5 < E_T^\gamma < 10$ GeV with the jet rapidity and jet transverse energy in the range $-1 < \eta^{jet} < 2.3$ and $4.5 \text{ GeV} < E_T^{jet}$, respectively. If two jets are found within the above region, that with higher E_T^{jet} is taken. Other parameters are specified in Sec. 2.2.

6.2.1 Asymmetric cuts

As it is discussed in [32], the symmetric cuts for the photon and the jet transverse energy, $E_{T,min}^{jet} = E_{T,min}^\gamma$, lead to unphysical results in next-to-leading or higher orders of calculations due to constraints imposed on soft gluons (see also [110, 111, 112]). We have decided to study this effect for the cross section as a function the photon transverse energy, not analyzed in [32]. This allows to understand the effect of the symmetric cuts in more details. The results of this study was first presented in our

paper [33]. Next, similar study of the effect of the symmetric cuts was presented in [34].

Our findings are illustrated in Fig. 6.1a,b. We study the dependence of the NLO predictions on the photon transverse energy in the E_T^γ -range wider than the range considered by the H1 Collaboration. At E_T^γ values close to the minimal jet transverse energy, $E_{T,min}^{jet} = 4.5$ GeV, the NLO differential cross section has a discontinuity, see Fig. 6.1a. For $(E_T^\gamma)_- \rightarrow 4.5$ GeV the cross section has a strong maximum while a minimum for $(E_T^\gamma)_+ \rightarrow 4.5$ GeV. In the minimum the value of the cross section is even negative. This unphysical fluctuation is due to processes with soft gluons: large terms corresponding to the soft gluon emission and the virtual gluon exchange do not cancel properly if the photon transverse energy is close to the minimal transverse energy of the jet, because some of this terms corresponds to E_T^γ slightly below the cut-off $E_{T,min}^{jet}$ and the other correspond to E_T^γ slightly above $E_{T,min}^{jet}$.

However, if we integrate the cross section over some E_T^γ -bins then this fluctuation disappears. As it is shown in Fig. 6.1b, the NLO predictions are well defined if one takes the cross section integrated over E_T^γ from $E_{T,min}^{jet} - \Delta$ to $E_{T,min}^{jet} + \Delta$, provided that Δ is sufficiently large in the comparison with the gap in Fig. 6.1a, say $\Delta > 0.3$ GeV. So, the bins of a length 1 GeV presented in Fig. 6.1b are large enough to avoid errors corresponding to the fluctuation around $E_T^\gamma = E_{T,min}^{jet}$.

An integration of the differential cross section (Fig. 6.1a) over the photon transverse energy higher than the minimal jet transverse energy, $E_T^\gamma \geq E_{T,min}^{jet}$ (symmetric cuts), leads to underestimated predictions in NLO. However numerically this effect is not very important, being at level of roughly 5% if the integration is performed in the range from $E_T^\gamma = E_{T,min}^{jet} = 4.5$ GeV to $E_T^\gamma = 10$ GeV.

Note that in the previous measurements [40, 41, 44] the symmetric cuts $E_T^\gamma > 5$ GeV and $E_T^{jet} > 5$ GeV were used, while in the new H1 analysis [49] the asymmetric cuts $E_T^\gamma > 5$ GeV and $E_T^{jet} > 4.5$ are taken. This latter choice of cuts allows to avoid the theoretical errors in QCD calculations and is applied in calculations presented in next sections (Sec. 6.2.2-6.2.4).

It is worth mentioning that the cross section for $E_T^\gamma < E_{T,min}^{jet}$ (Fig. 6.1a) is dominated by the contribution due to the $2 \rightarrow 3$ processes in the $\mathcal{O}(\alpha_S)$ corrections (Figs. 2.3, 2.4), since the contributions of the $2 \rightarrow 2$ processes (Figs. 2.1, 2.7-2.11) are suppressed by the requirement $E_T^{jet} > E_{T,min}^{jet}$ and by the isolation. For $E_T^\gamma < E_{T,min}^{jet}/(1 + \epsilon) \approx 4$ GeV the $2 \rightarrow 2$ processes do not contribute at all. On the other hand, for larger E_T^{jet} , say $E_T^{jet} > 5$ GeV, the contribution of $\mathcal{O}(\alpha_S)$ corrections is very small, see Tab. 1.

6.2.2 Theoretical uncertainties

μ

The dependence of the considered cross sections on the choice of the renormalization/factorization scale, μ , is not strong: variations of μ from E_T^γ to $E_T^\gamma/2$ or $2E_T^\gamma$ lead to changes of the cross section less than 3% for $E_T^\gamma < E_{T,min}^{jet}$ and up to 5% for $E_T^\gamma > E_{T,min}^{jet}$.

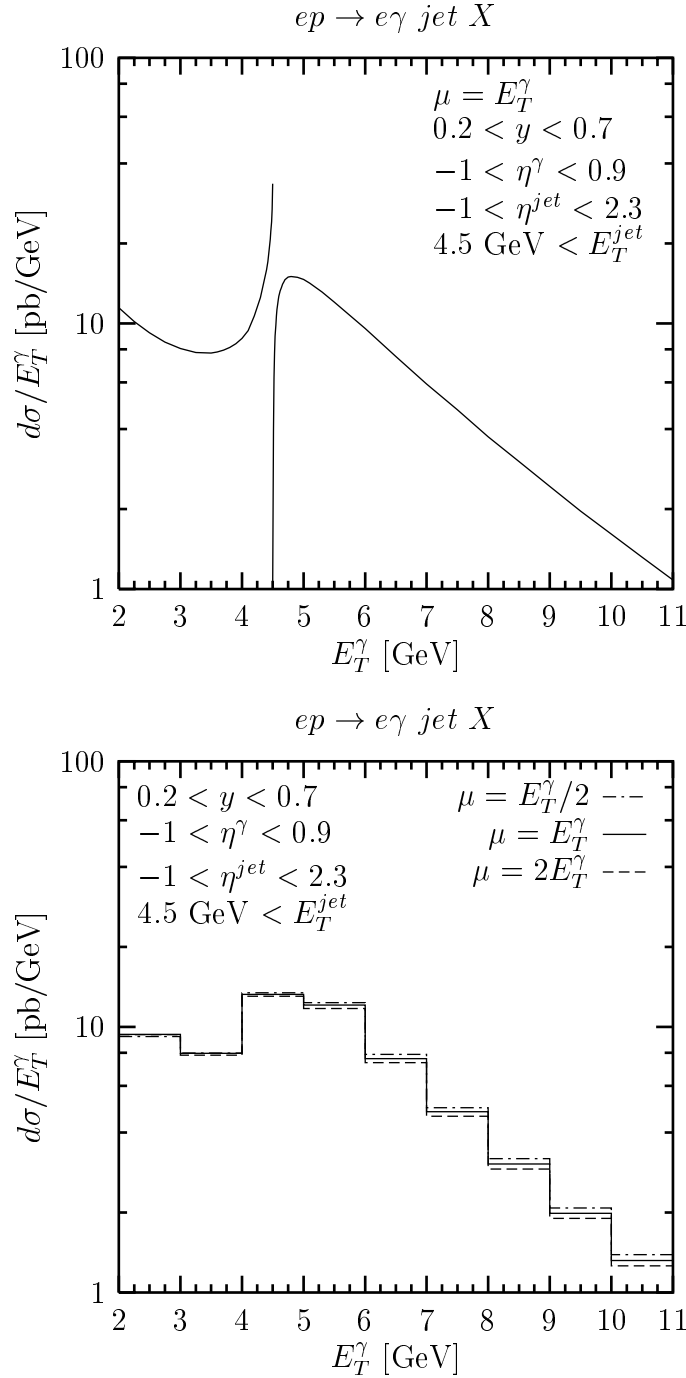


Figure 6.1: The differential cross section $d\sigma/dE_T^\gamma$ (a) and the differential cross section $d\sigma/dE_T^\gamma$ averaged over E_T^γ -bins (b) for the $ep \rightarrow e\gamma \text{ jet } X$ process. The NLO predictions for $E_T^\gamma = \mu$ (a) and for μ between $E_T^\gamma/2$ and $2E_T^\gamma$ (b) are shown.

(Fig. 6.1b). The predictions for various μ are also shown in Fig. 6.2. In each presented here bin the dependence on the choice of μ is less than $\pm 5\%$ for both E_T^{jet} (Fig. 6.2a) and η_{jet} (Fig. 6.2b) distributions. The total cross section integrated over the kinematic range considered by the H1 Collaboration [49] vary by $\pm 3.4\%$. Since the effect of the

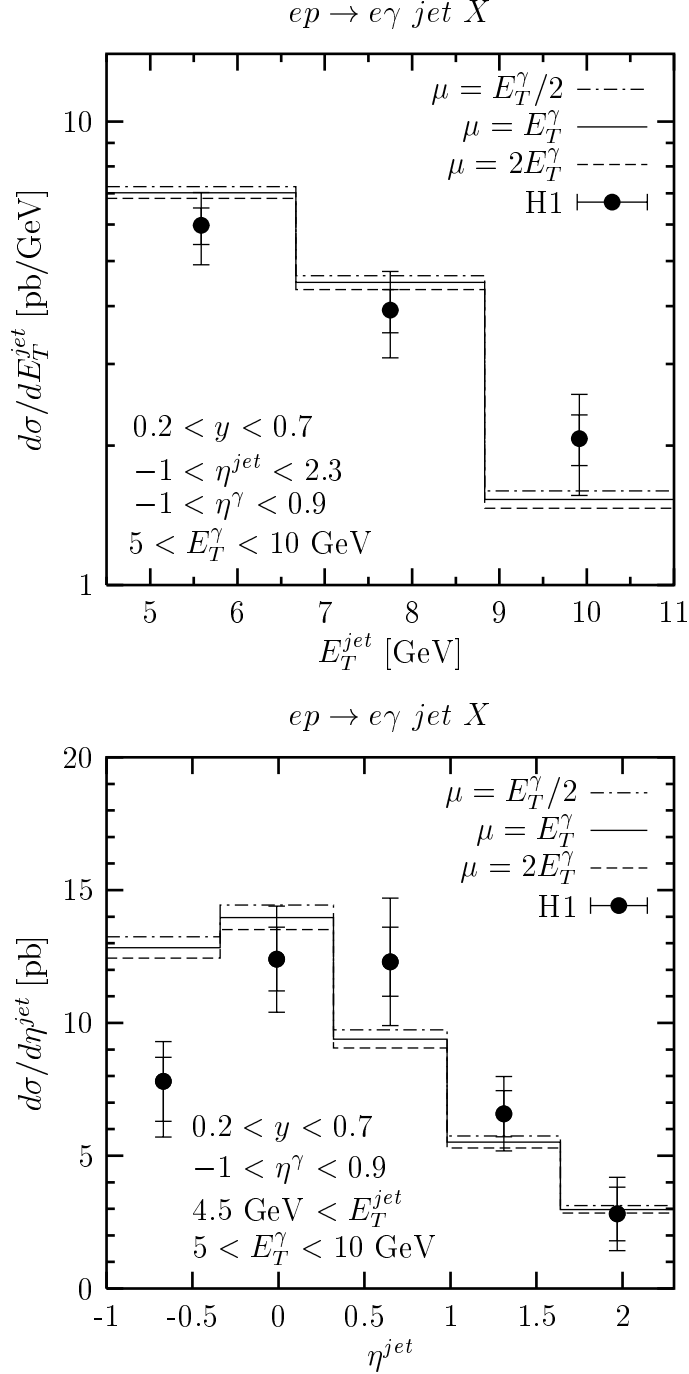


Figure 6.2: The cross section $d\sigma/dE_T^{jet}$ (a) and $d\sigma/d\eta^{jet}$ (b) for $\mu = 0.5 \cdot E_T^\gamma$ (dashed-dotted lines), $\mu = E_T^\gamma$ (solid lines) and $\mu = 2 \cdot E_T^\gamma$ (dashed lines). The H1 Collaboration data [49] are shown for comparison.

variation of the μ scale is not large, the calculation seems to be stable, and one can expect that the contributions of higher orders are not sizable.

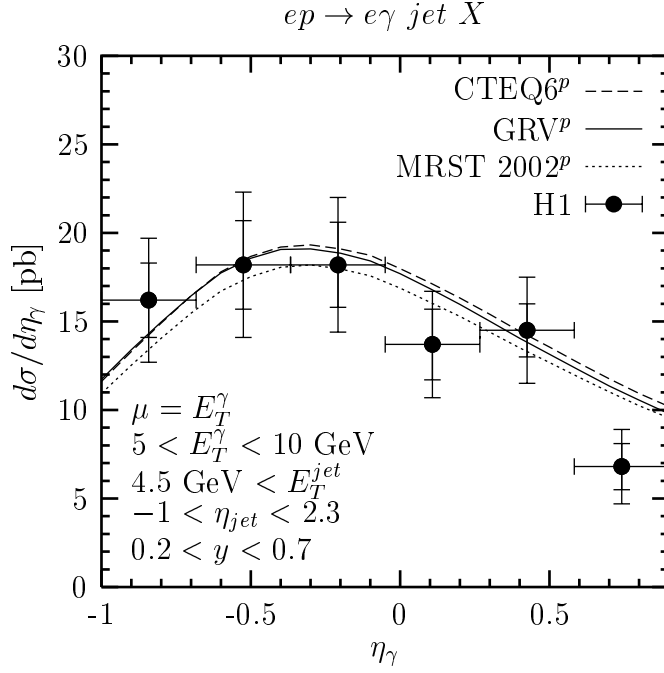


Figure 6.3: The cross section $d\sigma/d\eta_\gamma$ for MRST2002^p (NLO) [76] (dotted line), GRV^p (NLO) [71] (solid line) and CTEQ6^p (NLO) [78] (dashed line) parton densities in the proton used with GRV^{γ,frag} (NLO) [72, 73] densities in the photon and fragmentation functions. The H1 Collaboration data [49] are also shown.

f_p

Next, we have checked the sensitivity to the choice of parametrizations. In Fig. 6.3 the results obtained using different parton densities in the proton are shown. The predictions of CTEQ6^p (NLO) [78] are 6% higher than the predictions of MRST2002^p (NLO) [76]. The GRV^p (NLO) [71] densities give results higher than MRST2002^p by 5-7% at negative η_γ , and 3-5% at positive η_γ . Differences between CTEQ6^p and GRV^p do not exceed 4%.

f_γ

The most important variables for testing the structure of colliding particles are the fractional momenta of partons in these particles. Below we consider the distribution of the fractional momentum in the photon, however since the theoretical variable x_γ is not a good observable, in experimental analyses some estimations of x_γ are used instead. We consider here the observable x_γ^{obs} , which is defined as [40, 47]¹:

$$x_\gamma^{obs} = (E_T^{jet} e^{-\eta^{jet}} + E_T^\gamma e^{-\eta^\gamma}) / 2yE_e. \quad (6.6)$$

¹The variable x_γ^{obs} is equal to the “theoretical” one, x_γ , for $2 \rightarrow 2$ processes with the direct final photon. For the processes with a larger number of partons in the final state and for the processes with the parton-to-photon fragmentation, the x_γ and x_γ^{obs} differ.

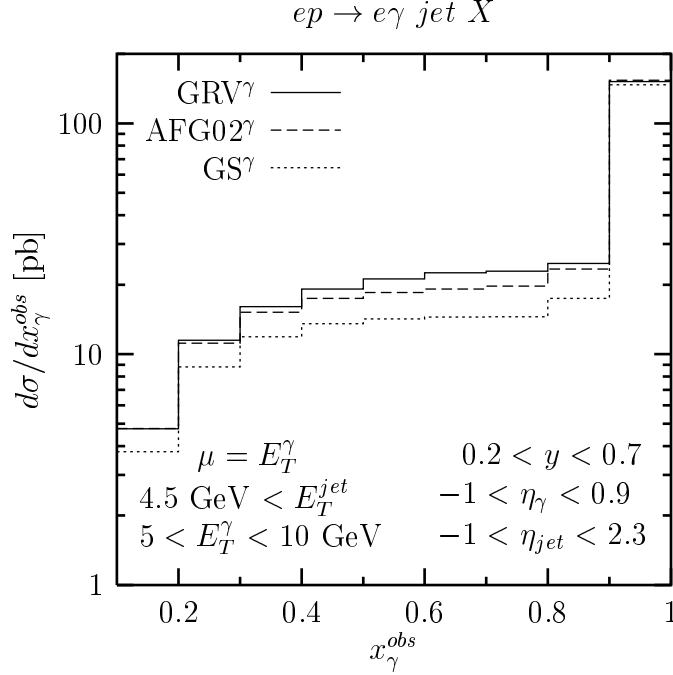


Figure 6.4: The cross section $d\sigma/dx_\gamma^{obs}$ for GRV^γ (NLO) [72] (solid line), $AFG02^\gamma$ (NLO) [80] (dashed line) and GS^γ [81] (dotted line) parton densities in the photon used with $GRV^{p,frag}$ (NLO) [71, 73] densities in the proton and fragmentation functions.

In Fig. 6.4 the x_γ^{obs} distributions are shown for different parton densities in the photon. The GS^γ (NLO) parametrization [81] give predictions lower than GRV^γ (NLO) [72] by 20-36% for $x_\gamma^{obs} < 0.9$. This large difference is due to the specific treatment of the charm contribution in the GS parametrization (see Sec. 4.4.4). The results obtained with use of AFG^γ (NLO) [79] and $AFG02^\gamma$ (NLO) [80] are very similar, and only the latter is shown in Fig. 6.4. It gives predictions up to 15% lower than GRV^γ for $x_\gamma^{obs} < 0.9$. At large- x_γ^{obs} region, $x_\gamma^{obs} > 0.9$, the cross section is dominated by the contribution of processes with the direct initial photons, and the differences between predictions obtained using various parametrizations are small. For the total cross section integrated over all x_γ^{obs} , within the considered range of y , η^γ , E_T^γ , η^{jet} and E_T^{jet} , the difference between results based on GRV^γ and $AFG02^\gamma$ ($G^\gamma S$) is 4% (16%).

Note, that there are new LO [82, 113, 114] and NLO [115] parametrizations of the real photon structure with a special treatment of heavy quark contributions. For the first time for the photon they use the $ACOT_\chi$ scheme introduced previously for the proton [116] and include the newest F_2^γ data, never used in constructing other parametrizations for the photon. We have compared the results obtained using the LO parametrization of Cornet, Jankowski, Krawczyk and Lorca ($CJKL^\gamma$) [82] with results obtained using $GRV^\gamma(LO)$ [72]. Despite the fact that parton densities in both parametrizations differ considerably, they lead to similar results for the prompt photon production at HERA. Predictions for $CJKL^\gamma(LO)$ are about 3% lower than the predictions for $GRV^\gamma(LO)$ (in this comparison the $\mathcal{O}(\alpha_S)$ corrections were not taken into account and the $GRV^p(LO)$ [71] densities in the proton were used).

D_γ

We have also compared predictions of DO^{frag} (LO) [15], GRV^{frag} (NLO) [73] and BFG^{frag} (NLO) [83] fragmentation functions. The isolation requirement reduces the contribution of processes involving the resolved final photon (Sec. 4.4.1, Tabs. 1, 2), so the dependence on the choice of fragmentation functions is weak, even if the fragmentation functions differ considerably from one another. The total cross sections for the isolated photon plus jet production obtained with DO^{frag} and BFG^{frag} (set I and set II) are lower than the predictions of GRV^{frag} by 2% and 4%, respectively.

f_p, f_γ, D_γ

The GRV distributions for the proton [71], photon [72] and fragmentation [73] have been used as a reference in calculations discussed above, and while performing the comparison each time only one parametrization has been changed. The differences observed in the total cross section (i.e. in the cross section integrated within the considered kinematic range) are not large (with an exception of the GS densities, which give predictions considerably lower than the other densities in the photon, as we discussed before). However, the differences can be larger if one changes simultaneously all the used distributions. For instance predictions of the MRST1999^p [75], AFG^γ [79] and BFG^{frag} [83] set ² are lower than the $\text{GRV}^{p,\gamma,frag}$ predictions by 10% on average. The comparison between both results is presented in Fig. 6.5. The differences are large, up to 13%, for $E_T^\gamma \lesssim 7.5$ GeV, while for higher E_T^γ both sets of parton densities give predictions relatively close to each other and differences are below 6%.

N_f

In the calculation the renormalization/factorization scale $\mu = E_T^\gamma$ is used for E_T^γ between 5 and 10 GeV (with exception of Fig. 6.1, where a wider range of E_T^γ is shown). It is a standard assumption that the number of active massless flavours at this scale is $N_f = 4$ [27]-[34]. For a comparison, in Fig. 6.6 the results obtained with $N_f = 3$ and $N_f = 5$ are also shown. The contribution of the bottom quark is very small and the results for $N_f = 4$ and $N_f = 5$ are similar. Differences between these two results are much smaller than the standard deviations of the H1 data [49] which are also presented in Fig. 6.6. On the other hand, the contribution of the charm quark is large: the results obtained using $N_f = 3$ are about 35% below the predictions for $N_f = 4$. Neglecting of the charm mass may lead to a slight overestimation of the production rate, especially in the box contribution which is particularly sensitive to the change from $N_f = 3$ to $N_f = 4$. However we do not expect that an improved treatment of the charm contribution would change our results qualitatively, since the energy $\mu = E_T^\gamma \geq 5$ GeV is several times larger than the charm mass.

²These parametrizations are used for comparison with the H1 data and with the FGH predictions in Secs. 5.4.2, 5.4.3, 6.2.3 and 6.2.4.

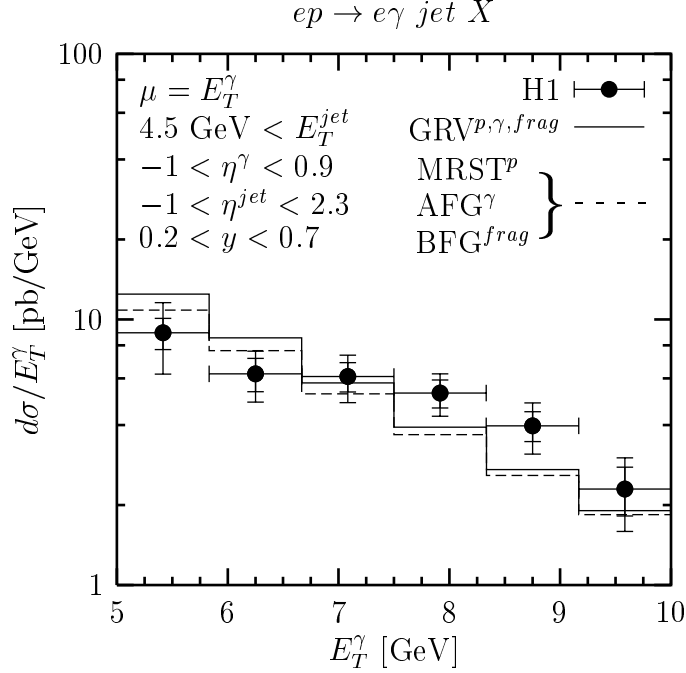


Figure 6.5: The cross section $d\sigma/dE_T^\gamma$ averaged over bins corresponding to the H1 Collaboration data [49]. The predictions are obtained using $GRV^{p,\gamma,frag}$ [71, 72, 73] (solid line) and $MRST1999^p$ [75], AFG^γ [79], BFG^{frag} [83] (dashed line) parton densities.

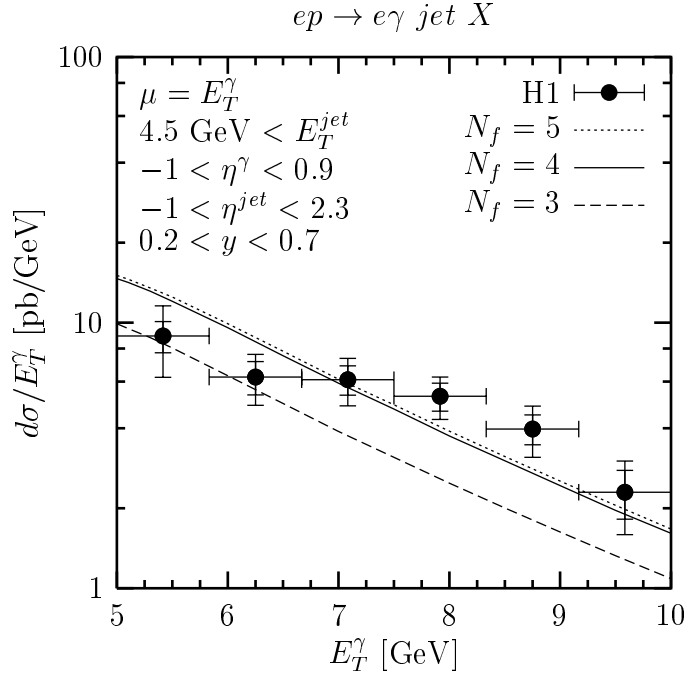


Figure 6.6: The cross section $d\sigma/dE_T^\gamma$ obtained with $GRV^{p,\gamma,frag}$ [71, 72, 73] parametrizations for $N_f = 3$ (dashed line), 4 (solid line) and 5 (dotted line). The H1 Collaboration data [49] are shown.

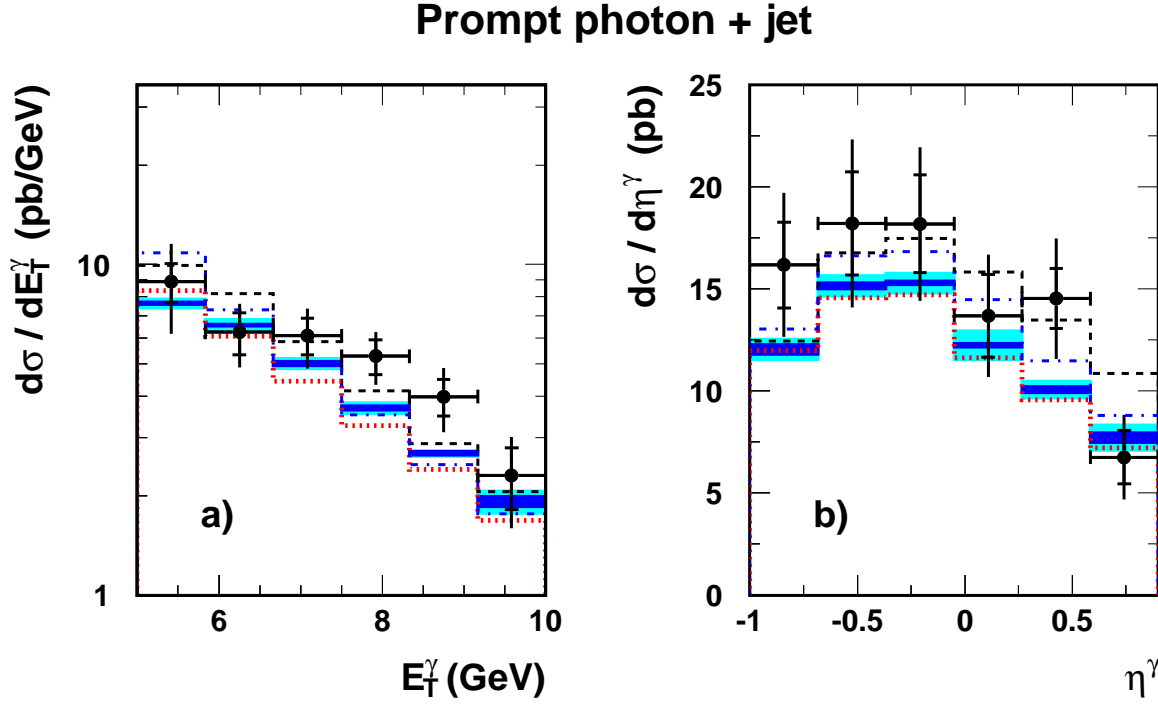


Figure 6.7: As in Fig. 5.3 for the $ep \rightarrow e\gamma \text{ jet } X$ process. The additional cuts for the jet are: $E_T^{\text{jet}} > 4.5 \text{ GeV}$ and $-1 < \eta^{\text{jet}} < 2.3$. The figure is taken from [49].

6.2.3 Comparison with the H1 data

The QCD results for the photon plus jet production shown in Figs. 6.2, 6.3, 6.5 and 6.6 are in reasonable agreement with the data of the H1 Collaboration [49] although some discrepancies are present, especially for $\eta_{\text{jet}} < -0.3$ (Fig. 6.2) and for the E_T^γ distribution (Figs. 6.5, 6.6).

However, according to [49], for the realistic comparison with the data, the pure perturbative QCD calculations should be corrected for effects of hadronization and multiple interactions (h.c.+m.i.), as discussed in Sec. 5.4.2. Such a comparison was performed by the H1 Collaboration [49], see Figs. 6.7 and 6.8, where the predictions of Zembruski and Krawczyk (K&Z) [33] (dotted lines) corrected for h.c.+m.i. are presented together with the H1 Collaboration data [49] and with predictions of Fontannaz, Guillet and Heinrich (FGH) [29, 32]. To show the size of the corrections, the FGH NLO results are plotted without (dashed lines) and with (solid lines) h.c.+m.i.³. Both K&Z and FGH predictions are obtained using the MRST1999^p [75], AFG^γ [79] and BFG^{frag} [83] parton parametrizations.

The K&Z and FGH calculations for the $ep \rightarrow e\gamma \text{ jet } X$ process give somewhat better description of the data than in the case of the $ep \rightarrow e\gamma X$ process (Sec. 5.4). The agreement is seen in most bins in Figs. 6.7 and 6.8, especially when one takes into account on the one hand the uncertainties of h.c.+m.i. corrections and on the other hand the theoretical uncertainties due to the variation of the μ scale ($\pm 5\%$) and

³See footnote ⁴ in Sec. 5.4.2.

Prompt photon + jet

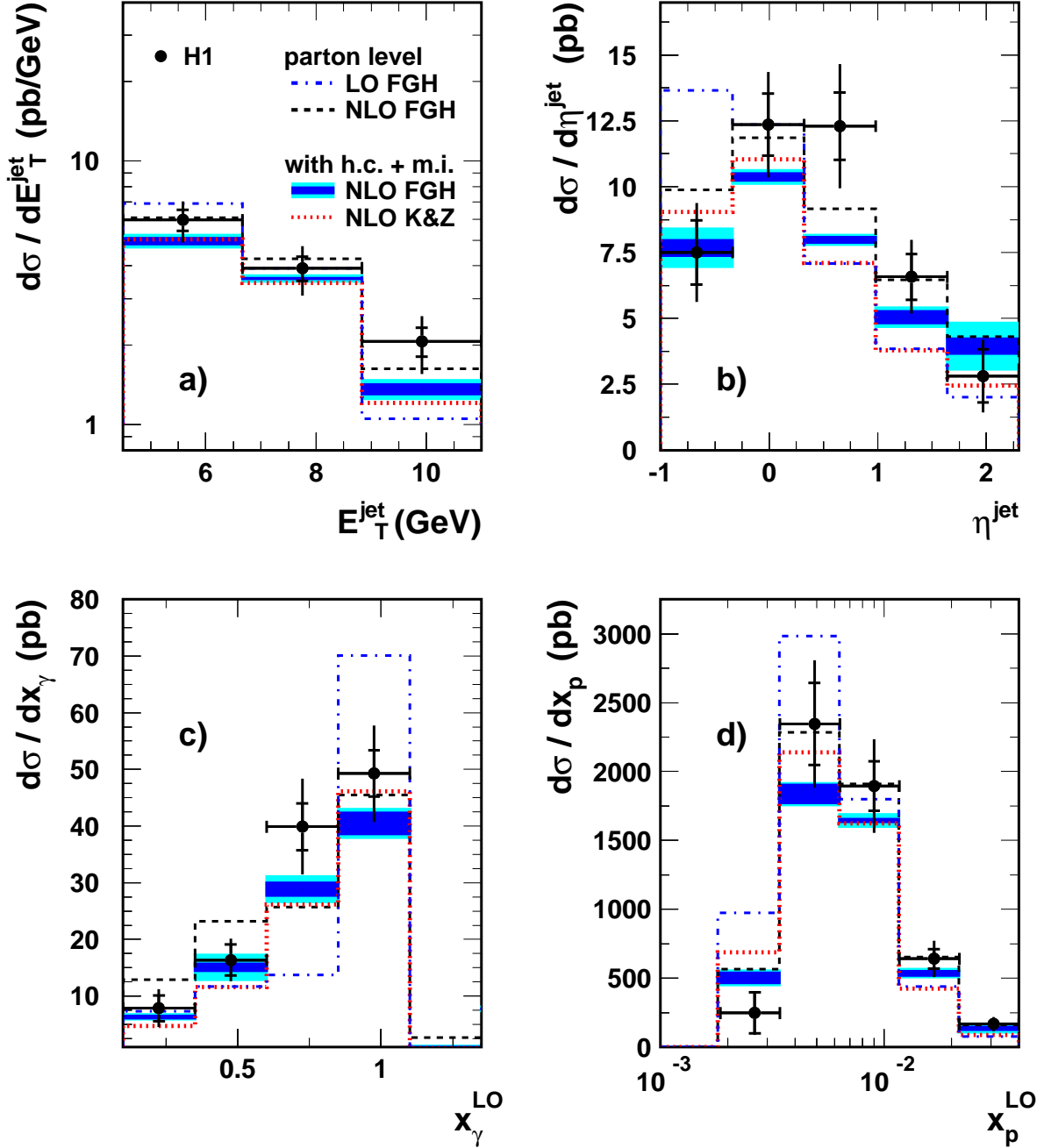


Figure 6.8: As in Fig. 6.7 for $d\sigma/dE_T^{\text{jet}}$ (a) $d\sigma/d\eta^{\text{jet}}$ (b) $d\sigma/dx_\gamma^{\text{LO}}$ (c) and $d\sigma/dx_p^{\text{LO}}$ (d) cross sections. The figure is taken from [49].

to the choice of parton densities ($\sim 10\%$) (Sec. 6.2.2). Nevertheless, the K&Z and FGH predictions tend to underestimate the H1 data. In some kinematic ranges the data are 1-2 standard deviations above the K&Z predictions e.g. for $6.7 < E_T^\gamma < 9.2$ GeV (Fig. 6.7a) and $0.3 < \eta_{\text{jet}} < 1.6$ (Fig. 6.8b).

In Figs. 6.8c,d the cross sections $d\sigma/dx_\gamma^{LO}$ and $d\sigma/dx_p^{LO}$ are shown, where x_γ^{LO} and x_p^{LO} are defined as follows [49]⁴:

$$x_\gamma^{LO} = E_T^\gamma(e^{-\eta^{jet}} + e^{-\eta^\gamma})/2yE_e, \quad (6.7)$$

$$x_p^{LO} = E_T^\gamma(e^{-\eta^{jet}} + e^{-\eta^\gamma})/2E_p. \quad (6.8)$$

The K&Z predictions are 1-1.5 standard deviations below the data for $x_\gamma^{LO} < 0.85$ (Fig. 6.8c). Note, that better agreement is obtained if GRV $^{p,\gamma,frag}$ [71, 72, 73] parametrizations are used (not shown in Fig. 6.8 which is taken from the H1 paper), since they give predictions 18% higher than MRST1999 p , AFG $^\gamma$ and BFG frag at $x_\gamma^{LO} < 0.85$ (at $x_\gamma^{LO} > 0.85$ the difference is 4%).

At $x_p^{LO} > 0.012$ ($x_p^{LO} < 0.0034$) the K&Z predictions are 2 standard deviations below (above) the data (Fig. 6.8d). An implementation of GRV $^{p,\gamma,frag}$ densities does not improve the description of the data (not shown).

The H1 Collaboration has also presented the cross sections $d\sigma/dp_\perp$ [49], where p_\perp is the component of the photon momentum perpendicular to the scattering plane (see [49] for the precise definition). For $p_\perp \neq 0$ the $2 \rightarrow 2$ processes give no contribution, so the cross section is sensitive to higher order processes only. For $x_\gamma^{LO} > 0.85$ the cross section is dominated by $\mathcal{O}(\alpha_S)$ corrections to the processes with direct initial and final photons, which are included in NLO in our calculation, and the data are in reasonable agreement with K&Z predictions. On the other hand, for $x_\gamma^{LO} < 0.85$ the cross section is dominated by $\mathcal{O}(\alpha_S)$ corrections to the processes with resolved photons. These contributions are not included in the K&Z calculation, so our predictions by definition can not describe such data.

6.2.4 Comparison with other QCD predictions (FGH)

The calculation of Fontannaz, Guillet and Heinrich (FGH) [29, 32] takes into account the $\mathcal{O}(\alpha_S)$ corrections to the resolved photon processes, which are not included in the calculation presented in this work (Chapter 2, Sec. 5.4.3). In the considered kinematic range for the photon plus jet production the total cross section of FGH is about 4% higher than our predictions, so the total contribution of $\mathcal{O}(\alpha_S)$ corrections to the resolved photon processes is relatively small.

The K&Z and FGH results shown in Fig. 6.7b differ by 5% or less in the whole range of η^γ . The differences are larger for other differential cross sections (Figs. 6.7a, 6.8). At $E_T^\gamma > 6.7$ GeV the FGH predictions are about 13% higher, while at $5 < E_T^\gamma < 5.8$ GeV they are 7% lower than predictions of K&Z (Fig. 6.7a). The largest differences are for $1 < \eta^{jet} < 1.6$ and $1.6 < \eta^{jet} < 2.3$, where the FGH predictions are above K&Z by 33% and 63%, respectively. Despite these divergences, both calculations lead to a similar description of the H1 data shown in Figs. 6.7 and 6.8.

⁴For $2 \rightarrow 2$ processes the experimental variables x_γ^{LO} and x_p^{LO} are equal to corresponding theoretical variables multiplied by z (defined in Sec. 3.1): $x_\gamma^{LO} = z \cdot x_\gamma$, $x_p^{LO} = z \cdot x_p$.

Note that the FGH predictions are closer to the H1 data than the K&Z predictions for $d\sigma/dp_\perp$ with $x_\gamma^{LO} < 0.85$ [49], since we do not include processes which contribute in this region (Sec. 6.2.3).

Chapter 7

Probing the gluon content of the photon

The photoproduction processes in the electron-proton scattering are sensitive to the parton densities in the proton as well as in the photon and provide an opportunity to probe the photon structure at the HERA collider (for a review of the data see [3]). Also the photoproduction of photons with a large transverse momentum (the Deep Inelastic Compton process) was considered as a possible tool to test the quark and gluon densities in the photon and proton [20]-[24], [26]-[33], [92, 93]. In particular, it was found that the contribution involving the gluon density in the photon is especially large when the final photon is produced in the forward (proton) direction [20]-[24], [92, 93]. Recently new analysis devoted to the possibility of measuring the gluon density in the photon and proton in the $ep \rightarrow e\gamma \text{ jet } X$ process at HERA were presented in [34, 35, 36].

So far we have considered the production of the photon with the large transverse momentum (transverse energy) in the electron-proton scattering where the mediating photons have been quasi-real, $Q^2 \approx 0$, and they spectrum have been given by the equivalent photon approximation [86]-[89] (Sec. 2.3). Now, we extend the study including the effect of small, but non-zero virtuality, $Q^2 \neq 0$.

The first attempt to describe the Deep Inelastic Compton process at HERA using the parton densities in the virtual photon can be found in [117, 118], where we tested in LO the validity of the equivalent photon approximation. Next, we have examined the usefulness of this process to study at the HERA collider the structure of a virtual photon, and in particular its gluonic content [92, 93]. In this chapter we discuss shortly some of our LO results obtained in [92, 93].

7.1 Calculation of the cross section

The invariant differential cross section for the deep inelastic electron-proton scattering can be written in the following form:

$$E'_e \frac{d\sigma^{ep \rightarrow eX}}{d^3p'_e} = \Gamma \left(\sigma_T^{\gamma^* p \rightarrow X} + \epsilon \sigma_L^{\gamma^* p \rightarrow X} \right), \quad (7.1)$$

where $\sigma_T^{\gamma^* p \rightarrow X}$ ($\sigma_L^{\gamma^* p \rightarrow X}$) is the cross section for the interaction between the proton and the virtual photon polarized transversely (longitudinally) and p'_e (E'_e) stands for the final electron momentum (energy). Coefficients Γ and $\epsilon\Gamma$ are functions of energies and momenta of the electron in initial and final states, see [9]. They can be interpreted as the probability of emitting by the initial electron the virtual photon polarized transversely and longitudinally. If so, we can use (7.1) to obtain the differential cross section for the $ep \rightarrow e\gamma X$ process taking into account the virtuality of the exchanged photon:

$$E'_e \frac{d}{d^3p'_e} E_\gamma \frac{d\sigma^{ep \rightarrow e\gamma X}}{d^3p_\gamma} = \Gamma \left(E_\gamma \frac{d\sigma_T^{\gamma^* p \rightarrow \gamma X}}{d^3p_\gamma} + \epsilon E_\gamma \frac{d\sigma_L^{\gamma^* p \rightarrow \gamma X}}{d^3p_\gamma} \right), \quad (7.2)$$

where p_γ (E_γ) stands for the final photon momentum (energy). Since the cross section for the reaction $ep \rightarrow e\gamma X$ is dominated by the exchange of photons with small virtuality, one can neglect a contribution due to the longitudinal polarization [5]. Assuming that the exchanged photon has only the transverse polarization we obtain:

$$E_\gamma \frac{d\sigma^{ep \rightarrow e\gamma X}}{d^3p_\gamma} = \int \frac{d^3p'_e}{E'_e} \Gamma E_\gamma \frac{d\sigma^{\gamma^* p \rightarrow \gamma X}}{d^3p_\gamma}. \quad (7.3)$$

Our aim is to study the sensitivity of the cross section to the gluon distribution in the photon. To achieve this goal we include the Born process (Fig. 2.1) and the processes with the resolved initial photon (Fig. 2.7), and we omit contributions of other processes:

$$E_\gamma \frac{d\sigma^{\gamma^* p \rightarrow \gamma X}}{d^3p_\gamma} = \sum_{q, \bar{q}} \int_0^1 dx f_{q/p}(x, \mu^2) E_\gamma \frac{d\sigma^{\gamma^* q \rightarrow \gamma q}}{d^3p_\gamma} + \quad (7.4)$$

$$\sum_{a=q, \bar{q}, g} \int_0^1 dx_\gamma \sum_{b=q, \bar{q}, g} \int_0^1 dx f_{a/\gamma^*}(x_\gamma, \mu^2, Q^2) f_{b/p}(x, \mu^2) E_\gamma \frac{d\sigma^{ab \rightarrow \gamma d}}{d^3p_\gamma}, \quad (7.5)$$

where $f_{b/p}$ and f_{a/γ^*} are the parton densities in the proton and in the virtual photon. In the partonic cross section $d\sigma^{\gamma^* q \rightarrow \gamma q}$ as well as in the partonic distribution f_{a/γ^*} we take the virtuality Q^2 of the photon emitted by the electron exactly as it follows from the kinematics of the process.

7.2 Numerical results

In the calculation we use the GRS (LO) [84] and the GRV (LO) [71] parton distributions in the virtual photon and in the proton, respectively. The number of flavours is assumed $N_f = 3$ - the maximum number of active massless quarks in the GRS parametrization. We take the QCD parameter $\Lambda_{QCD} = 0.2$ GeV and the hard scale equal to the transverse energy of the final photon, $\mu = E_T^\gamma$. Calculations are performed for the initial electron and proton energies in the HERA accelerator: $E_e = 30$ GeV² and $E_p = 820$ GeV² with the virtualities of the mediating photon, Q^2 ranging from 10^{-7} GeV² to 2.5 GeV². Note that due to a smooth behaviour of the GRS parametrization in the limit $Q^2 \rightarrow 0$ we were able to perform the calculation also for Q^2 below Λ_{QCD}^2 .

We study the differential cross section

$$E_\gamma \frac{d\sigma^{ep \rightarrow e\gamma X}}{d^3p_\gamma dQ^2 dy}, \quad (7.6)$$

for the transverse energy of the final photon $E_T^\gamma = 5$ GeV and the energy of the mediating photon $E_{\gamma^*} = yE_e$ with fixed $y = 0.5$.

As it was expected, the cross section decreases for increasing values of the virtuality Q^2 . For example the predictions obtained for $Q^2 = 0.25$ GeV² (2.5 GeV²) are one order (three orders) of magnitude lower than the predictions for $Q^2 = 0.03$ GeV² [92].

The processes initiated by the gluonic content of the virtual photon dominate in the cross section in the forward (proton) direction, i.e. for large photon rapidities, η_γ [92, 93]. This effect is presented in Fig. 7.1, where the contributions due to the resolved virtual photon divided by the Born contribution are shown as a functions of η_γ . The results for the process $g_{\gamma^*} q_p \rightarrow \gamma q$ are obtained taking Q^2 between 10^{-7} GeV² and 1 GeV². For comparison we show the results for $q_{\gamma^*} g_p \rightarrow \gamma q$ and $q_{\gamma^*} \bar{q}_p (\bar{q}_{\gamma^*} q_p) \rightarrow \gamma g$ processes obtained using $Q^2 = 0.1$ GeV².

The large dominance of the contribution due to the gluonic content of the virtual photon over the Born contribution is seen at large η_γ in the whole considered range of the photon virtualities. The largest ratio, up to factor of 35, is obtained for the small virtualities. It is important since in the limit $Q^2 \rightarrow 0$ the value of the cross section is the largest. Thus the cross section integrated over Q^2 between 0 and, say, 1 GeV²¹ is also strongly dominated by the process $g_\gamma q_p \rightarrow \gamma q$ in the forward direction.

The process involving the gluonic content of the photon dominates at large η_γ not only over the Born contribution but also over the contribution of processes involving quarks from the photon, see Fig. 7.1 and Ref. [92]. This gives an opportunity of measuring the gluon content of the real and virtual photon at HERA.

¹This range of Q^2 is considered for the photoproduction of prompt photons at HERA, see Sec. 2.3.

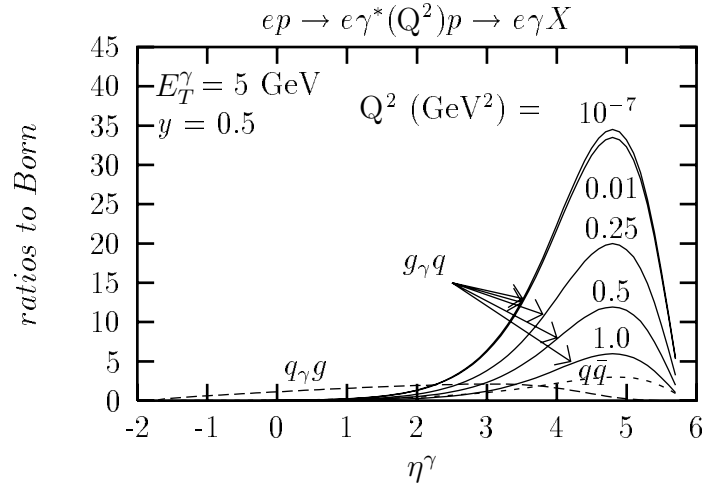


Figure 7.1: The results for the $ep \rightarrow e\gamma X$ reaction including non-zero virtualities, Q^2 , of the mediating photon obtained for $y=0.5$ and $E_T^\gamma = 5$ GeV. The curves represent the cross section (7.6) for the $g_\gamma^* q_p \rightarrow \gamma q$ (solid lines), $q_\gamma^* g_p \rightarrow \gamma q$ (long-dashed line) as well as $\bar{q}_\gamma^* q_p \rightarrow \gamma g$ and $q_\gamma^* \bar{q}_p \rightarrow \gamma g$ (short-dashed line) processes divided by the corresponding Born contribution. The predictions for $g_\gamma^* q_p \rightarrow \gamma q$ process are obtained with $Q^2 = 10^{-7}, 0.01, 0.25, 0.5$ and 1 GeV², while for the other processes involving resolved photons $Q^2 = 0.1$ GeV² was used.

Chapter 8

Summary

We have presented a NLO QCD calculation for the photoproduction of the isolated photons and the isolated photons associated with jets at the DESY HERA ep collider.

Our calculation includes set of diagrams different than other existing NLO QCD calculations for this process. This difference arises from different treatment of parton densities in the photon and parton-to-photon fragmentation functions. In our approach these parton densities and fragmentation functions are of order $\mathcal{O}(\alpha)$ while in most of other calculations they are treated as quantities being of order $\mathcal{O}(\alpha/\alpha_S)$. Our counting originate from the fact that the “structure” of the photon and the fragmentation into the photon arises from the purely electromagnetic processes $\gamma \rightarrow q\bar{q}$ and $q \rightarrow \gamma\bar{q}$, respectively. It ensures a cancellation to a large extend of dependences on the choice of the renormalization/factorization scale μ in the cross section.

We have presented a method to divide (slice) the three-body phase space which differs from methods applied in other calculations for the considered process. Our method allows to obtain relatively simple analytical singular-free formulae for the $\mathcal{O}(\alpha_S)$ corrections in each part of the phase space. Dividing of the phase space is introduced in order to implement exactly isolation restrictions and other kinematic cuts. It was used to obtain predictions for the isolated photon and isolated photon plus jet production at HERA.

The numerical predictions obtained using the phase space slicing were compared with the predictions obtained using the small cone approximation. In this approximation the isolation cuts in the $\mathcal{O}(\alpha_S)$ corrections to the Born process are implemented in an approximated way while in other contributions the isolation is implemented exactly. We confirm the observation of other author, that the small cone approximation gives very accurate predictions. However we have found that it is due to the fact that the $\mathcal{O}(\alpha_S)$ corrections to the Born process are small. These $\mathcal{O}(\alpha_S)$ corrections alone are obtained within the small cone approximation with very low accuracy.

The theoretical uncertainties of our predictions are well under control. The predictions vary within 10% for various used parton parametrizations. The dependence on the choice of the renormalization/factorization scale μ for the isolated photon (isolated photon plus jet) productions is below $\pm 6\%$ ($\pm 5\%$) in each considered kinematic region, and the average dependence is $\pm 5\%$ ($\pm 3\%$). This small sensitivity to the choice of μ

may indicate that the not included contributions of higher orders (NNLO or higher) are not sizable.

Other NLO QCD calculations (including some diagrams which are of NNLO order from our point of view) give predictions 10-20% (4%) higher on the average than ours for the isolated photon (isolated photon plus jet) production. However there are some kinematic ranges where the differences are larger, up to 70% for the isolated photon production in the range $0.5 < y < 0.9$ and $0.7 < \eta^\gamma < 0.9$ (where our predictions give the best description of the data). This large difference is not supported by our study of the sensitivity to the choice of μ , which seems to suggest smaller effect of higher order contributions. To understand these differences we should know the dependence of other predictions on the scale μ in this particular range, which however was not provided.

We have studied in details the influence of the isolation restrictions as well as other experimental cuts. In particular, we have shown that the measurements in the central rapidity range considered in current experiments are not much sensitive to the parton densities in the photon in the low- x_γ region.

Effects of symmetric cuts for the photon and jet transverse energies were studied. We have found that the NLO differential cross section $d\sigma/dE_T^\gamma$ is a discontinuous function at $E_T^\gamma = E_{T,min}^{jet}$. This is due to constraints imposed on the phase space of soft gluons. We confirm the known result that to avoid theoretical uncertainties the asymmetric cuts are preferred.

Our predictions and computer program were used by experimental groups for comparison with data. The QCD predictions for the photon plus jet production tend to lie below the data, nevertheless they agree with the data in most of bins. On the other hand, none of existing predictions describes the data satisfactory well for the photon production with no cuts for the jet. It means that the cuts for the observed jet remove from the cross section contributions of such kinematic configurations for which the disagreement with the data and the differences between predictions are the largest.

Finally, we have pointed out the sensitivity of the Deep Inelastic Compton cross section to the gluon density in the photon also for the virtual photon. We presented a formula which allows to include the parton densities in the virtual photon in the cross section for the $ep \rightarrow e\gamma X$ (or $ep \rightarrow e\gamma \text{ jet } X$) reaction. We have found that, as it was expected, the processes initiated by the gluon arising from the photon dominate in the cross section in the forward direction, i.e. for large η_γ .

Tables

The tables contain our predictions for the $ep \rightarrow e\gamma X$ and $ep \rightarrow e\gamma \text{ jet } X$ photoproduction processes at the HERA collider. The initial electron and proton energies, the final photon isolation parameters ($\epsilon = 0.1$, $R = 1$) as well as the kinematic ranges of y , η^γ , η^{jet} , E_T^γ and E_T^{jet} are taken from the H1 [49] (Tabs. 1, 3) and ZEUS [42] (Tab. 2) Collaborations papers and are described in the captions of corresponding tables.

The following notation is used for various contributing processes:

- $\mathcal{O}(\alpha_S) = \mathcal{O}(\alpha_S)$ corrections to the Born process,
- dir,dir = direct initial and final γ ,
- dir,frag = direct initial γ and fragmentation into final γ ,
- res,dir = resolved initial γ and direct final γ ,
- res,frag = resolved initial γ and fragmentation into final γ .

Table 1: The cross section for the non-isolated (inclusive) photon, the isolated photon, and the isolated photon + jet production. The photon transverse energy is integrated over the range $5 \leq E_T^\gamma \leq 10$ GeV. The initial electron and proton energies are $E_e = 27.6$ GeV and $E_p = 920$ GeV [49]. The results for the non-isolated photon are integrated over the whole range of y and η^γ . The isolated photon cross section is calculated for $0.2 \leq y \leq 0.7$ and $-1. \leq \eta^\gamma \leq 0.9$. For the photon+jet production there are additional cuts, $4.5 \text{ GeV} \leq E_T^{jet}$ and $-1. \leq \eta^{jet} \leq 2.3$.

| [pb] | total | dir,dir | | | res,dir | dir,frag | res,frag |
|---|-------|------------------|-------------------------|-----------------|------------------|-----------------|-----------------|
| | | Born | $\mathcal{O}(\alpha_S)$ | box | | | |
| non-isolated γ E_T^γ cut | 240.6 | 85.8 (35.6%) | 5.0 (2.1%) | 15.2 (6.3%) | 60.0 (25.0%) | 27.0 (11.2%) | 47.6 (19.8%) |
| isolated γ $y, E_T^\gamma, \eta_\gamma$ cuts | 37.77 | 15.23 (40.3%) | 1.76 (4.7%) | 4.34 (11.5%) | 12.63 (33.4%) | 1.49 (3.9%) | 2.33 (6.2%) |
| isolated γ +jet $y, E_T^\gamma, \eta_\gamma$ cuts E_T^{jet}, η_{jet} cuts | 29.45 | 11.60 (39.4%) | 0.19 (0.6%) | 3.41 (11.6%) | 11.45 (38.9%) | 1.20 (4.1%) | 1.59 (5.4%) |

Table 2: The cross section for the non-isolated (inclusive) and isolated final photon with $5 \leq E_T^\gamma \leq 10$ GeV. The initial energies are $E_e = 27.6$ GeV and $E_p = 820$ GeV [42]. The results for the isolated photon are obtained using the small cone approximation (Sec. 4) without and with cuts $0.2 \leq y \leq 0.9$ and $-0.7 \leq \eta^\gamma \leq 0.9$.

| [pb] | total | dir,dir | | | res,dir | dir,frag | res,frag |
|--|-------|------------------|-------------------------|----------------|------------------|-----------------|-----------------|
| | | Born | $\mathcal{O}(\alpha_S)$ | box | | | |
| non-isolated γ E_T^γ cut | 222.0 | 82.0 (36.9%) | 4.8 (2.2%) | 13.9 (6.3%) | 54.8 (24.7%) | 24.6 (11.1%) | 42.0 (18.9%) |
| isolated γ E_T^γ cut | 178.1 | 82.0 (46.0%) | 13.1 (7.4%) | 13.9 (7.8%) | 54.8 (30.8%) | 5.1 (2.9%) | 9.4 (5.3%) |
| isolated γ y, E_T^γ cuts | 71.95 | 23.60 (32.8%) | 6.02 (8.4%) | 6.53 (9.1%) | 28.18 (39.2%) | 2.34 (3.3%) | 5.28 (7.3%) |
| isolated γ $y, E_T^\gamma, \eta_\gamma$ cuts | 35.34 | 13.64 (38.6%) | 3.26 (9.2%) | 3.41 (9.6%) | 11.88 (33.6%) | 1.20 (3.4%) | 1.93 (5.5%) |

Table 3: The cross section for the isolated final photon with $E_e = 27.6$ GeV, $E_p = 920$ GeV, $0.2 \leq y \leq 0.9$, $-0.7 \leq \eta^\gamma \leq 0.9$ and $5 \leq E_T^\gamma \leq 10$ GeV [49]. The results are obtained with (upper row) and without (lower row) the small cone approximation (Sec. 5).

| [pb] | total | dir,dir | | | res,dir | dir,frag | res,frag |
|--------------|-------|---------|-------------------------|------|---------|----------|----------|
| | | Born | $\mathcal{O}(\alpha_S)$ | box | | | |
| approximated | 38.93 | 15.23 | 2.94 | 4.34 | 12.63 | 1.49 | 2.33 |
| exact | 37.77 | 15.23 | 1.76 | 4.34 | 12.63 | 1.49 | 2.33 |

Appendix A

Kinematics and notation

A.1 $2 \rightarrow 2$ processes

We study the production of photons and jets in the electron-proton scattering:

$$e(p_e) p(p_p) \rightarrow e(p'_e) \gamma(p_\gamma) jet(p_{jet}) X(p_X), \quad (\text{A.1})$$

where four-momenta of particles are given in brackets, and assume that the mediating photon is quasi-real,

$$Q^2 = -(p_e - p'_e)^2 \approx 0. \quad (\text{A.2})$$

In such processes the emission of the mediating photon from the electron can be factored out (Sec. 2.3) and we can consider the photon-proton scattering:

$$\gamma(q) p(p_p) \rightarrow \gamma(p_\gamma) jet(p_{jet}) X(p_X), \quad (\text{A.3})$$

where $q = yp_p$ is the four-momentum of the mediating photon. This photon may interact with a parton from the proton directly or as a resolved one, see Eq. (4.6). The corresponding $2 \rightarrow 2$ partonic processes are:

$$a(p_a) b(p_b) \rightarrow c(p_c) d(p_d), \quad (\text{A.4})$$

where

$$p_a = x_\gamma q = x_\gamma y p_e \quad , \quad p_b = x p_p \quad , \quad p_c = p_\gamma / z. \quad (\text{A.5})$$

We introduce the standard variables:

$$s = (p_a + p_b)^2 \quad , \quad t = (p_a - p_c)^2 \quad , \quad u = (p_b - p_c)^2, \quad (\text{A.6})$$

which are used in next Appendices and in formulae for the cross sections.

A.2 $2 \rightarrow 3$ processes

Now, we consider the $2 \rightarrow 3$ partonic processes contributing to the $ep \rightarrow e\gamma$ (*jet*) X reaction: $\gamma q \rightarrow \gamma qg$ (Fig. 2.3) and $\gamma g \rightarrow \gamma q\bar{q}$ (Fig. 2.4). We write

$$\gamma(q) + q(p) \rightarrow \gamma(p_\gamma) + q(p_1) + g(p_2) \quad (\text{see Fig. A.1}), \quad (\text{A.7})$$

and

$$\gamma(q) + g(p) \rightarrow \gamma(p_\gamma) + q(p_1) + \bar{q}(p_2). \quad (\text{A.8})$$

We use the variables s , t and u defined in Appendix A.1, which for the direct both initial and final photon ($x_\gamma = z = 1$) are given by

$$s = (q + p)^2, \quad t = (q - p_\gamma)^2, \quad u = (p - p_\gamma)^2. \quad (\text{A.9})$$

Finally, we define the scaled variables v and w :

$$v = 1 + t/s, \quad w = -u/(t + s). \quad (\text{A.10})$$

The variables v and w are in the range from 0 to 1: $0 \leq v \leq 1$ and $0 \leq w \leq 1$. Note, that for massless particles

$$(p_1 + p_2)^2 = sv(1 - w), \quad (\text{A.11})$$

and in the limit $(p_1 + p_2)^2 \rightarrow 0$ one obtains $w \rightarrow 1$ (v can not be too low, since the final photon has a large transverse momentum). For the $2 \rightarrow 2$ processes one has $w = 1$ by definition.

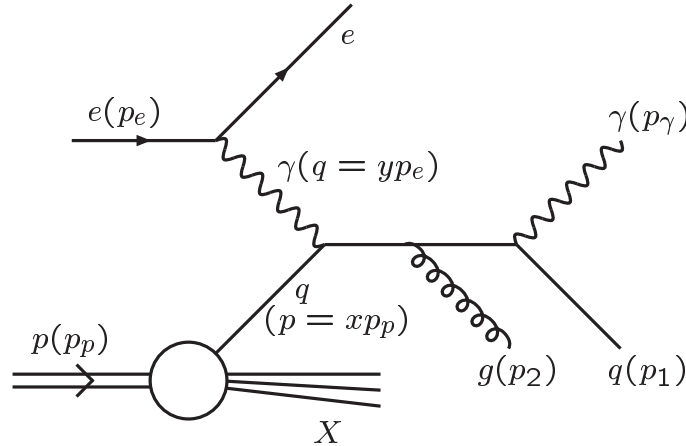


Figure A.1: An example of the $2 \rightarrow 3$ NLO process contributing to the $ep \rightarrow e\gamma$ (*jet*) X reaction. The four-momenta of particles are given in brackets.

Appendix B

Cross sections for $2 \rightarrow 2$ processes

In this Appendix we have collected all the tree-level cross sections for $2 \rightarrow 2$ processes which are included in our calculation. The virtual gluon corrections to the Born process are included in Appendix D together with the real gluon corrections.

The cross sections for $2 \rightarrow 2$ processes shown in Figs. 2.1, 2.7-2.11 are given by the equation

$$E_\gamma \frac{d^3\sigma^{ab \rightarrow cd}}{d^3p_\gamma}(s, t, u) = \frac{1}{(4\pi)^2 s} \cdot |\overline{M}^{ab \rightarrow cd}|^2(s, t, u) \cdot \delta(s + t + u), \quad (\text{B.1})$$

where $|\overline{M}^{ab \rightarrow cd}|^2$ are the squared matrix elements:

$$|\overline{M}^{\gamma q \rightarrow \gamma q}|^2(s, t, u) = -2(4\pi)^2 \alpha^2 e_q^4 \left(\frac{u}{s} + \frac{s}{u} \right), \quad (\text{B.2})$$

$$|\overline{M}^{qg \rightarrow \gamma q}|^2(s, t, u) = -\frac{1}{3}(4\pi)^2 \alpha \alpha_S e_q^2 \left(\frac{t}{s} + \frac{s}{t} \right), \quad (\text{B.3})$$

$$|\overline{M}^{q\bar{q} \rightarrow \gamma g}|^2(s, t, u) = \frac{8}{9}(4\pi)^2 \alpha \alpha_S e_q^2 \left(\frac{t}{u} + \frac{u}{t} \right), \quad (\text{B.4})$$

$$|\overline{M}^{gq \rightarrow \gamma q}|^2(s, t, u) = |\overline{M}^{qg \rightarrow \gamma q}|^2(s, u, t), \quad (\text{B.5})$$

$$|\overline{M}^{\gamma q \rightarrow qg}|^2(s, t, u) = -\frac{8}{3}(4\pi)^2 \alpha \alpha_S e_q^2 \left(\frac{t}{s} + \frac{s}{t} \right), \quad (\text{B.6})$$

$$|\overline{M}^{\gamma q \rightarrow gq}|^2(s, t, u) = |\overline{M}^{qg \rightarrow qg}|^2(s, u, t), \quad (\text{B.7})$$

$$|\overline{M}^{\gamma g \rightarrow q\bar{q}}|^2(s, t, u) = (4\pi)^2 \alpha \alpha_S e_q^2 \left(\frac{t}{u} + \frac{u}{t} \right), \quad (\text{B.8})$$

$$|\overline{M}^{gq \rightarrow qg}|^2(s, t, u) = (4\pi)^2 \alpha_S^2 \left[-\frac{4}{9} \left(\frac{t}{s} + \frac{s}{t} \right) + \frac{s^2 + t^2}{u^2} \right], \quad (\text{B.9})$$

$$|\overline{M}^{gq \rightarrow gq}|^2(s, t, u) = |\overline{M}^{gq \rightarrow qg}|^2(s, u, t), \quad (\text{B.10})$$

$$|\overline{M}^{qg \rightarrow qg}|^2(s, t, u) = |\overline{M}^{gq \rightarrow qg}|^2(s, u, t), \quad (\text{B.11})$$

$$|\overline{M}^{qg \rightarrow gq}|^2(s, t, u) = |\overline{M}^{gq \rightarrow qg}|^2(s, t, u), \quad (\text{B.12})$$

$$|\overline{M}^{qq' \rightarrow q'q}|^2(s, t, u) = (4\pi)^2 \alpha_S^2 \left[\frac{4}{9} \frac{s^2 + u^2}{t^2} \right], \quad (\text{B.13})$$

$$|\overline{M}^{qq' \rightarrow q'q}|^2(s, t, u) = |\overline{M}^{qq' \rightarrow qq'}|^2(s, u, t), \quad (\text{B.14})$$

$$|\overline{M}^{qq \rightarrow qq}|^2(s, t, u) = (4\pi)^2 \alpha_S^2 \left[\frac{4}{9} \left(\frac{s^2 + u^2}{t^2} + \frac{s^2 + t^2}{u^2} \right) - \frac{8}{27} \frac{s^2}{tu} \right], \quad (\text{B.15})$$

$$|\overline{M}^{q\bar{q} \rightarrow q\bar{q}}|^2(s, t, u) = (4\pi)^2 \alpha_S^2 \left[\frac{4}{9} \left(\frac{s^2 + u^2}{t^2} + \frac{u^2 + t^2}{s^2} \right) - \frac{8}{27} \frac{u^2}{st} \right], \quad (\text{B.16})$$

$$|\overline{M}^{q\bar{q} \rightarrow q\bar{q}}|^2(s, t, u) = |\overline{M}^{q\bar{q} \rightarrow q\bar{q}}|^2(s, u, t), \quad (\text{B.17})$$

$$|\overline{M}^{q\bar{q} \rightarrow q'q'}|^2(s, t, u) = (4\pi)^2 \alpha_S^2 \left[\frac{4}{9} \frac{t^2 + u^2}{s^2} \right], \quad (\text{B.18})$$

$$|\overline{M}^{gg \rightarrow q\bar{q}}|^2(s, t, u) = (4\pi)^2 \alpha_S^2 \left[\frac{1}{6} \left(\frac{t}{u} + \frac{u}{t} \right) - \frac{3}{8} \frac{t^2 + u^2}{s^2} \right], \quad (\text{B.19})$$

$$|\overline{M}^{q\bar{q} \rightarrow gg}|^2(s, t, u) = (4\pi)^2 \alpha_S^2 \left[\frac{32}{27} \left(\frac{t}{u} + \frac{u}{t} \right) - \frac{8}{3} \frac{t^2 + u^2}{s^2} \right], \quad (\text{B.20})$$

$$|\overline{M}^{gg \rightarrow gg}|^2(s, t, u) = \frac{9}{2} (4\pi)^2 \alpha_S^2 \left(3 - \frac{tu}{s^2} - \frac{su}{t^2} - \frac{st}{u^2} \right). \quad (\text{B.21})$$

The squared matrix element for the box process (Fig. 2.11) has a form:

$$|\overline{M}^{\gamma g \rightarrow \gamma g}|^2(s, t, u) = \frac{1}{16} \left(\frac{\alpha_S}{\alpha} \right)^2 \left(\sum_{q, \bar{q}} e_q^2 \right)^2 \left(|M_{11 \rightarrow 11}|^2 + |M_{22 \rightarrow 22}|^2 + \right. \\ \left. 2|M_{11 \rightarrow 22}|^2 + 2|M_{12 \rightarrow 12}|^2 + 2|M_{12 \rightarrow 21}|^2 \right), \quad (\text{B.22})$$

where the amplitudes $M_{ij \rightarrow kl}$ ($\sim \alpha^4$) are given by Eq. (1) in Ref. [68], and $M_{12 \rightarrow 21}(s, t, u) = M_{12 \rightarrow 12}(s, u, t)$.

Appendix C

Three-body phase space

The cross section for a $2 \rightarrow 3$ process is given by a general formula:

$$d\sigma^{2 \rightarrow 3} = \frac{1}{2s} d(P\mathcal{S})_3 |\overline{M}^{2 \rightarrow 3}|^2, \quad (\text{C.1})$$

where $(PS)_3$ is the three-body *phase space* in n dimensions:

$$(PS)_3 = \int \frac{d^n p_\gamma}{(2\pi)^{n-1}} \int \frac{d^n p_1}{(2\pi)^{n-1}} \int \frac{d^n p_2}{(2\pi)^{n-1}} \cdot (2\pi)^n \delta^n(q + p - p_\gamma - p_1 - p_2) \delta^+(p_\gamma^2) \delta^+(p_1^2) \delta^+(p_2^2). \quad (\text{C.2})$$

The integration of $(PS)_3$ over all four-momenta of two final partons is discussed e.g. in [119, 18, 25]. However, in order to impose the isolation of the final photon as well as cuts for the jet, we need to restrict the momenta of the final partons. To achieve this goal we integrate $(PS)_3$ considering various configurations of the final particles momenta, e.g. some collinear configurations, as described in Sec. 5.2. The integration of $(PS)_3$ including a collinear configuration, where two final particles move (almost) parallel to each other, was previously discussed e.g. in [101]. In comparison with [101] we simplified the integration over the final energies. Below we derive all formulae for $(PS)_3$ which are applied in Appendix D to obtain the cross sections for the $\mathcal{O}(\alpha_S)$ corrections to the Born process including e.g. the configurations where a final parton is collinear with the final photon or with the initial electron or proton.

The integration of $(PS)_3$ as well as the calculations of the cross sections for the $\mathcal{O}(\alpha_S)$ corrections to the Born process are performed in $n = 4 - 2\varepsilon$ dimensions using the *dimensional regularization*, see e.g. [1].

First, we integrate (C.2) over p_2 :

$$(PS)_3 = \frac{1}{(2\pi)^{2n-3}} \int d^n p_\gamma \int d^n p_1 \delta^+(p_\gamma^2) \delta^+(p_1^2) \delta^+((q + p - p_\gamma - p_1)^2). \quad (\text{C.3})$$

Next, we choose the z -axis along the initial proton momentum in any frame of reference, in which the collision is central, e.g. in the laboratory frame:

$$p = xE_p(1, \dots, 0, 1), \quad (\text{C.4})$$

$$q = yE_e(1, \dots, 0, -1) \quad (\text{C.5})$$

(the unspecified components are equal to zero). The collision has the rotational symmetry and we can perform an integration over $(n-3)$ azimuthal angles of the photon. Performing this integration as well as the integration over the photon energy, and making the change of variables we obtain:

$$\int d^n p_\gamma \delta^+(p_\gamma^2) = \frac{\pi^{1-\varepsilon}}{2\Gamma(1-\varepsilon)} \int dv \int dw [vws(1-v)]^{-\varepsilon} sv. \quad (\text{C.6})$$

Next, we chose the z and y axes this way that momenta \vec{p} , \vec{q} and \vec{p}_γ are in the zy -plane:

$$p = xE_p(1, \dots, 0, \sin \alpha, \cos \alpha), \quad (\text{C.7})$$

$$q = yE_e(1, \dots, 0, -\sin \alpha, -\cos \alpha), \quad (\text{C.8})$$

$$p_\gamma = E_\gamma(1, \dots, 0, \sin \alpha', \cos \alpha'), \quad (\text{C.9})$$

where α and α' are arbitrary, and the unspecified components in the additional $(n-4)$ dimensions are equal to zero. We write p_1 and p_2 in this frame:

$$p_1 = E(1, \dots, \cos \theta_3 \sin \theta_2 \sin \theta_1, \cos \theta_2 \sin \theta_1, \cos \theta_1), \quad (\text{C.10})$$

$$p_2 = p + q - p_\gamma - p_1. \quad (\text{C.11})$$

Since the four-momenta p , q and p_γ have only two non-zero space components, one can perform the integration over $(n-4)$ azimuthal angles of the final parton:

$$\int d^n p_1 \delta^+(p_1^2) = \frac{\pi^{\frac{1}{2}-\varepsilon}}{\Gamma(\frac{1}{2}-\varepsilon)} \int dE E^{1-2\varepsilon} \int d\theta_1 \sin^{1-2\varepsilon} \theta_1 \int d\theta_2 \sin^{-2\varepsilon} \theta_2. \quad (\text{C.12})$$

From (C.3), (C.6) and (C.12) one has

$$\begin{aligned} \frac{d(PS)_3}{dvdw} &= \frac{1}{4(2\pi)^n} \frac{1}{\Gamma(1-2\varepsilon)} [vws(1-v)]^{-\varepsilon} sv \cdot \\ &\cdot \int d\theta_1 \sin^{1-2\varepsilon} \theta_1 \int d\theta_2 \sin^{-2\varepsilon} \theta_2 \int dE E^{1-2\varepsilon} \delta^+((q+p-p_\gamma-p_1)^2). \end{aligned} \quad (\text{C.13})$$

Note, that the integration over E is straightforward as the argument of the δ function is a linear function of p_1 : $(q+p-p_\gamma-p_1)^2 = (q+p-p_\gamma)^2 - 2p_1(q+p-p_\gamma)$. The expression (C.13) was obtained with no approximations and can be used e.g. to calculate the cross section for $2 \rightarrow 3$ processes in Part 5 of the phase space described in Sec. 5.2.

In order to obtain $(PS)_3$ in a form suitable for considering collinear configurations in Part 2, 3 and 4, we assume that θ_1 is small:

$$\theta_1 \approx 0, \quad (\text{C.14})$$

APPENDIX C. THREE-BODY PHASE SPACE

and take in Eqs. (C.7-C.9) $\alpha = \pi$ or $\alpha = 0$ or $\alpha' = 0$. With these assumptions we obtain:

$$\begin{aligned} \frac{d(PS)_3}{dvdw} &= \\ &= \Theta(1-w) \frac{[svw(1-v)]^{-\varepsilon}}{4(2\pi)^n \Gamma(1-2\varepsilon)} \cdot \frac{E^{2-2\varepsilon}}{1-w} \int d\theta_1 \int d\theta_2 \sin^{1-2\varepsilon} \theta_1 \sin^{-2\varepsilon} \theta_2, \end{aligned} \quad (\text{C.15})$$

where

- for $\alpha = \pi$:

$$E = (1-w)yE_e, \quad (\text{C.16})$$

- for $\alpha = 0$:

$$E = \frac{v(1-w)}{1-vw} xE_p, \quad (\text{C.17})$$

- for $\alpha' = 0$:

$$E = \frac{v(1-w)}{1-v+vw} E_\gamma. \quad (\text{C.18})$$

Of course, the same formulae for $(PS)_3$ are valid if we replace p_1 with p_2 :

$$p_2 = E(1, \dots \cos \theta_3 \sin \theta_2 \sin \theta_1, \cos \theta_2 \sin \theta_1, \cos \theta_1), \quad (\text{C.19})$$

$$p_1 = p + q - p_\gamma - p_2. \quad (\text{C.20})$$

Appendix D

Corrections of order $\mathcal{O}(\alpha_s)$ to the Born process

In this Appendix we present formulae for $\mathcal{O}(\alpha_s)$ corrections (Figs. 2.2-2.4) to the Born process (Fig. 2.1). The general (unintegrated) formulae (Appendix D.1) and the formulae for the non-isolated photon production (Appendix D.2) are taken from the literature [18, 25]. The cross sections corresponding to various collinear configurations described in Sec. 5.2 are derived briefly in Appendices D.3, D.4 and D.5.

D.1 General formulae for $2 \rightarrow 3$ processes

The general formula for the squared matrix element for the $\gamma q \rightarrow \gamma qg$ process has the form [18, 25]:

$$|\overline{M}^{\gamma q \rightarrow \gamma qg}|^2 = \frac{2(4\pi)^3 \alpha^2 \alpha_s \hat{\mu}^{6\epsilon} c}{a_1 a_2 a_3 b_1 b_2 b_3} e_q^4 C_F [A_1 - \varepsilon(2A_1 - A_2 + 2A_3 - 8A_4) + \mathcal{O}(\varepsilon^2)], \quad (\text{D.1})$$

where $\hat{\mu}$ is an arbitrary mass scale, $C_F = 4/3$ and the terms A_i , a_i , b_i , c are given by

$$A_1 = a_1 b_1 (a_1^2 + b_1^2) + a_2 b_2 (a_2^2 + b_2^2) + a_3 b_3 (a_3^2 + b_3^2) \quad (\text{D.2})$$

$$A_2 = a_1 b_1 (a_2 + b_2)(a_3 + b_3) - a_2 b_2 (a_1 + b_1)(a_3 + b_3) - a_3 b_3 (a_1 + b_1)(a_2 + b_2) \quad (\text{D.3})$$

$$A_3 = a_1^2 b_1^2 + a_2^2 b_2^2 + a_3^2 b_3^2 \quad (\text{D.4})$$

$$A_4 = a_1 b_1 a_2 b_2 + a_1 b_1 a_3 b_3 + a_2 b_2 a_3 b_3 \quad (\text{D.5})$$

and

$$a_1 = pq = \frac{s}{2}, \quad (\text{D.6})$$

APPENDIX D. CORRECTIONS OF ORDER $\mathcal{O}(\alpha_S)$ TO THE BORN PROCESS

$$a_2 = pp_\gamma = \frac{s}{2}vw, \quad (\text{D.7})$$

$$a_3 = pp_2, \quad (\text{D.8})$$

$$b_1 = p_1q, \quad (\text{D.9})$$

$$b_2 = p_1p_\gamma, \quad (\text{D.10})$$

$$b_3 = p_1p_2 = \frac{s}{2}v(1-w), \quad (\text{D.11})$$

$$c = pp_1. \quad (\text{D.12})$$

The same formula (D.1) is valid for the squared matrix element of the $\gamma g \rightarrow \gamma q \bar{q}$ process, $|\overline{M}^{\gamma g \rightarrow \gamma q \bar{q}}|^2$, but with the factor 1/2 instead of C_F , with no $\mathcal{O}(\varepsilon^2)$ term, and with the coefficients $a'_1, a'_2, a'_3, b'_1, b'_2, b'_3$ and c' instead of $a_1, a_2, a_3, b_1, b_2, b_3$ and c , where the coefficients with the prime are given by:

$$a'_1 = -p_2q, \quad (\text{D.13})$$

$$a'_2 = -p_2p_\gamma, \quad (\text{D.14})$$

$$a'_3 = a_3, \quad (\text{D.15})$$

$$b'_1 = b_1, \quad (\text{D.16})$$

$$b'_2 = b_2, \quad (\text{D.17})$$

$$b'_3 = -c, \quad (\text{D.18})$$

$$c' = -b_3. \quad (\text{D.19})$$

The above squared matrix elements are used (with $\varepsilon = 0$) to calculate the cross sections for the $\mathcal{O}(\alpha_S)$ corrections to the Born process in Part 5 of the phase space (see Sec. 5.2):

$$E_\gamma \frac{d\sigma_{\alpha_S(5)}^{2 \rightarrow 3}}{d^3p_\gamma} = \frac{1}{sv\pi} \cdot \frac{1}{2s} \frac{d(P_S)_3}{dvdw} |\overline{M}^{2 \rightarrow 3}|^2, \quad (\text{D.20})$$

where the three-body phase space is given by Eq. C.13.

D.2 Inclusive photon cross section

The cross sections for the $\mathcal{O}(\alpha_S)$ corrections to the Born process, integrated over all momenta of final partons are given by [18, 25]:

$$\begin{aligned}
 E_\gamma \frac{d}{d^3 p_\gamma} [\sigma_{\alpha_S}^{\gamma q \rightarrow \gamma q} + \sigma_{\alpha_S}^{\gamma q \rightarrow \gamma qg}] &= \Theta(1-w) \frac{\alpha^2 \alpha_S}{\pi s^2} e_q^4 C_F \cdot \left[c_1 \delta(1-w) + \right. \\
 &c_2 \left(\frac{1}{1-w} \right)_+ + c_3 \left(\frac{\ln(1-w)}{1-w} \right)_+ + \left(c D_4 \delta(1-w) + \right. \\
 &c W_4 \left(\frac{1}{1-w} \right)_+ + c_4 \left. \right) \ln \frac{s}{\mu^2} + c_5 \ln v + c_6 \ln(1-vw) + \\
 &c_7 \ln(1-v+vw) + c_8 \ln(1-v) + c_9 \ln w + c_{10} \ln(1-w) + c_{11} + \\
 &c_{12} \frac{\ln(1-v+vw)}{1-w} + c_{13} \frac{\ln w}{1-w} + c_{14} \frac{\ln((1-vw)/(1-v))}{1-w} \Big], \tag{D.21}
 \end{aligned}$$

$$\begin{aligned}
 E_\gamma \frac{d\sigma_{\alpha_S}^{\gamma q \rightarrow \gamma q\bar{q}}}{d^3 p_\gamma} &= \Theta(1-w) \frac{\alpha^2 \alpha_S}{\pi s^2} e_q^4 \frac{1}{2} \left[c'_4 \ln \frac{s}{\mu^2} + c'_5 \ln v + c'_6 \ln(1-vw) + \right. \\
 &c'_7 \ln(1-v+vw) + c'_8 \ln(1-v) + c'_9 \ln w + c'_{10} \ln(1-w) + c'_{11} + \\
 &c'_{12} \frac{\ln(1-v+vw)}{1-w} + c'_{13} \frac{\ln w}{1-w} + c'_{14} \frac{\ln((1-vw)/(1-v))}{1-w} \Big], \tag{D.22}
 \end{aligned}$$

where the coefficients c and c' are given in Appendix B in the paper [18]. We use formulae (D.21) and (D.22) to obtain the $\mathcal{O}(\alpha_S)$ corrections for the non-isolated photon production (Chapters 3, 4) as well as to obtain the $\mathcal{O}(\alpha_S)$ corrections for the isolated photon in Part 1 of the phase space, as defined in Sec. 5.2 (Chapters 5, 6).

D.3 Collinear configuration ($\vec{p}_1 || \vec{p}_e$ or $\vec{p}_2 || \vec{p}_e$)

In this Appendix we consider the configuration corresponding to the Part 2 of the phase space defined in Sec. 5.2. First, we assume that the momentum of the final quark, \vec{p}_1 , is almost parallel to the momentum of the initial photon originating from the electron, \vec{q} ($= y \vec{p}_e$). We orient the axes this way that

$$q = y E_e (1, \dots, 0, 0, 1), \tag{D.23}$$

$$p = x E_p (1, \dots, 0, 0, -1), \tag{D.24}$$

APPENDIX D. CORRECTIONS OF ORDER $\mathcal{O}(\alpha_S)$ TO THE BORN PROCESS

$$p_\gamma = E_\gamma(1, \dots, 0, \sin \alpha', \cos \alpha'), \quad (\text{D.25})$$

$$p_1 = E(1, \dots, \cos \theta_2 \sin \theta_1, \cos \theta_1), \quad (\text{D.26})$$

$$p_2 = q + p - p_\gamma - p_1, \quad (\text{D.27})$$

where

$$E_\gamma = xE_p(1 - v) + yE_e v w, \quad (\text{D.28})$$

$$\sin \alpha' = \frac{\sqrt{s(1 - v)vw}}{E_\gamma}, \quad (\text{D.29})$$

$$\cos \alpha' = -\frac{x E_p(1 - v) - y E_e v w}{E_\gamma}. \quad (\text{D.30})$$

$$E = (1 - w)yE_e, \quad (\text{D.31})$$

$$0 \leq \theta_1 \leq \theta_{cut} \ll 1. \quad (\text{D.32})$$

From Eqs. (C.1, C.15, C.16, D.1-D.19) we obtain the cross sections which contain terms $\sim 1/\varepsilon$ being singular in 4 dimensions:

$$E_\gamma \frac{d\sigma_{\alpha_S(2)}^{\gamma q \rightarrow \gamma q g}}{d^3 p_\gamma} \Big|_{singular} = \frac{1}{sv\pi} \cdot \frac{1}{2s} \frac{d(PS)_3}{dv dw} |\overline{M}^{\gamma q \rightarrow \gamma q g}|^2 \sim \mathcal{O}\left(\frac{1}{\varepsilon}\right) + \mathcal{O}(1) + \dots, \quad (\text{D.33})$$

$$E_\gamma \frac{d\sigma_{\alpha_S(2)}^{\gamma g \rightarrow \gamma q \bar{q}}}{d^3 p_\gamma} \Big|_{singular} = \frac{1}{sv\pi} \cdot \frac{1}{2s} \frac{d(PS)_3}{dv dw} |\overline{M}^{\gamma g \rightarrow \gamma q \bar{q}}|^2 \sim \mathcal{O}\left(\frac{1}{\varepsilon}\right) + \mathcal{O}(1) + \dots, \quad (\text{D.34})$$

We remove these singularities applying the standard factorization procedure (see e.g. [18, 25]):

$$E_\gamma \frac{d\sigma_{\alpha_S(2)}^{\gamma q \rightarrow \gamma q g}}{d^3 p_\gamma} = E_\gamma \frac{d\sigma_{\alpha_S(2)}^{\gamma q \rightarrow \gamma q g}}{d^3 p_\gamma} \Big|_{singular} - \int_0^1 d\xi H_{q\gamma}(\xi, \mu) E_\gamma \frac{d\sigma^{q\bar{q} \rightarrow \gamma g}}{d^3 p_\gamma}(\xi s, \xi t, u), \quad (\text{D.35})$$

$$E_\gamma \frac{d\sigma_{\alpha_S(2)}^{\gamma g \rightarrow \gamma q \bar{q}}}{d^3 p_\gamma} = E_\gamma \frac{d\sigma_{\alpha_S(2)}^{\gamma g \rightarrow \gamma q \bar{q}}}{d^3 p_\gamma} \Big|_{singular} - \int_0^1 d\xi H_{q\gamma}(\xi, \mu) E_\gamma \frac{d\sigma^{qg \rightarrow \gamma q}}{d^3 p_\gamma}(\xi s, \xi t, u), \quad (\text{D.36})$$

with

$$H_{q\gamma}(\xi, \mu) = -\frac{1}{\varepsilon} \frac{\alpha}{2\pi} 3e_q^2 [\xi^2 + (1 - \xi)^2] \left(\frac{4\pi\hat{\mu}^2}{\mu^2} \right)^\varepsilon \frac{\Gamma(1 - \varepsilon)}{\Gamma(1 - 2\varepsilon)} + \mathcal{O}(\varepsilon), \quad (\text{D.37})$$

$$E_\gamma \frac{d\sigma^{q\bar{q} \rightarrow \gamma g}}{d^3 p_\gamma}(s, t, u) = \frac{2\pi\alpha\alpha_S e_q^2}{3s} C_F \frac{\hat{\mu}^{2\varepsilon}}{\Gamma(1-\varepsilon)} \left(\frac{4\pi\hat{\mu}^2 s}{tu} \right)^\varepsilon \cdot (1-\varepsilon) \left[(1-\varepsilon) \left(\frac{t}{u} + \frac{u}{t} \right) - 2\varepsilon \right], \quad (\text{D.38})$$

$$E_\gamma \frac{d\sigma^{gg \rightarrow \gamma q}}{d^3 p_\gamma}(s, t, u) = \frac{2\pi\alpha\alpha_S e_q^2}{3s} \frac{1}{2} \frac{\hat{\mu}^{2\varepsilon}}{\Gamma(1-\varepsilon)} \left(\frac{4\pi\hat{\mu}^2 s}{tu} \right)^\varepsilon \cdot (1-\varepsilon) \left[-(1-\varepsilon) \left(\frac{t}{s} + \frac{s}{t} \right) - 2\varepsilon \right], \quad (\text{D.39})$$

where $\hat{\mu}$ is an arbitrary mass scale. Finally, we obtain the singular-free $\mathcal{O}(\alpha_S)$ corrections to the Born process in the region of the phase space labeled as Part 2 (Sec. 5.2):

$$E_\gamma \frac{d\sigma_{\alpha_S(2)}^{\gamma q \rightarrow \gamma qg}}{d^3 p_\gamma} = \theta(1-w) \frac{\alpha^2 \alpha_S e_q^4}{\pi s^2 v w} C_F \frac{v^2 + (1-v)^2}{v(1-v)} \cdot \left[[w^2 + (1-w)^2] \ln \frac{(yE_e)^2 \theta_{cut}^2 (1-w)^2}{\mu^2} + 1 \right] \quad (\text{D.40})$$

$$E_\gamma \frac{d\sigma_{\alpha_S(2)}^{\gamma g \rightarrow \gamma q\bar{q}}}{d^3 p_\gamma} = \theta(1-w) \frac{\alpha^2 \alpha_S e_q^4}{\pi s^2 v w} \frac{1}{2} \frac{1 + (1-v)^2}{1-v} \cdot \left[[w^2 + (1-w)^2] \ln \frac{(yE_e)^2 \theta_{cut}^2 (1-w)^2}{\mu^2} + 1 \right] \quad (\text{D.41})$$

These cross sections (D.40, D.41) are equivalent to the results quoted in Sec. 5.2 in Eqs. (5.10, 5.11).

The squared matrix element $|\overline{M}^{\gamma q \rightarrow \gamma qg}|^2$ calculated for the gluon moving (almost) parallel to the initial electron, $\vec{p}_2||\vec{q} = y\vec{p}_e$ (see the notation in Eq. (A.7)), contains no collinear singularities and the cross section $d\sigma_{\alpha_S(2)}^{\gamma q \rightarrow \gamma qg}$ corresponding to this configuration can be obtained performing the exact numerical calculations as in Part 5 of the phase space (see Appendix D.1) or it can be neglected as it is a term of order $\mathcal{O}(\theta_{cut}^2)$.

On the other hand, the configuration corresponding to the final antiquark collinear to the initial electron, $\vec{p}_2||\vec{q} = y\vec{p}_e$ (see the notation in Eq. (A.8)), leads to the same contribution in the cross section $d\sigma_{\alpha_S(2)}^{\gamma g \rightarrow \gamma q\bar{q}}$ as the quark collinear to the electron, $\vec{p}_1||\vec{q} = y\vec{p}_e$, and this is included in Eq. (5.5) in the summation over $2N_f$ flavours.

D.4 Collinear configuration ($\vec{p}_1||\vec{p}_p$ or $\vec{p}_2||\vec{p}_p$)

Herein we derive the cross sections $d\sigma_{\alpha_S(3)}^{\gamma q \rightarrow \gamma qg}$ and $d\sigma_{\alpha_S(3)}^{\gamma g \rightarrow \gamma q\bar{q}}$ corresponding to the region of the phase space labeled in Sec. 5.2 as Part 3. First, we consider the final gluon moving almost parallel to the initial quark and the final antiquark moving almost

APPENDIX D. CORRECTIONS OF ORDER $\mathcal{O}(\alpha_S)$ TO THE BORN PROCESS

parallel to the initial gluon, $\vec{p}_2 || \vec{p} = x\vec{p}_p$ (see the notation in Eqs. (A.7, A.8)). We write the four-momenta in the laboratory frame with the z axis chosen along the direction of the initial proton momentum:

$$q = yE_e(1, \dots, 0, 0, -1), \quad (\text{D.42})$$

$$p = xE_p(1, \dots, 0, 0, 1), \quad (\text{D.43})$$

$$p_\gamma = E_\gamma(1, \dots, 0, \sin \alpha', \cos \alpha'), \quad (\text{D.44})$$

$$p_2 = E(1, \dots, \cos \theta_2 \sin \theta_1, \cos \theta_1), \quad (\text{D.45})$$

$$p_1 = q + p - p_\gamma - p_2, \quad (\text{D.46})$$

where

$$E_\gamma = xE_p(1 - v) + yE_e v w, \quad (\text{D.47})$$

$$\sin \alpha' = \frac{\sqrt{s(1 - v)vw}}{E_\gamma}, \quad (\text{D.48})$$

$$\cos \alpha' = \frac{xE_p(1 - v) - yE_e v w}{E_\gamma}, \quad (\text{D.49})$$

$$E = \frac{v(1 - w)}{1 - vw} xE_p, \quad (\text{D.50})$$

$$0 \leq \theta_1 \leq \theta_{cut} \ll 1. \quad (\text{D.51})$$

From Eqs. (C.1, C.15, C.17, D.1-D.5, D.13-D.19) we have the cross sections which are singular in 4 dimensions:

$$E_\gamma \frac{d\sigma_{\alpha_S(3)}^{\gamma q \rightarrow \gamma q g}}{d^3 p_\gamma} \Big|_{\text{singular}} = \frac{1}{sv\pi} \cdot \frac{1}{2s} \frac{d(PS)_3}{dv dw} |\overline{M}^{\gamma q \rightarrow \gamma q g}|^2 \sim \mathcal{O}\left(\frac{1}{\varepsilon}\right) + \mathcal{O}(1) + \dots, \quad (\text{D.52})$$

$$E_\gamma \frac{d\sigma_{\alpha_S(2)}^{\gamma g \rightarrow \gamma q \bar{q}}}{d^3 p_\gamma} \Big|_{\text{singular}} = \frac{1}{sv\pi} \cdot \frac{1}{2s} \frac{d(PS)_3}{dv dw} |\overline{M}^{\gamma g \rightarrow \gamma q \bar{q}}|^2 \sim \mathcal{O}\left(\frac{1}{\varepsilon}\right) + \mathcal{O}(1) + \dots, \quad (\text{D.53})$$

As in Appendix D.3, we remove these singularities applying the factorization procedure:

$$E_\gamma \frac{d\sigma_{\alpha_S(3)}^{\gamma q \rightarrow \gamma q g}}{d^3 p_\gamma} = E_\gamma \frac{d\sigma_{\alpha_S(3)}^{\gamma q \rightarrow \gamma q g}}{d^3 p_\gamma} \Big|_{\text{singular}} - \int_0^1 d\xi H_{qq}(\xi, \mu) E_\gamma \frac{d\sigma^{\gamma q \rightarrow \gamma q}}{d^3 p_\gamma}(\xi s, t, \xi u), \quad (\text{D.54})$$

$$E_\gamma \frac{d\sigma_{\alpha_S(3)}^{\gamma g \rightarrow \gamma q \bar{q}}}{d^3 p_\gamma} = E_\gamma \frac{d\sigma_{\alpha_S(3)}^{\gamma g \rightarrow \gamma q \bar{q}}}{d^3 p_\gamma} \Big|_{\text{singular}} - \int_0^1 d\xi H_{qg}(\xi, \mu) E_\gamma \frac{d\sigma^{\gamma q \rightarrow \gamma q}}{d^3 p_\gamma}(\xi s, t, \xi u), \quad (\text{D.55})$$

with

$$H_{qg}(\xi, \mu) = \frac{\alpha_S}{6\alpha e_q^2} H_{q\gamma}(\xi, \mu), \quad (\text{D.56})$$

$$H_{qg}(\xi, \mu) = -\frac{1}{\varepsilon} \frac{\alpha_S}{2\pi} C_F \frac{1+\xi^2}{1-\xi} \left(\frac{4\pi\hat{\mu}^2}{\mu^2} \right)^\varepsilon \frac{\Gamma(1-\varepsilon)}{\Gamma(1-2\varepsilon)} + \mathcal{O}(\varepsilon) \quad (\text{D.57})$$

and

$$E_\gamma \frac{d\sigma^{\gamma q \rightarrow \gamma q}}{d^3 p_\gamma}(s, t, u) = \frac{2\pi\alpha^2 e_q^4}{s} \frac{\hat{\mu}^{2\varepsilon}}{\Gamma(1-\varepsilon)} \left(\frac{4\pi\hat{\mu}^2 s}{tu} \right)^\varepsilon \cdot (1-\varepsilon) \left[-(1-\varepsilon) \left(\frac{u}{s} + \frac{s}{u} \right) - 2\varepsilon \right]. \quad (\text{D.58})$$

The final singular-free formulae for the $\mathcal{O}(\alpha_S)$ corrections to the Born process in Part 3 of the phase space are:

$$E_\gamma \frac{d\sigma_{\alpha_S(3)}^{\gamma q \rightarrow \gamma qg}}{d^3 p_\gamma} = \Theta(1-w) \frac{\alpha^2 \alpha_S e_q^4}{\pi s^2 (1-v)} C_F \left(vw + \frac{1}{vw} \right) \cdot \left[\frac{1+\hat{x}^2}{1-\hat{x}} \ln \frac{(xE_p)^2 \theta_{cut}^2 (1-\hat{x})^2}{\mu^2} + 1 - \hat{x} \right], \quad (\text{D.59})$$

$$E_\gamma \frac{d\sigma_{\alpha_S(3)}^{\gamma g \rightarrow \gamma q \bar{q}}}{d^3 p_\gamma} = \Theta(1-w) \frac{\alpha^2 \alpha_S e_q^4}{\pi s^2 (1-v)} \frac{1}{2} \left(vw + \frac{1}{vw} \right) \cdot \left[(\hat{x}^2 + (1-\hat{x})^2) \ln \frac{(xE_p)^2 \theta_{cut}^2 (1-\hat{x})^2}{\mu^2} + 1 \right], \quad (\text{D.60})$$

where

$$\hat{x} = \frac{1-v}{1-vw}. \quad (\text{D.61})$$

These formulae are equivalent to the formulae (5.12, 5.13) in Sec. 5.3.

The squared matrix element $|\overline{M}^{\gamma q \rightarrow \gamma qg}|^2$ calculated for the final quark moving parallel to the initial quark, $\vec{p}_1||\vec{p} = x\vec{p}_p$ (see Eq. (A.7)), contains no collinear singularities and the cross section $d\sigma_{\alpha_S(3)}^{\gamma q \rightarrow \gamma qg}$ corresponding to this configuration can be either calculated numerically or neglected.

The configurations corresponding to the final quark or antiquark collinear to the initial electron, $\vec{p}_1||\vec{p} = x\vec{p}_p$ or $\vec{p}_2||\vec{p} = x\vec{p}_p$ (see Eq. (A.8)), give the same contributions to the cross section $d\sigma_{\alpha_S(3)}^{\gamma g \rightarrow \gamma q \bar{q}}$ and this is included in Eq. (5.5) in the summation over $2N_f$ flavours.

D.5 Collinear configuration ($\vec{p}_1 || \vec{p}_\gamma$)

Now, we choose the z axis in the direction of the final photon momentum:

$$q = yE_e(1, \dots, 0, -\sin \alpha, -\cos \alpha), \quad (\text{D.62})$$

$$p = xE_p(1, \dots, 0, \sin \alpha, \cos \alpha), \quad (\text{D.63})$$

$$p_\gamma = E_\gamma(1, \dots, 0, 0, 1), \quad (\text{D.64})$$

$$p_1 = E(1, \dots, \cos \theta_2 \sin \theta_1, \cos \theta_1), \quad (\text{D.65})$$

$$p_2 = q + p - p_\gamma - p_1, \quad (\text{D.66})$$

with

$$E_\gamma = xE_p(1 - v) + yE_e v w, \quad (\text{D.67})$$

$$\sin \alpha = \frac{\sqrt{s(1 - v)vw}}{E_\gamma}, \quad (\text{D.68})$$

$$\cos \alpha = \frac{xE_p(1 - v) - yE_e v w}{E_\gamma}, \quad (\text{D.69})$$

$$E = \frac{v(1 - w)}{1 - v + vw} E_\gamma \equiv -\frac{s + t + u}{t + u} E_\gamma. \quad (\text{D.70})$$

We assume that the angle between the final quark momentum and the final photon momentum is small:

$$0 \leq \theta_1 \leq \delta_{cut} \ll 1, \quad (\text{D.71})$$

where δ_{cut} is a cut-off parameter. The partonic cross sections derived from Eqs. (C.1, C.15, C.18, D.1-D.12, D.20) contain the $1/\varepsilon$ singularity:

$$E_\gamma \frac{d\sigma_{\alpha_S(4)}^{\gamma q \rightarrow \gamma qg}}{d^3 p_\gamma} \Big|_{\text{singular}} = \frac{1}{sv\pi} \cdot \frac{1}{2s} \frac{d(PS)_3}{dv dw} |\overline{M}^{\gamma q \rightarrow \gamma qg}|^2 \sim \mathcal{O}\left(\frac{1}{\varepsilon}\right) + \mathcal{O}(1) + \dots, \quad (\text{D.72})$$

$$E_\gamma \frac{d\sigma_{\alpha_S(4)}^{\gamma g \rightarrow \gamma q\bar{q}}}{d^3 p_\gamma} \Big|_{\text{singular}} = \frac{1}{sv\pi} \cdot \frac{1}{2s} \frac{d(PS)_3}{dv dw} |\overline{M}^{\gamma g \rightarrow \gamma q\bar{q}}|^2 \sim \mathcal{O}\left(\frac{1}{\varepsilon}\right) + \mathcal{O}(1) + \dots \quad (\text{D.73})$$

The singularities are removed in the factorization procedure:

$$E_\gamma \frac{d\sigma_{\alpha_S(4)}^{\gamma q \rightarrow \gamma qg}}{d^3 p_\gamma} =$$

$$= E_\gamma \frac{d\sigma_{\alpha_S(4)}^{\gamma q \rightarrow \gamma qg}}{d^3 p_\gamma} \Big|_{singular} - \int_0^1 d\xi H_{\gamma q}(\xi, \mu) E_\gamma \frac{d\sigma^{\gamma q \rightarrow qg}}{d^3 p_\gamma}(s, t/\xi, u/\xi), \quad (D.74)$$

$$\begin{aligned} E_\gamma \frac{d\sigma_{\alpha_S(4)}^{\gamma g \rightarrow \gamma q\bar{q}}}{d^3 p_\gamma} &= \\ &= E_\gamma \frac{d\sigma_{\alpha_S(4)}^{\gamma g \rightarrow \gamma q\bar{q}}}{d^3 p_\gamma} \Big|_{singular} - \int_0^1 d\xi H_{\gamma q}(\xi, \mu) E_\gamma \frac{d\sigma^{\gamma g \rightarrow q\bar{q}}}{d^3 p_\gamma}(s, t/\xi, u/\xi), \end{aligned} \quad (D.75)$$

with

$$H_{\gamma q}(\xi, \mu) = -\frac{1}{\varepsilon} \frac{\alpha}{2\pi} e_q^2 \frac{1 + (1 - \xi)^2}{\xi} \left(\frac{4\pi\hat{\mu}^2}{\mu^2} \right)^\varepsilon \frac{\Gamma(1 - \varepsilon)}{\Gamma(1 - 2\varepsilon)} + \mathcal{O}(\varepsilon), \quad (D.76)$$

$$E_\gamma \frac{d\sigma^{\gamma q \rightarrow qg}}{d^3 p_\gamma}(s, t, u) = 8 E_\gamma \frac{d\sigma^{qg \rightarrow \gamma q}}{d^3 p_\gamma}(s, t, u), \quad (D.77)$$

$$E_\gamma \frac{d\sigma^{\gamma g \rightarrow q\bar{q}}}{d^3 p_\gamma}(s, t, u) = \frac{9}{8} E_\gamma \frac{d\sigma^{q\bar{q} \rightarrow \gamma g}}{d^3 p_\gamma}(s, t, u), \quad (D.78)$$

where the partonic cross sections $d\sigma^{\gamma q \rightarrow qg}$ and $d\sigma^{\gamma g \rightarrow q\bar{q}}$ are given in Appendix D.4. Finally, the $\mathcal{O}(\alpha_S)$ corrections to the Born process in Part 4 of the phase space are

$$\begin{aligned} E_\gamma \frac{d\sigma_{\alpha_S(4)}^{\gamma q \rightarrow \gamma qg}}{d^3 p_\gamma} &= \Theta(1 - w) \cdot \\ &\cdot \frac{\alpha^2 \alpha_S e_q^4}{\pi s^2 \hat{z}} C_F \frac{1 + (1 - \hat{v})^2}{1 - \hat{v}} \left[\frac{1 + (1 - \hat{z})^2}{\hat{z}} \ln \frac{E_\gamma^2 \delta_{cut}^2 (1 - \hat{z})^2}{\mu^2} + \hat{z} \right], \end{aligned} \quad (D.79)$$

$$\begin{aligned} E_\gamma \frac{d\sigma_{\alpha_S(4)}^{\gamma g \rightarrow \gamma q\bar{q}}}{d^3 p_\gamma} &= \Theta(1 - w) \cdot \\ &\cdot \frac{\alpha^2 \alpha_S e_q^4}{\pi s^2 \hat{z}} \frac{1}{2} \frac{\hat{v}^2 + (1 - \hat{v})^2}{\hat{v}(1 - \hat{v})} \left[\frac{1 + (1 - \hat{z})^2}{\hat{z}} \ln \frac{E_\gamma^2 \delta_{cut}^2 (1 - \hat{z})^2}{\mu^2} + \hat{z} \right], \end{aligned} \quad (D.80)$$

where

$$\hat{z} = 1 - v + vw, \quad (D.81)$$

$$\hat{v} = \frac{vw}{1 - v + vw}. \quad (D.82)$$

Since δ_{cut} is small, we have

$$E_\gamma \delta_{cut} \approx E_T^\gamma R_{cut}, \quad (D.83)$$

where R_{cut} is the cut-off radius in the rapidity and azimuthal angle space, see Sec. 5.2. From Eqs. (D.79), (D.80) and (D.83) one obtains Eqs. (5.15, 5.17) corresponding to Part 4 of the phase space as well as Eqs. (4.20, 4.22) for the subtraction terms in the small cone approximation.

D.6 Collinear configuration ($\vec{p}_2 || \vec{p}_\gamma$)

Finally, we assume that the momentum \vec{p}_2 is almost parallel with the momentum of the final photon, \vec{p}_γ :

$$q = yE_e(1, \dots, 0, -\sin \alpha, -\cos \alpha), \quad (\text{D.84})$$

$$p = xE_p(1, \dots, 0, \sin \alpha, \cos \alpha), \quad (\text{D.85})$$

$$p_\gamma = E_\gamma(1, \dots, 0, 0, 1), \quad (\text{D.86})$$

$$p_2 = E(1, \dots, \cos \theta_2 \sin \theta_1, \cos \theta_1), \quad (\text{D.87})$$

$$p_1 = q + p - p_\gamma - p_2. \quad (\text{D.88})$$

The calculation of the cross section for the process $\gamma g \rightarrow \gamma q \bar{q}$ is the same as in the previous Appendix D.5, and the formula for $d\sigma_{\alpha_S(4)}^{\gamma g \rightarrow \gamma q \bar{q}}$ is given by Eq. (D.80). This is included in the cross section for the γp collision in the summation over quarks and antiquarks ($2N_f$ flavours), see Eq. 5.5.

The calculation for the process $\gamma q \rightarrow \gamma q g$ with the gluon momentum (\vec{p}_2) parallel to \vec{p}_γ is different than the corresponding calculation in Appendix D.5 for the quark momentum (\vec{p}_1) parallel to \vec{p}_γ , since now we deal with the cross section which contains no singularities.

The cross section $d\sigma_{\alpha_S(4)}^{\gamma q \rightarrow \gamma q g}$ is equal to

$$E_\gamma \frac{d\sigma_{\alpha_S(4)}^{\gamma q \rightarrow \gamma q g}}{d^3 p_\gamma} = \frac{1}{sv\pi} \cdot \frac{1}{2s} \frac{d(P S)_3}{dv dw} |\overline{M}^{\gamma q \rightarrow \gamma q g}|^2, \quad (\text{D.89})$$

where $(PS)_3$ and $|\overline{M}^{\gamma q \rightarrow \gamma q g}|^2$ are given in Eqs. (C.15) and (D.1), respectively. This cross section contains no singularities and is proportional to θ_{cut}^2 . In the Part 4 of the phase space we assume that $w < w_{cut}$. This cut-off restricts the phase space of the final gluon this way that the gluon can not be too soft, so the cross section (D.89) contains no large terms due to the emission of soft gluons and is small $\sim \mathcal{O}(\theta_{cut}^2)$. It can be either calculated numerically or neglected if θ_{cut} is sufficiently small.

Similar configuration (gluon moving parallel to the final photon) was considered in Chapter 4, when the subtraction cross section in the small cone approximation was discussed. In this case we had no cut-off for w , and large terms due to the soft gluon emission might contribute to the cross section, so the subtraction term $d\sigma_{sub}^{\gamma q \rightarrow \gamma g + q}$ (4.21) could not be neglected. We have obtained the formula (4.21) for the subtraction term from Eqs. (C.15, D.1, D.89) keeping all terms of order $\mathcal{O}(\theta_{cut}^2)$ and neglecting higher powers of θ_{cut} .

Bibliography

- [1] G. Sterman, “An Introduction to quantum field theory”, Cambridge University Press, 1993.
- [2] M. Klasen, Rev. Mod. Phys. **74** (2002) 1221 [arXiv:hep-ph/0206169].
- [3] M. Krawczyk, A. Zembrzuski and M. Staszel, Phys. Rept. **345** (2001) 265 [arXiv:hep-ph/0011083]; arXiv:hep-ph/9806291.
- [4] R. Nisius, Phys. Rep. **332** (2000) 165 [arXiv:hep-ex/9912049].
- [5] U. Jezuita-Dąbrowska, “The polarization states of the virtual photon in $ep \rightarrow e\gamma X$ at the HERA collider”, MS Thesis, 1999.
- [6] T. F. Walsh and P. M. Zerwas, Phys. Lett. B **44** (1973) 195; E. Witten, Nucl. Phys. B **120** (1977) 189; W. A. Bardeen and A. J. Buras, Phys. Rev. D **20** (1979) 166 [Erratum-ibid. D **21** (1980) 2041].
- [7] R. J. DeWitt, L. M. Jones, J. D. Sullivan, D. E. Willen and H. W. Wyld, Phys. Rev. D **19** (1979) 2046 [Erratum-ibid. D **20** (1979) 1751].
- [8] J. D. Bjorken and E. A. Paschos, Phys. Rev. **185** (1969) 1975.
- [9] F. Halzen and A. D. Martin, “Quarks And Leptons: An Introductory Course In Modern Particle Physics”, John Wiley & Sons, 1984.
- [10] I. J. Schienbein, “Heavy quark production in CC and NC DIS and the structure of real and virtual photons in NLO QCD”, Ph.D. Thesis, Dortmund University, arXiv:hep-ph/0110292.
- [11] A. Gehrmann-De Ridder, G. Kramer and H. Spiesberger, Eur. Phys. J. C **11** (1999) 137 [arXiv:hep-ph/9907511].
- [12] T. s. Tu and C. m. Wu, Nucl. Phys. B **156** (1979) 493.
- [13] K. Iguchi and A. Niegawa, Prog. Theor. Phys. **64** (1980) 1093; Z. Phys. C **9** (1981) 135.
- [14] M. Fontannaz and D. Schiff, Z. Phys. C **14** (1982) 151.

BIBLIOGRAPHY

- [15] D. W. Duke and J. F. Owens, Phys. Rev. D **26** (1982) 1600 [Erratum-ibid **28** (1983) 1227].
- [16] A. Czechowski, M. Krawczyk, T. Hofmohl, A. Jacholkowska and M. Gorski, Z. Phys. C **19** (1983) 95.
- [17] M. Krawczyk, unpublished
- [18] P. Aurenche, A. Douiri, R. Baier, M. Fontannaz and D. Schiff, Z. Phys. C **24** (1984) 309.
- [19] A. C. Bawa and W. J. Stirling, J. Phys. G **14** (1988) 1353.
- [20] M. Krawczyk, Acta Physica Polonica B **21** (1990) 999.
- [21] A. C. Bawa, M. Krawczyk and W. J. Stirling, Z. Phys. C **50** (1991) 293.
- [22] A. C. Bawa and M. Krawczyk, Phys. Lett. B **262** (1991) 492.
- [23] A. C. Bawa and M. Krawczyk, Proceedings “Physics at HERA”, Hamburg 1991, vol. 1, p. 579, IFT-17-91.
- [24] P. Aurenche, P. Chiappetta, M. Fontannaz, J. P. Guillet and E. Pilon, Z. Phys. C **56** (1992) 589.
- [25] J. Żochowski, “The corrections of order α_S in Deep Inelastic Compton Scattering”, MS Thesis, 1992.
- [26] L. E. Gordon and J. K. Storrow, Z. Phys. C **63** (1994) 581.
- [27] L. E. Gordon and W. Vogelsang, Phys. Rev. D **52** (1995) 58; hep-ph/9606457.
- [28] M. Krawczyk and A. Zembrzuski, in: A. Astbury, D. Axen, J. Robinson (Eds.), Proceedings of the 29th Int. Conference on High Energy Physics, ICHEP’98, Vancouver, Canada, July 1998, World Scientific, 1999, p.895, arXiv:hep-ph/9810253.
- [29] M. Fontannaz, J. P. Guillet and G. Heinrich, Eur. Phys. J. C **21** (2001) 303 [arXiv:hep-ph/0105121].
- [30] M. Krawczyk and A. Zembrzuski, Phys. Rev. D **64** (2001) 114017 [arXiv:hep-ph/0105166].
- [31] L. E. Gordon, Phys. Rev. D **57** (1998) 235 [arXiv:hep-ph/9707464].
- [32] M. Fontannaz, J. P. Guillet and G. Heinrich, Eur. Phys. J. C **22** (2001) 303 [arXiv:hep-ph/0107262].
- [33] A. Zembrzuski and M. Krawczyk, arXiv:hep-ph/0309308.

- [34] M. Fontannaz and G. Heinrich, Eur. Phys. J. C **34** (2004) 191 [arXiv:hep-ph/0312009].
- [35] G. Heinrich, arXiv:hep-ph/0312070.
- [36] M. Fontannaz, arXiv:hep-ph/0407356.
- [37] G. Kramer, D. Michelsen and H. Spiesberger, Eur. Phys. J. C **5** (1998) 293 [arXiv:hep-ph/9712309].
- [38] A. Gehrmann-De Ridder, G. Kramer and H. Spiesberger, Phys. Lett. B **459** (1999) 271 [arXiv:hep-ph/9903377].
- [39] A. Gehrmann-De Ridder, G. Kramer and H. Spiesberger, Nucl. Phys. B **578** (2000) 326 [arXiv:hep-ph/0003082].
- [40] J. Breitweg *et al.* [ZEUS Collaboration], Phys. Lett. B **413** (1997) 201 [arXiv:hep-ex/9708038].
- [41] ZEUS Collaboration, prepared for 29th Int. Conference on High Energy Physics (ICHEP 98), Vancouver, Canada, July 1998.
- [42] J. Breitweg *et al.* [ZEUS Collaboration], Phys. Lett. B **472** (2000) 175 [arXiv:hep-ex/9910045].
- [43] Sung Won Lee, “Measurements of Prompt Photon Photoproduction at HERA”, Ph.D. Thesis, University of Glasgow, 2000, available at <http://www-zeus.desy.de/physics/qcd/thesis/>.
- [44] S. Chekanov *et al.* [ZEUS Collaboration], Phys. Lett. B **511** (2001) 19 [arXiv:hep-ex/0104001].
- [45] P.J. Bussey, talk given at the 9th Int. Workshop on Deep Inelastic Scattering, Bologna, Italy, 27 April - 1 May 2001; see also arXiv:hep-ex/0107063.
- [46] H1 Collaboration, Abstract 265, submitted to the Int. Europhysics Conference on High Energy Physics, HEP97, Jerusalem, Israel, August 1997.
- [47] H1 Collaboration, submitted to the Int. Europhysics Conference on High Energy Physics, EPS03, July 2003, Aachen (Abstract 093), and to the XXI Int. Symposium on Lepton and Photon Interactions, LP03, August 2003, Fermilab; R. Lemrani [H1 Collaboration], arXiv:hep-ex/0308066;
- [48] R. Lemrani, “Prompt photon production at HERA”, Ph.D. Thesis, Hamburg University, 2003, DESY-THESIS-2003-010, also available at http://www-h1.desy.de/publications/theses_list.html.
- [49] A. Aktas *et al.* [H1 Collaboration], submitted to Eur. Phys. J., arXiv:hep-ex/0407018.

BIBLIOGRAPHY

- [50] E. Laenen, G. Sterman and W. Vogelsang, Phys. Rev. Lett. **84** (2000) 4296 [arXiv:hep-ph/0002078].
- [51] D. Acosta *et al.* [CDF Collaboration], Phys. Rev. D **65** (2002) 112003 [arXiv:hep-ex/0201004].
- [52] G. Abbiendi *et al.* [OPAL Collaboration], Eur. Phys. J. C **31** (2003) 491 [arXiv:hep-ex/0305075].
- [53] S. Chekanov *et al.* [ZEUS Collaboration], Phys. Lett. B **595** (2004) 86 [arXiv:hep-ex/0402019].
- [54] E. L. Berger, X. f. Guo and J.-W. Qiu, Phys. Rev. Lett. **76** (1996) 2234 [arXiv:hep-ph/9512281]; Phys. Rev. D **54** (1996) 5470 [arXiv:hep-ph/9605324]; arXiv:hep-ph/9610497; arXiv:hep-ph/9708408.
- [55] P. Aurenche, M. Fontannaz, J. P. Guillet, A. Kotikov and E. Pilon, Phys. Rev. D **55** (1997) 1124 [arXiv:hep-ph/9606287].
- [56] S. Catani, M. Fontannaz and E. Pilon, Phys. Rev. D **58** (1998) 094025 [arXiv:hep-ph/9803475].
- [57] A. Vogt, Nucl. Phys. Proc. Suppl. **82** (2000) 394 [arXiv:hep-ph/9908315].
- [58] J. Chýla, JHEP **0004** (2000) 007 [arXiv:hep-ph/9911413]; arXiv:hep-ph/9811455; arXiv:hep-ph/0010140; arXiv:hep-ph/0010309.
- [59] P. Aurenche, R. Baier, A. Douiri, M. Fontannaz and D. Schiff, Phys. Lett. B **140** (1984) 87; P. Aurenche, R. Baier, A. Douiri, M. Fontannaz and D. Schiff, Nucl. Phys. B **297** (1988) 66.
- [60] L. E. Gordon and W. Vogelsang, Phys. Rev. D **48** (1993) 3136.
- [61] F. Aversa, P. Chiappetta, M. Greco and J. P. Guillet, Phys. Lett. B **210** (1988) 225; **211** (1988) 465; Nucl. Phys. B **327** (1989) 105.
- [62] P. Aurenche, A. Douiri, R. Baier, M. Fontannaz and D. Schiff, Phys. Lett. B **135** (1984) 164; P. Aurenche, R. Baier, M. Fontannaz and D. Schiff, Nucl. Phys. B **286** (1987) 553.
- [63] L. E. Gordon, Phys. Rev. D **50** (1994) 6753.
- [64] E. W. N. Glover and A. G. Morgan, Z. Phys. C **62** (1994) 311.
- [65] E. W. N. Glover and W. J. Stirling, Phys. Lett. B **295** (1992) 128.
- [66] E. W. N. Glover and A. G. Morgan, Phys. Lett. B **334** (1994) 208.
- [67] Z. Kunszt and Z. Trocsanyi, Nucl. Phys. B **394** (1993) 139 [arXiv:hep-ph/9207232].

- [68] B. L. Combridge, Nucl. Phys. B **174** (1980) 243.
- [69] W. A. Bardeen, A. J. Buras, D. W. Duke and T. Muta, Phys. Rev. D **18** (1978) 3998.
- [70] S. Bethke, arXiv:hep-ex/0211012; J. Phys. G **26** (2000) R27 [arXiv:hep-ex/0004021].
- [71] M. Glück, E. Reya and A. Vogt, Z. Phys. C **67** (1995) 433.
- [72] M. Glück, E. Reya and A. Vogt, Phys. Rev. D **45** (1992) 3986; Phys. Rev. D **46** (1992) 1973.
- [73] M. Glück, E. Reya and A. Vogt, Phys. Rev. D **48** (1993) 116.
- [74] A. D. Martin, R. G. Roberts, W. J. Stirling and R. S. Thorne, Eur. Phys. J. C **4** (1998) 463 [arXiv:hep-ph/9803445].
- [75] A. D. Martin, R. G. Roberts, W. J. Stirling and R. S. Thorne, Eur. Phys. J. C **14** (2000) 133 [arXiv:hep-ph/9907231].
- [76] A. D. Martin, R. G. Roberts, W. J. Stirling and R. S. Thorne, Eur. Phys. J. C **28** (2003) 455 [arXiv:hep-ph/0211080].
- [77] H.L. Lai, J. Huston, S. Kuhlmann, F. Olness, J. Owens, D. Soper, W.K. Tung, and H. Weerts, Phys. Rev. D **55** (1997) 1280 [arXiv:hep-ph/9606399].
- [78] J. Pumplin, D. R. Stump, J. Huston, H. L. Lai, P. Nadolsky and W. K. Tung, JHEP **0207** (2002) 012 [arXiv:hep-ph/0201195].
- [79] P. Aurenche, J. P. Guillet and M. Fontannaz, Z. Phys. C **64** (1994) 621 [arXiv:hep-ph/9406382].
- [80] M. Fontannaz, J. P. Guillet and G. Heinrich, Eur. Phys. J. C **26** (2002) 209 [arXiv:hep-ph/0206202].
- [81] L. E. Gordon and J. K. Storrow, Nucl. Phys. B **489** (1997) 405 [arXiv:hep-ph/9607370].
- [82] F. Cornet, P. Jankowski, M. Krawczyk and A. Lorca, Phys. Rev. D **68** (2003) 014010 [arXiv:hep-ph/0212160].
- [83] L. Bourhis, M. Fontannaz and J. P. Guillet, Eur. Phys. J. C **2** (1998) 529 [arXiv:hep-ph/9704447].
- [84] M. Gluck, E. Reya and M. Stratmann, Phys. Rev. D **51** (1995) 3220.
- [85] P. Hoyer, M. Maul, A. Metz and A. Metz, Eur. Phys. J. C **17** (2000) 113 [arXiv:hep-ph/0003257].

BIBLIOGRAPHY

- [86] C. F. von Weizsäcker, Z. Phys. **88** (1934) 612.
- [87] E. J. Williams, Phys. Rev. **45** (1934) 729.
- [88] V. M. Budnev, I. F. Ginzburg, G. V. Meledin and V. G. Serbo, Phys. Rep. **15** (1975) 181.
- [89] S. Frixione, M. L. Mangano, P. Nason and G. Ridolfi, Phys. Lett. B **319** (1993) 339 [arXiv:hep-ph/9310350].
- [90] U. Jezuita-Dąbrowska and M. Krawczyk, Acta Phys. Polon. B **34** (2003) 3133; arXiv:hep-ph/0211112.
- [91] F. Bloch, A. Nordsieck, Phys. Rev. **52** (1937) 54
- [92] M. Krawczyk and A. Zembrzuski, Phys. Rev. D **57** (1998) 10 [arXiv:hep-ph/9708274].
- [93] M. Krawczyk and A. Zembrzuski, Nucl. Phys. Proc. Suppl. **82** (2000) 167 [arXiv:hep-ph/9912368].
- [94] S. Frixione, Phys. Lett. B **429** (1998) 369 [arXiv:hep-ph/9801442].
- [95] E. L. Berger and J.-W. Qiu, Phys. Lett. B **248** (1990) 371; E. L. Berger and J.-W. Qiu, Phys. Rev. D **44** (1991) 2002
- [96] L. E. Gordon and W. Vogelsang, Phys. Rev. D **50** (1994) 1901
- [97] M. Glück, L. E. Gordon, E. Reya and W. Vogelsang, Phys. Rev. Lett. **73** (1994) 388
- [98] L. E. Gordon, Nucl. Phys. B **501** (1997) 175 [arXiv:hep-ph/9611391].
- [99] O. Biebel, P. A. Movilla Fernandez and S. Bethke [JADE Collaboration], Phys. Lett. B **459** (1999) 326 [arXiv:hep-ex/9903009].
- [100] R. K. Ellis, D. A. Ross and A. E. Terrano, Nucl. Phys. B **178** (1981) 421.
- [101] M. Furman, Nucl. Phys. B **197** (1982) 413.
- [102] H. Baer, J. Ohnemus and J. F. Owens, Phys. Rev. D **40** (1989) 2844; **42** (1990) 61.
- [103] W. T. Giele and E. W. N. Glover, Phys. Rev. D **46** (1992) 1980.
- [104] W. T. Giele, E. W. N. Glover and D. A. Kosower, Nucl. Phys. B **403** (1993) 633 [arXiv:hep-ph/9302225].
- [105] S. Frixione, Z. Kunszt and A. Signer, Nucl. Phys. B **467** (1996) 399 [arXiv:hep-ph/9512328].

- [106] S. Catani and M. H. Seymour, Nucl. Phys. B **485** (1997) 291 [Erratum-ibid. B **510** (1997) 503] [arXiv:hep-ph/9605323].
- [107] M. Klasen, T. Kleinwort and G. Kramer, Eur. Phys. J. directC **1** (1998) 1 [arXiv:hep-ph/9712256].
- [108] S. D. Ellis and D. E. Soper, Phys. Rev. D **48** (1993) 3160 [arXiv:hep-ph/9305266].
- [109] S. Catani, Y. L. Dokshitzer, M. H. Seymour and B. R. Webber, Nucl. Phys. B **406** (1993) 187.
- [110] P. Aurenche, arXiv:hep-ph/9706386.
- [111] S. Frixione and G. Ridolfi, Nucl. Phys. B **507** (1997) 315 [arXiv:hep-ph/9707345].
- [112] S. Catani and B. R. Webber, JHEP **9710** (1997) 005 [arXiv:hep-ph/9710333].
- [113] F. Cornet, P. Jankowski and M. Krawczyk, Nucl. Phys. Proc. Suppl. **126** (2004) 28 [arXiv:hep-ph/0310029]; P. Jankowski, JHEP **0405** (2004) 055 [arXiv:hep-ph/0312056].
- [114] F. Cornet, P. Jankowski and M. Krawczyk, arXiv:hep-ph/0404244.
- [115] F. Cornet, P. Jankowski and M. Krawczyk, arXiv:hep-ph/0404063.
- [116] W. K. Tung, S. Kretzer and C. Schmidt, J. Phys. G **28** (2002) 983 [arXiv:hep-ph/0110247]; S. Kretzer, H. L. Lai, F. I. Olness and W. K. Tung, Phys. Rev. D **69** (2004) 114005 [arXiv:hep-ph/0307022].
- [117] A. Zembrzuski, “The $ep \rightarrow e\gamma X$ process at HERA. The structure of the photon”, MS Thesis, Warsaw University 1991
- [118] A. Zembrzuski and M. Krawczyk, On the validity of the equivalent photon approximation and the structure of a virtual photon, Proc. “Physics at HERA”, Hamburg 1991, vol. 1, p. 617, and Warsaw Univ. IFT 91/15.
- [119] R. K. Ellis, M. A. Furman, H. E. Haber and I. Hinchliffe, Nucl. Phys. B **173** (1980) 397.